UNIVERSITA' DEGLI STUDI DI ROMA

LA SAPIENZA

FACOLTA' DI SCIENZE M.M.FF.N.N.

DOTTORATO DI RICERCA IN SCIENZA DEI MATERIALI

XXIV CICLO

In-situ Structural/Morphological study of polymer-based active materials for Organic Photovoltaic devices: bulk, surface and interface properties and aging effects

PhD Student: Daniele Bailo

Supervisors

Dr. Barbara Paci

Prof. Ruggero Caminiti

Coordinator

Prof. Ruggero Caminiti

Academic Year 2011/2012

The kingdom of heaven is like a mustard seed, which a man took and planted in his field. Though it is the smallest of all seeds, yet when it grows, it is the largest of garden plants and becomes a tree, so that the birds come and perch in its branches (Gospel o Matthew 13,31-32)

Il regno dei cieli è simile a un granello di senape che un uomo prende e semina nel suo campo. Esso è il più piccolo di tutti i semi; ma una volta cresciuto è il più grande di tutte le erbe e diventa un albero, tanto che gli uccelli del cielo vengono a ripararsi tra i suoi rami. (Vangelo di Matteo 13,31-32)

3

Indice generale

3

List of Symbols, Acronyms and Abbreviations

AFM   Atomic Force Microscopy

BHJ(s)   Bulk heterojunction(s)

CB   conduction band

C_{60} Buckminsterfullerene

EDXD   Energy Dispersive X-ray Diffraction

EDXR   Energy Dispersive X-ray Reflectometry

FF   Fill Factor

FT-IR   Fourier Transform Infrared Spectroscopy

HOMO   Highest Occupied Molecular Orbital

I_L current generated by the solar radiation

I_{sc} short circuit current

ITO   Indium Tin Oxide

LUMO   Lowest Occupied Molecular Orbital

MDMO-PPV   poly[2-methoxy-5-(3,7-dimethyloctyloxy)-phenylene vinylene]

NPs   Nanoparticles

OPV   Organic Photovoltaic

OSC   Organic Solar Cell(s)

PCE   Power Conversion Efficiency

P3HT   Poly (3-Hexylthiophene)

PCBM   [6,6]-phenyl-C_{61}-butyric acid methyl ester

PEDOT:PSS   Poly(3,4-ethylenedioxythiophene) poly (styrenesulfonate)

PET   Polyethylene terephthalate

PFB/F8BT   N,N'-(4-butilfenil)-bis-N,N'-*fenil*-1,4-fenilendiammina

P_m maximum value of power

T_g Glass Transition Temperature

TEM   Transmission Electron Microscopy

4

VB   valence band

V_{OC} open circuit voltage

5

Abstract

The main purpose of the present work is to investigate properties and issues limiting performance and lifetime of active materials used in organic solar cell, in particular Poly(3-hexylthiophene)] (P3HT) and [6,6]phenyl-C61-butyric acid methyl ester (PCBM) blends. The influence of structural and morphological properties on such aspects is investigated.

Indeed, organic Photovoltaic (OPV) devices have gained more and more interest in scientific and research community. Moreover, as material's cost is lower compared to silicon cells and structural-mechanical material's property are interesting for utility-scale applications, they are gaining interest also in the industrial field.

However their performances are still quite far from their inorganic counterpart.

Hence, a great effort is being done to improve cells performances and durability. In this perspective, while on one hand the research for new photoactive materials or devices structures can be of great importance, on the other hand the study of morphological and structural properties can be a key aspect which can unroll Organic Devices possibilities. Indeed, these properties have been shown to be strictly linked to cell performances, even if they still present uncovered issues. In particular, the possibility to perform non-invasive time resolved experiments examining not only the films bulk structure but also their surface and interfaces properties may play a crucial role.

This works deals, in particular, with P3HT:PCBM (Poly (3-Hexylthiophene):[6,6]-phenyl-C_{61}-butyric acid methyl ester) blends, which is one of the most studied because of its promising PV properties.

The investigation of such multi-layered systems, which present thickness of each layer of the order of 100-200nm, implies that techniques able to detect nano and meso-scale structures must be used. Moreover when the experiments are carried out in-situ and in real time, as the case of this work, non perturbative techniques are required.

Here, structural and morphological properties where studied by means of an unconventional tool which allows to use *jointly*, *in situ* and in *real-time*, Energy Dispersive X-ray Reflectometry (EDXR) and Atomic Force Microscopy (AFM) techniques. Thus, non-destructive investigations, both in reciprocal and direct space could be performed. Also, Energy Dispersive X-ray (EDXR) Diffraction and complementary FTIR studies were carried on.

6

A first part of this work was devoted to the set-up the joint EDXR and AFM tecnique. Hence information both on the reciprocal (EDXR) space and on the direct space (AFM) are obtained, and the possibility to probe the properties of buried interfaces is gained. The technique was validated by performing a series of preliminary test experiments on a reference sample and enabled to carry on the subsequent work of examining the multilayered system composing the intermediate stages of OPV cells.

There's no de-facto standard in OSC device structure, however two common configurations are ITO/PEDOT:PSS/P3HT:PCBM/Al.Electrode and ITO/P3HT:PCBM/Al.Electrode, the only difference being the buffer PEDOT:PSS (Poly(3,4-ethylenedioxythiophene) poly (styrenesulfonate)) layer. This buffer layer is often used for its smoothing and conduction-enhancing properties, but in working conditions it has shown to have some drawbacks, in particular when exposed to environmental humidity.

Hence a second phase of this work has been dedicated to the understanding of the structural and morphological processes which occur in the bulk of PEDOT:PSS and at its interface with ITO. These investigations, performed by time resolved EDXR and AFM experiments, used jointly in-situ, pointed out that this layer is subject to a water uptake/release when exposed to humidity and then to heat induced by solar irradiation. This process induces bulk morphological modifications which result to be irreversible, as confirmed by FTIR analysis, thus compromising its role as conduction enhancer layer, and indicating that a more stable polymer buffer layer and better encapsulation techniques are required.

The study then focused on the P3HT:PCBM blend active layer. A preliminary investigation on the role of PEDOT:PSS buffer layer and of the relative P3HT and PCBM weight ratios on the blend characteristics was carried on. The results show that in any case the photoactive layer results to be characterized by the morphological and structural parameters in the optimal range for application for organic solar devices.

Being aging one of the most consistent factor which limits performances, a systematic study of morphological and structural degradation of P3HT:PCBM active layer bends has been carried on up-on illumination, making use of the aforementioned joint AFM/EDXR technique.

In pristine samples a bulk aging effect was detected, and further Energy Dispersive X-ray Diffraction (EDXD) experiments allowed to relate this phenomenon to a secondary crystallization process of the P3HT counterpart. On the other hand, annealed samples active layer showed to have a good bulk stability, and only a slight increase of roughness limited to the buried interface was

detected. In addition, FTIR spectroscopy studies strongly supported the hypothesis that inter-diffusion of ITO into the organic layer (in ITO/P3HT:PCBM sample structure) was most likely the cause of morphological degradation. Therefore, the joint application of the in situ X-ray and AFM techniques, together with FTIR ex situ analysis, provided a clear picture of the concomitant chemical physical process occurring in the organic film. Importantly, such study demonstrated, for the first time, that the present approach for in situ non-invasive investigations of organic systems for PV devices is able to discriminate among the bulk, interface and surface aging effects.

The detected structural modification was then studied in-situ during illumination by means of a time-resolved EDXD analysis, thus pointing out the kinetics of the rearrangement of the active layer molecules. Such rearrangement could be described in real-time evidencing two different processes (P3HT crystallization and PCBM clustering into larger domains) which together with FTIR and AFM analysis support the hypothesis of a phase separation of the two components of the blend, which is one of the most relevant issues restraining conduction in active layer blends.

With these studies, also, a further proof that annealing results to be an effective treatment to stabilize P3HT:PCBM bulk hetherojunction active layer is given.

However, for the development of a flexible OPV technology, plastic substrates are needed. These letter are characterized by rather low glass transition temperatures, so that the employ of high temperature thermal treatments should be avoided.

Thus, in order to explore different promising solutions for cell stability, avoiding thermal annealing, the investigation of P3HT:PCBM blend doped with Silver Nanoparticles (Ag-Nps) was carried on. These materials are of great interest as the inclusion of Nps leads to an impressive improvement of device power conversion efficiency, up to 250% with respect to reference devices based on un doped P3HT:PCBM blends. Indeed, the incorporation of metallic nanoparticles in the active layer is expected to enhance absorption due to a plasmon mediated effect, causing improved initial cell efficiency.

Importantly, such improved performances come together with an enhanced stability. Indeed, pristine Ag-Nps doped samples, studied during illumination with EDXR/AFM joint technique, show improved bulk properties, the only morphological modification which was detected consisted in a minor roughening process taking place at the interface with PEDOT:PSS (in ITO/PEDOT:PSS/P3HT:PCBM sample structure). Moreover, the blends structural properties remained stable over time, thus evidencing that the doping of the blend with Ag Nps gives rise to enhanced structural stability.

8

The latter investigations are very encouraging, if we consider that the blend was not annealed. In this perspective, our finding pave the way to a systematic study of organic PV layers doped with metallic nanostructures, which can be key strategy towards the development of efficient and durable Organic Solar Devices.

- Part One -

State of the art

-Chapter I -

Materials and Devices

1.1 Introduction

Electricity produced by the sun, currently known as photovoltaic (PV) energy, is one of the most interesting alternatives to the so called non-renewable energy sources. It can enable one to avoid all the threats associated with traditional energy production techniques, and has many advantages and benefits, like the possibility of having clean energy in isolated places which are difficult to connect to traditional power plants [1]. A really persuasive example of the possibilities that an extended use of photovoltaics can unroll are satellites, which are powered by solar cell modules, and can orbit around the Earth for over twenty years [2]. In this perspective, science is getting more and more interested in photovoltaics, as the incredible increase of scientific studies in the last decade testify [3] (Fig.1).

The different PV technologies can be grouped in: crystalline silicon (c-Si) (first generation), thin film technologies (second generation) and organic solar cell (OSC) also known as Organic Photovoltaic (OPV) (third generation) [4]. The latter , based on organic materials, is gaining more and more interest in the scientific and research community, although the efficiencies are still lower than the inorganic counterpart (Fig 2).
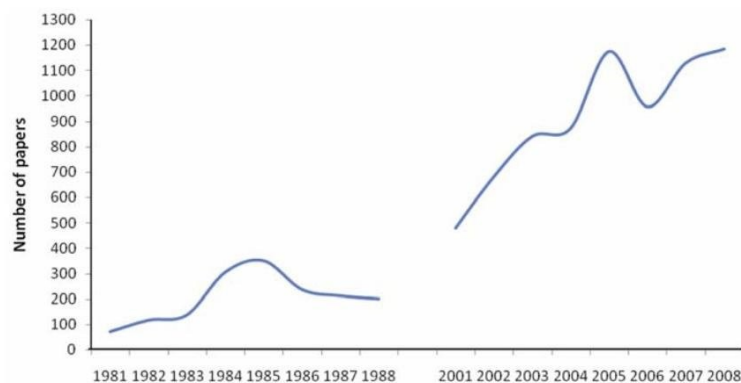
Figure 1: The intensity of publication such as the number of papers published per year and the annual growth of publication was comparatively higher in the latter period. Courtesy of [3]

Figure 2: Efficiency increase through years of different solar cell technologies. Source: Goswami

OPV modules indeed use the lowest carbon footprint of all solar panels; moreover the production of organic-based PV using industrial printing process allows to produce in one day an amount of cell area which, with the silicon-based technologies, typically takes one year [5].

Best Research-Cell Efficiencies
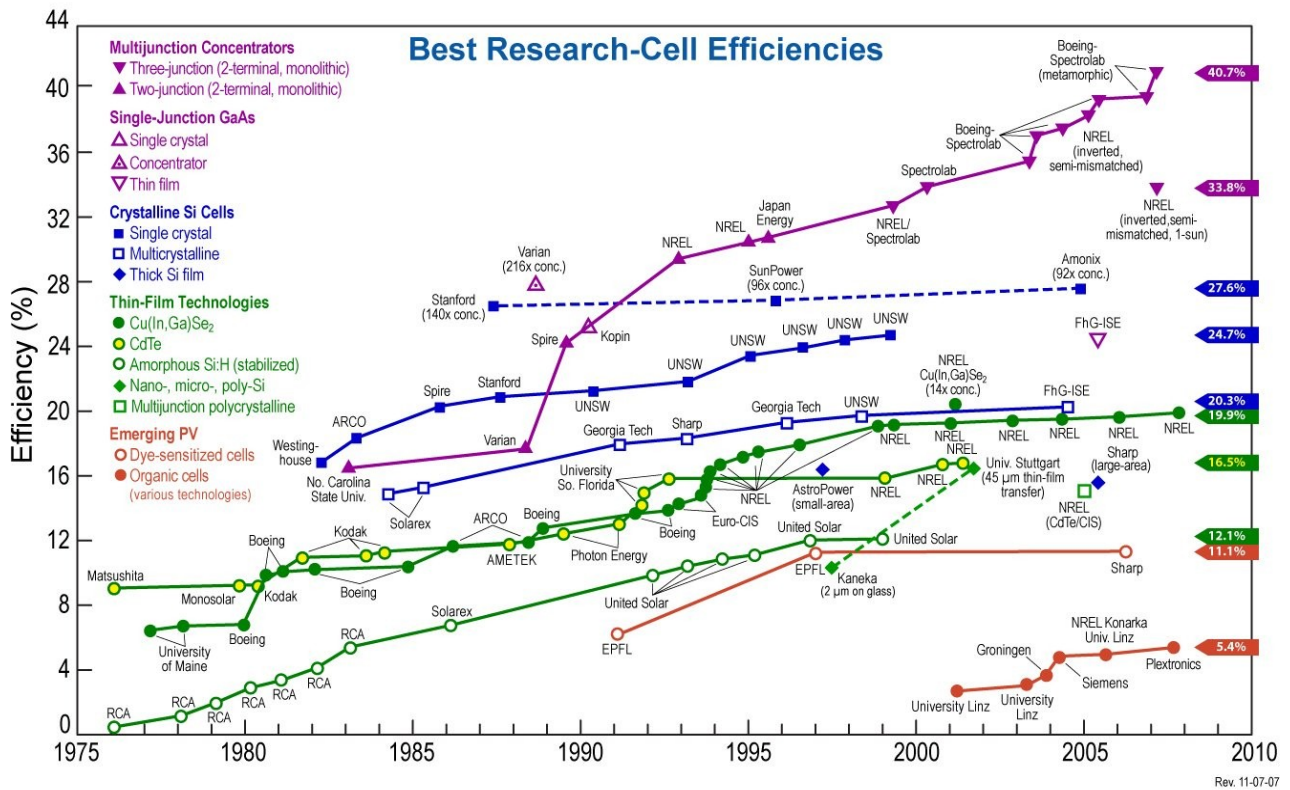
As the materials costs are much lower compared to silicon cells, the cost reduction due to printing techniques can be enormous. Organic cells also have some structural-mechanical advantages like flexibility and light weight, which make them interesting for utility-scale applications and enable the cell to be installed almost everywhere. The advantages of this technology are mainly the low-cost processing procedures and the possibility of tailoring the properties of the active materials [6], which can be done only in a limited way when inorganic materials are used.

The study of organic materials and their possible applications usually focuses both (i) on the production processes and on organic materials chemistry, in order to relate them with material's performances (in the case of OPV efficiency and lifetime, for instance), and (ii) on analytical procedures whose aim is to correlate material's micro and mesoscopic properties to electrical and macroscopic properties. In the present work we mainly use the latter methodology in order to focus on the comprehension of the processes, which occur in organic materials used for third generation photovoltaics connected both to the physical - chemical properties of materials and to the modifications of such properties.

Several studies [7-13] paved the way towards the understanding that the optimization of structural and morphological characteristics of the photo-active components of an organic solar cell strongly influences the photo-active properties. Hence in this work a primary role is played by crystallinity, order, orientation, anisotropy, which are some material's structural properties, and thickness, roughness, homogeneity, surface topology, which are some morphological properties.

Photovoltaic material blends like P3HT:PCBM (Poly (3-Hexylthiophene):[6,6]-phenyl-C_{61}-butyric

13

acid methyl ester), which constitute the photoactive portion of the devices, can be organized in nanodomains thus enhancing the photovoltaic properties [12]. Also, the molecular order of the two components influences the film charge-transport properties [10, 11, 13]. Moreover, when the organic materials are blends in which polymers are included, as in the case of P3HT, both polymer regularity and film molecular packing strongly influence the optical and electrical properties of bulk hetherojunction films [7-9]. Nanodomains structure, molecular order, polymer regularity, hence result to be key aspects, whose control strongly influences the two main parameters which are used to determine organic materials' suitability for use in PV devices: efficiency and lifetime. Even if different the two parameters are strongly correlated and while the first describes the overall material's performances in all its different aspects (capacity to convert the sunlight in electric energy, electron-hole conduction inside the material etc.), the second deals with degradation issues and material's resistance over time or when exposed to environmental factors like moisture or heating due to illumination. However, these topographical and structural studies are often carried on with ex-situ investigation techniques, which do not allow to follow the dynamical modifications of the parameters of interest.

Within this framework, the present study intends to be a contribution to the investigations of structural/morphological properties correlated with efficiency and degradation of P3HT:PCBM bulk hetero-junction blends, through the joint use of complementary experimental tools. For this purpose time-resolved Energy Dispersive X-ray Diffraction (EDXD) and Energy Dispersive X-ray Reflectometry (EDXR) [14, 15] have been used, in synergy with Atomic Force Microscopy (AFM) and FT-IR, to perform non-perturbative and non-destructive investigations. These techniques are used in an *in-situ, real-time* set-up, which allows to gain a deeper insight of structural and morphological processes which occur in the bulk, the surface and at the interfaces of organic materials thin film used for organic photovoltaic devices simulating working conditions or exposure to environmental factors like heat or humidity.

A detailed knowledge of the dynamic of the modifications occurring in simulated working conditions in the OPV cells, can as a matter of fact enable us to modify the materials properties in order to have better efficiency and lifetime, which still are two key aspects that – if substantially improved – can pave the way for a capillary diffusion of devices which make use of the so-called plastic photovoltaic materials, as organic bulk hereto-junction blends.

1.2 Organic Photovoltaic Cells: Physics and Materials

As introduced in the previous paragraph, even though the OPV cells still have low efficiency compared to silicon cells, they result to be incredibly interesting for the market, mostly for some advantages of the organic materials they are based on: they can be easily processed using relatively simple and low-cost techniques, like doctor blade, spin coating (wet-processing) or evaporation technique (dry- processing); the amount of organic material required to build a cell is relatively small because the configuration is usually a thin-film (100 nm thick film) and large scale production, which involves chemical processes, is easier than for inorganic materials, which involve growth processes; also, organic materials can be chemically tuned to obtain desired properties, so that we can build materials with *ad hoc* properties can be build [16], like band gap and conducting energies.

1.2.1 Physics

Organic materials used in PV cells are basically semiconducting materials, so the physics behind these devices inherits many of the concepts of semiconductor physics.

All organic semiconductor are called conjugated system. They are large molecules composed of repeating structural units that form a short (in the case of oligomers, with a few repeating units) or long chain (in the case of polymers) and are made, at molecular scale, of connected π orbitals with delocalized π electrons. The chains are composed by an alternation between single and double bond. The property coming out from conjugation is that π electrons can jump from site to site with low potential energy barrier, thus allowing the essential features of organic materials: charge transport (conduction) and generation, light absorption and emission[16].

Like for inorganic semiconductor in semiconductor physics, to describe this phenomena, a band model can be used. For organic materials the band energy gap between the $\pi-\pi^*$ orbitals is defined as the difference between the LUMO (Lowest Occupied Molecular Orbital) and the HOMO (Highest Occupied Molecular Orbital) as shown in Fig. 3 lower left. The highest occupied electronic levels constitute the valence band (VB) and the lowest unoccupied levels, the conduction band (CB). The width of the forbidden band, or bandgap (Eg), between the VB and CB determines the intrinsic electrical properties of the material (fig 6) [17, 18].

In organic semiconductors, intramolecular interactions are mainly covalent and intermolecular interactions are due to much weaker van der Waals and London forces, so there's a low coupling

15

between molecules; the conduction bands are hence much narrower than those of their inorganic counterparts, the concept of allowed energy bands is of limited validity and the predominant role is played by excitations and interactions localized on individual molecules [18]. Indeed, a defect can occur in the organic chain, for instance by means of an oxidative doping (electron is removed from the π system of the backbone, producing a free radical and a spinless positive charge). This combination of charge site and radical is called polaron (Fig. 3b). However, as the charged cations are not bound to each other by high energy bonding, they can freely separate along the chain. These charged defects which are independent of one another and can travel along the chain, referred to as soliton which can be negatively, positively or neutrally charged. Thus transport occurs via a sequence of charge transfer steps from one molecule to another (Fig. 3c), similar to the hopping between defect states in inorganic semiconductors.
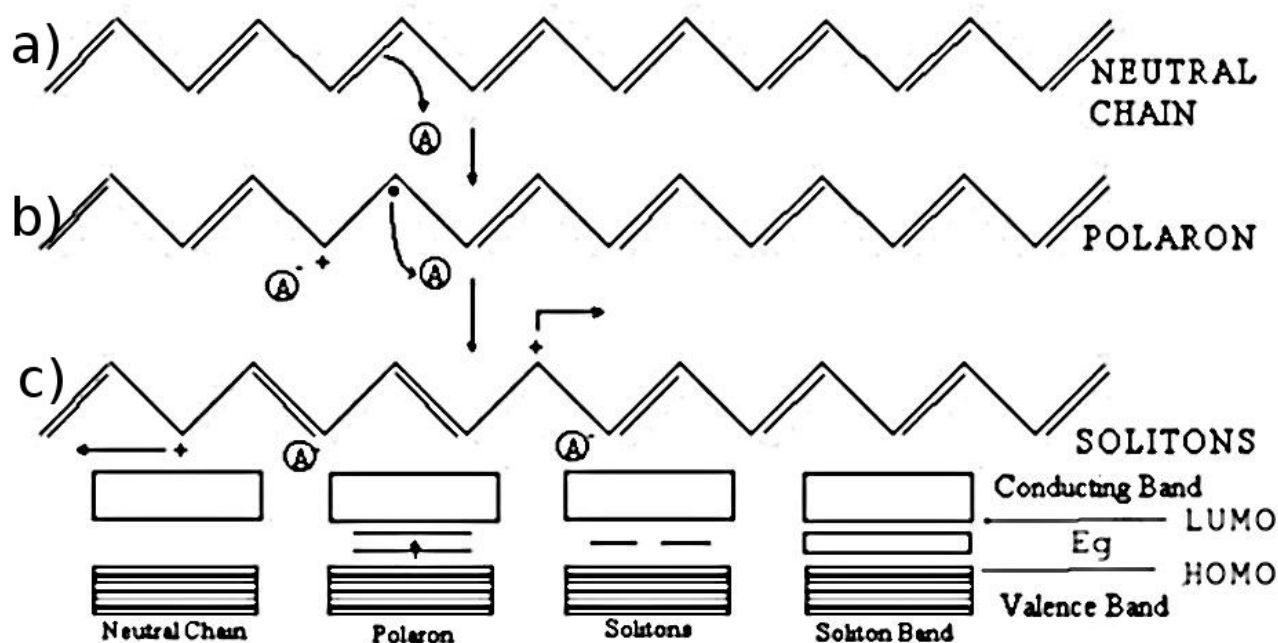
Figure 3: illustration of different conjugated chain: neutral chain and chains which include defects (polaron or solitons). The energy gap (Eg) between the π-π* orbitals is defined as the difference between the LUMO (Lowest Occupied Molecular Orbital) and the HOMO (Highest Occupied Molecular Orbital). The highest occupied electronic levels constitute the valence band (VB) and the lowest unoccupied levels, the conduction band (CB)

The insertion of defects into an organic semiconductor, like a conducting polymer, is called doping, by analogy with the doping of inorganic semiconductors, even if this is a rather misleading analogy. The pristine polymer is indeed converted into an ionic complex consisting of a polymeric cation (or anion) and a counterion which is the reduced form of the oxidizing agent (or the oxidized form of the reducing agent)[17]. Studies on polymer doping have been done, which stress the importance of

16

doping to enhance conductivity [19].

Again, like for inorganic semiconductors, the junction of two differently doped materials (n-type and p-type), the *depletion zone* or *depletion layer*, plays an important role in OPV active materials. In this zone indeed there are approximately no moving charge, and there is an electric field that is essential for charge separation which can occur when an excited state is arisen because of the photovoltaic effect. The *photovoltaic effect*, that is the basical physical effect allowing production of electric energy (i.e. electric current) from sun-light, happens when an active material, for example a thin film, is hit by the solar radiation. A part of this photon flux is reflected, a part tunnels thorugh the film and a part is absorbed. The photovoltaic process is accomplished by four steps [17]:

1) Absorption of a photon with an energy slightly higher than the band gap, leading to the formation of an excited state called exciton, which can be regarded as an electron-hole pair bound together by electrostatic interactions.

2) Exciton diffusion: for the light-electric current conversion process to take place, the exciton must diffuse to the depletion zone, where the charge separation occur.

3) Charge separation. It happens in the depletion zone, where effective fields break up excitons by causing the electron to fall from the conduction band of the absorber to the conduction band of the acceptor molecule

4) Finally the charge transport to the anode (holes) and cathode (electrons) occurs.

For organic materials, however, photoinduced charge (electron) transfer from optically excited conjugated polymers to the fullerene (C_{60}) electron acceptor molecule [20,21], together with increased photoconductivity upon C_{60} addiction to conjugated polymers [22-24] were observed. These studies on the photophysics of mixtures of conjugated polymers and C_{60} hence reported the evidence of reversible, metastable photo-induced, *ultrafast electron transfer* from conjugated polymers onto Buckminsterfullerene in a solid film. It was shown that a depletion zone exist not only at the interface of two semiconductors: the active material, indeed, in this case is a blend of electron *donor* (conjugated polymer) and electron *acceptor* (C_{60} for instance) materials, mixed together to form a bicontinuous interpenetrating network of bulk hetherojunction. The concept of bulk hetherojunction will be discussed deeper in the following pharagraphs.

In an OPV device, the delivered electric current corresponds to the number of created charges that are collected at the electrodes:

$$\eta_j = \eta_{abs} \times \eta_{diss} \times \eta_{out}$$

This number depends on: the fraction of photons absorbed (η_{abs}) which is correlated with the electron donor organic semiconductor band-gap; the fraction of electron-hole pairs that are dissociated (η_{diss}) which depends also on the exciton diffusion length and exciton lifetime; and

17

finally the fraction of (separated) charges that reach the electrodes (η_{out}) determining the overall photocurrent efficiency, which depends on recombination effects and on the material's conductivity [25].

It is hence evident the importance of collecting all the excitons generated by the solar radiation (photons); indeed if the diffusion length is less than the path lenght to the donor/acceptor interface, the exciton recombines, thus losing the possibility of generating a charge (i.e. electricity). Also, the problem of conductivity inside organic materials must be raised: transport of charges is affected by recombination during the journey to electrodes and the interactions with atoms or other charges may slow down the travel speed and thereby limit the current [26].

1.2.2 Materials and cell engineering

Organic semiconductors are a huge class of materials, and according to the mechanical properties required for their processing can be roughly grouped in: a) polymers, made of large ($10\text{-}10^3$) number of identical repeat units all linked together by covalent bonds in a linear way, b) oligomers, small fragments of polymers attached linearly and with a well defined length, c) dendrimers, also made of identical repeat units all linked together by covalent bonds, but in a three-dimensional way, d) pigments, which come from paint industry, which are small molecules bearing specific properties relevant to light absorption and charge generation, e) dyes, which have an electronic structure and properties similar to pigments, but are soluble [16].

Among them, polymers which can be conducting (conducting polymers) have been a promising area of research for technological applications since more than a decade [27], and result to be incredibly interesting because of the ease of processability (for instance deposition in thin films from solutions) and the possibility of tailoring their chemical properties (crosslinking and functionalization). The conductivity of polymers can vary over a very wide range, starting from insulating to semiconductor and towards metallic, by simply varying the concentration of the dopant and/or the type of dopant, which can be non-effective if used with different polymers.

In table I we report, as an example, a set of polymers, and respective dopant, together with the conductivity of the doped material.
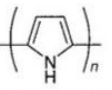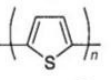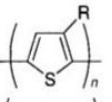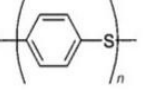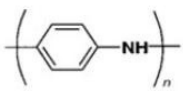
Polymer	Structure	Doping Materials	Approximate Conductivity (S/cm)
Polyacetylene	$(CH)_n$	I_2, Br_2, Li, Na, AsF_5	10,000
Polypyrrole		BF_4^-, ClO_4^-, tosylate[b]	500–7,500
Polythiophene		BF_4^-, ClO_4^-, tosylate[b], $FeCl_4$	1,000
Poly(3-alkylthiophene)		BF_4^-, ClO_4^-, $FeCl_4$	1,000–10,000
Polyphenylene sulfide		AsF_5	500
Polyaniline		HCl	

Table I
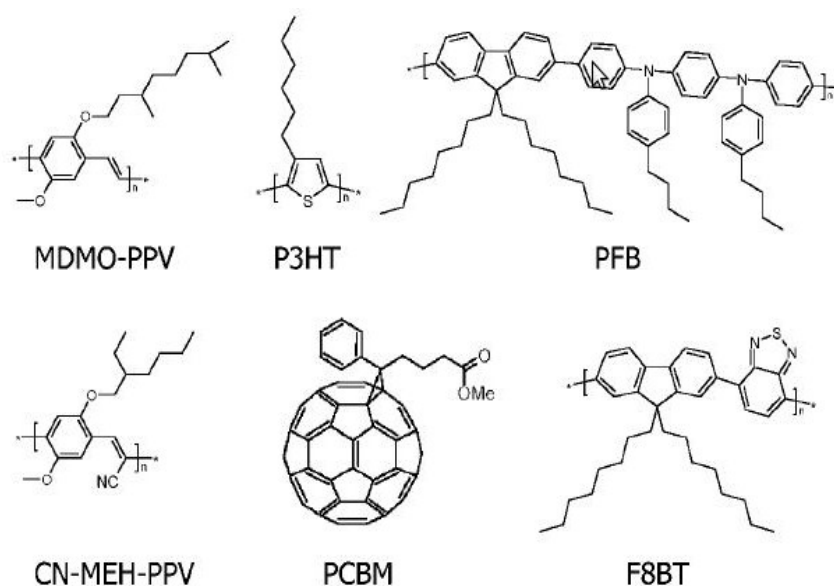
Figure 4: Several solution processable conjugated polymers and a fullerene derivative used in organic solar cells. Courtesy of [116]

Conducting polymers belongs to the family of conjugated polymer, which are also used as active materials in organic solar cell. However in the case of OPV the fundamental property is photoconversion of light in electric current, and the primary role is played by the junctions at the interface between a donor and an acceptor material, that can be a region of exciton creation, whose dissociation can eventually determine a charge transfer. The dissociation can occur at the sharp drop of potential at donor–acceptor (D-A) as well as semiconductor–metal interfaces. The junction can hence be created both by two doped organic materials, and by *blends* made up of a donor (a

19

conjugated polymer, for instance P3HT) and an acceptor material(for instance fullerene). In Fig. 4 we report some examples of conjugated polymer and acceptor molecules. One of the most used [28] pair of dopant-polymer is P3HT:PCBM, that will be discussed deeply in the next paragraphs.

Different device architectures are possible, which are strictly dependant on the active layer material's arrangement:

Single layer organic photovoltaic cell

Single layer organic photovoltaic cells were the first organic solar cells, and were based on single thermally evaporated molecular organic layers sandwiched between two metal electrodes with different work functions. The difference of work function between the two conductors sets up an electric field in the organic layer which helps to separate the exciton pairs, pulling electrons to the positive electrode and holes to the negative electrode, the already mentioned depletion zone (or depletion layer). The potential barrier formed at a metal–semiconductor junction which has rectifying characteristics is called Schottky barrier or Schottky junction [29] (Fig. 5). Efficiency of such cells is extremely low also because of the high rate of hole-electron recombination through the path to electrodes.
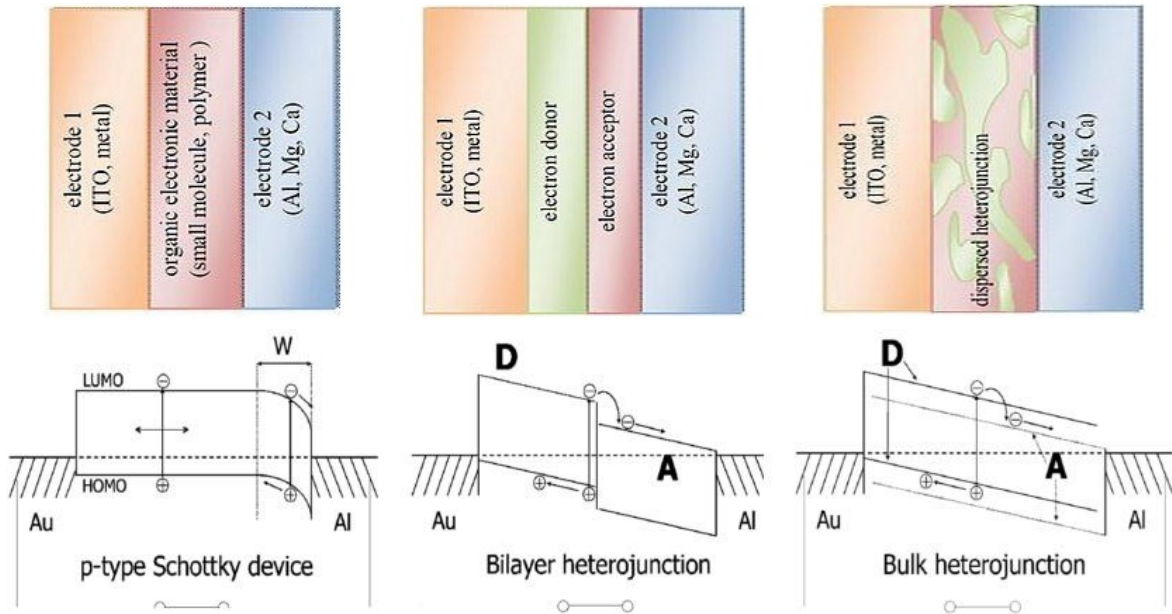
Figure 5: Upper part: sketch of a single, bi-layer and bulk heterojunction solar cell. Lower part: schematic of work functions of single layer (left), double layer (center), and bulk heterojunction (right) devices. In the single layer, photogenerated excitons can only be dissociated in a thin depletion layer W, so the exciton diffusion path is limited. In the bilayer device, the donor (D) contacts the higher and the acceptor (A) the lower work function metal, to achieve good hole and electron collection, respectively. Also in this case , as the photogenerated excitons can only be dissociated in a thin layer at the heterojunction, the exciton diffusion path is limited. In the Bulk heterojunction device, the donor (D) is blended with the acceptor (A) throughout the whole film. Thus, pho to generated excitons can be dissociated into charges at any place. Courtesy of [116].

Bilayer organic photovoltaic cell

In the case of a bilayer device, two layers, one of donor and the other of acceptor material, are planarly stacked together. Electrostatic forces at the interface between the two materials are present, which result from the differences in electron affinity and ionisation potential. In this case the interfacial electric field can drive charge separation, if both electron affinity and ionisation potential are greater in one material (the electron acceptor) than the other (the electron donor). The bilayer is sandwiched between two electrodes matching the donor HOMO and the acceptor LUMO, for efficient extraction of the corresponding charge carriers, as shown in fig. 5, centre. This structure is also called planar donor-acceptor heterojunctions [30].

Bulk heterojunction organic photovoltaic cell

A breakthrough was done in the mid 1990s with the introduction of dispersed heterojunction by different groups [31,32], where it was showed that a blend of electron-accepting and an electron donor material greatly improved quantum efficiency (the ratio of electrons delivered to the external circuit per incident photon of a given wavelength). If the length scale of the blend is similar to the exciton diffusion length, then wherever an exciton is photogenerated in either material, it is likely to diffuse to an interface and break up [30] (Fig. 6). If continuous paths exist in each material from the interface to the respective electrodes, then the separated charge carriers may travel to the contacts and deliver current to the external circuit. Those paths are called percolation paths, and can be imagined substantially like a bicontinuous interpenetrating network [33]. As the junctions are dispersed in the bulk, the electric field between the two electrodes doesn't exhibit sudden drops.
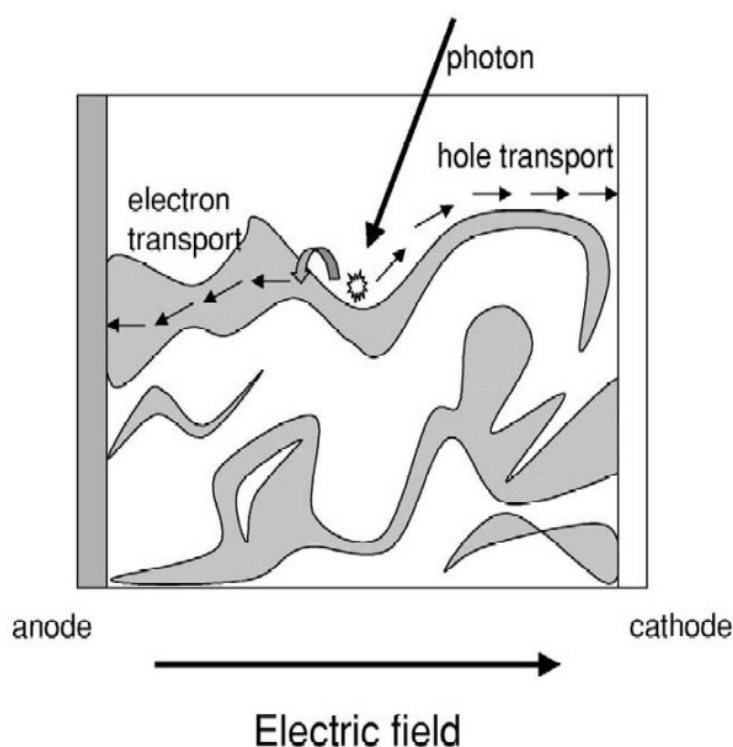
Figure 6: donor and acceptor materials may be blended together to yield a dispersed heterojunction. If the length scale of the blend is similar to the exciton diffusion length, then the probability that an exciton will reach the interface and dissociate is high. For efficient photocurrent collection, each material must provide a continuous path for the transport of separated charge to the contacts. Courtesy of [30bis].

The bulk heterojunction is thus the most successful device architecture for polymeric photovoltaics, because exciton harvesting is made near-perfect by creating a highly folded architecture such that all excitons are formed near a heterojunction [28]. Moreover, the bulk heterojunction configuration has opened the path to a wide study of materials that can be used like donor or acceptor: common acceptors used in polymer BHJs are indeed fullerenes [30bis-33bis], polymers[34], and n-type

inorganic nanoparticles[35,36]; common donor materials include MDMO-PPV poly[2-methoxy-5-(3,7-dimethyloctyloxy)-phenylene vinylene], P3HT [26]. Many studies can be found in literature, which focus on blends of P3HT or MDMO-PPV and the C60 derivative, PCBM [28].

Cell parameters

In order to understand cell efficiency and electrical behaviour in different conditions, some parameters must be introduced, whose tailoring can enhance cells performances. In an organic solar cell, informations about efficiency can be gathered by its I-V characteristic curve, where: I_{sc} is the short circuit current; I_L is the current generated by the solar radiation; V_{OC} is the open circuit voltage, that is to say the voltage of a running solar cell when no load is applied; I_m and V_m are current and tension values with which the power is maximum; P_m is the maximum value of power, represented like a rectangle (Fig. 7) [16].

In a OSC with constant solar incident radiation rate, when the load (required tension) increase and get close to the V_{OC}, the current may drastically decrease. The preferable behaviour would be to have a step-like current drop at V_{OC} (red lines in Fig. 7). With such ideal characteristic the device would have a linear behaviour within a certain range.

The ratio between the real and ideal characteristic is called Fill Factor (FF) and is calculated as:

$$FF = \frac{I_m \cdot V_m}{I_L \cdot V_{OC}}$$

So, being the power conversion efficiency (PCE) η the ratio between the generated power (P_m) and the incident solar radiation power (P_i), we have that:

$$n = \frac{P_m}{P_i} = \frac{I_m \cdot V_m}{P_i} = \frac{FF \cdot I_L \cdot V_{OC}}{P_i}$$
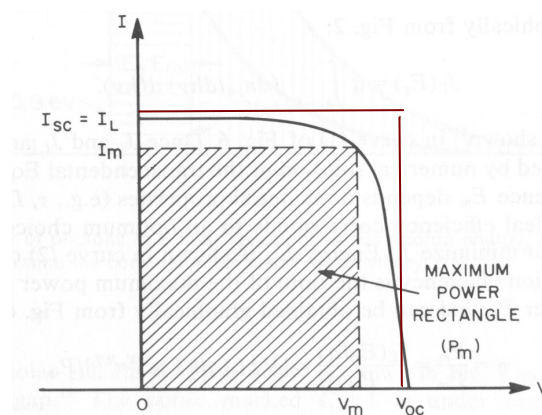
Figure 7: I-V characteristic curve of an organic solar device.

Hence, to increase the efficiency, some parameters must be modified, like short circuit current I_{SC}, open circuit voltage V_{OC}, fill factor FF, and characteristic resistivity (parallel, series, and shunt). It is easy to link these parameters with microscopic mechanisms: I_{SC} is nothing more than charge carriers, which is determined by exciton generation and separation efficiency, and charge collection. V_{OC} is related to the band gap between LUMO of acceptor and HOMO of donor. FF describes the part of energy loss in the form of Joule heat, which mainly determined by surface resistivity. [30]

The discussed parameters are influenced by the choice of material blends, their functionalization, the active layer nano-structure and the issues related to contacts between different organic layers or between organic-layer and electrode.

1.3 Cell Materials

Even if active materials plays a predominant role because they're responsible of the conversion of light into electric energy, an important contribution is given also by the other cell's layers, that is to say electrodes and additional layers that may enhance conductivity. So cell structure and configuration is also an important issue.
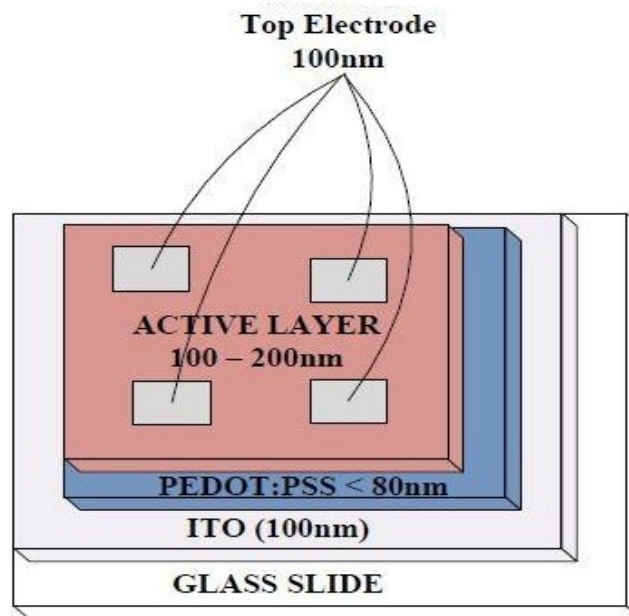
Figure 8: Device structure Schematic for polymer/fullerene solar cells. The active layer is between ITO electrode coated with a hole transport layer PEDOT:PSS and an aluminium top electrode [37]

The most used configuration, shown in Fig. 8, forcedly requires one of the two electrodes to be semi-transparent so that solar radiation can reach the active layer; indium–tin-oxide (ITO) is one of the most used mainly because of its electrical conductivity and high transparency[38], but a thin metal layer can also be used. The high conductivity of ITO films is due to high carrier concentration. In organic solar cells ITO is used as the anode, a hole injection layer.

The other electrode is very often aluminium but calcium, magnesium, gold, silver and others are also used [6]. The reason of the choice of such electrodes, is that after the dissociation of the exciton, the electron must reach one electrode while the hole must reach the other electrode, and this process is as efficient as the intensity of the electrical field provided by the asymmetrical ionisation energy/workfunctions of the electrodes is high. However it is not always possible to choose electrode materials which deliver the highest electric field. Indeed this necessity must be mediated with the degradation issues at the electrode interface, which increase the electron injection

barrier, and that can occur both at the ITO side (indium diffusion into organic layer [39]) or at the non-transparent electrode side as suggested in [40] where oxidation phenomena are hypothesised. So it is necessary to select electrodes materials which are both stable and which deliver a proper electric field.

Because of this phenomena, many of the high efficiency polymer:fullerene solar cells are made with a Poly(3,4-ethylenedioxythiophene) poly (styrenesulfonate) PEDOT:PSS buffer layer, which is inserted between the transparent electrode and the active organic layer, and has a positive effect on cell performances [41] for a number of reason that will be investigated in the next paragraph.

For active layers a wide range of possibility unrolls because, in the case of organic bulk heterojunction donor-acceptor blends, there is theoretically a variety of choice both for the donor and for the acceptor semiconductor materials. However, one of the most successful electron-acceptor materials for polymer solar cells in terms of efficiency is C_{60} and some of its derivates [42-45]. In this work the methano-fullerene PCBM was used.

With regard to the electron donor semiconductor semiconducting polymers, three representative can be cited [25,30]: (a) derivatives of phenylene vinylene backbones such as MDMO-PPV, and (b) derivatives of thiophene chains such as P3HT, and (c) derivatives of fluoren backbones such as (poly(9,9-dioctylfluorene-co-bis-N,N-(4- butylphenyl-1,4-phenylenediamine) (PFB/F8BT).

The P3HT and PCBM blend (P3HT:PCBM) is reported in a great number of works, and is one of the most interesting blend for OPV active layers [25,46-48].

1.3.1 PEDOT:PSS

One of the most used buffer layer is PEDOT:PSS or Poly(3,4-ethylenedioxythiophene) poly (styrenesulfonate), which is a polymer mixture of two ionomers [49]. One of the components in this mixture, PEDOT, is a conjugated polymer and carries positive charges and the other component, PSS, which is made up of sodium polystyrene sulfonate and carries a negative charge [49], the chemical structures being reported in Fig.9.

PEDOT:PSS is stable at high temperatures (100 °C) for a long period of time (1000 h) without noticeable changes in either their electrical conductivity or optical transparency[50]. This latter characteristic make it suitable for use in photovoltaic devices. Indeed, ITO electrode is often used alone as anode in OSC, but it has been shown that an additional layer of PEDOT:PSS can improve the devices performances because of a better selectivity of the anode, on account of the higher work function relative to ITO [51]; moreover the PEDOT:PSS layer improves the surface quality of the ITO electrode by smoothing out the ITO surface [52], increase the photovoltage through the surface enrichment of PSS components which facilitates the charge injection /extraction [53], seals the active layer from oxygen, and keeps cathode material from diffusing directly into an active layer

26

[54,55].
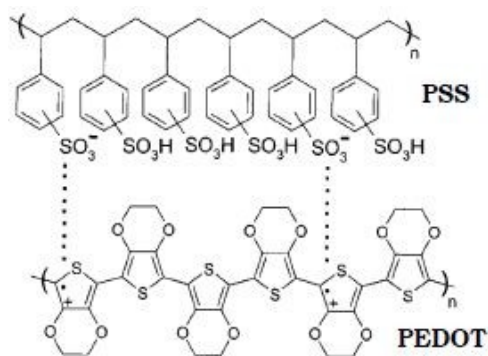
Figure 9: Chemical structure of the PEDOT:PSS film

PEDOT:PSS can be also modified by the addition into solution of glycerol [55], which improves hole-injection from the active polymer film into the PEDOT:PSS anode.

However, issues related to degradation have to be addressed, as will be described in the following sections.

1.3.2 P3HT:PCBM Bulk Heterojunctions

In recent years incredible progress has been made in increasing efficiencies of OPV using P3HT blended with methano-fullerene PCBM as active layer, in a bulk-hetherojunction configuration, with a PCE that exceed 6% [56-58]. At the moment of writing this work, the best efficiencies are reported by Mitsubishi Chemical which affirm to have reached the 8.5%. Such efficiencies, together with some interesting properties of good solubility, processability and environmental stability [59,60], make the P3HT:PCBM one of the most promising and used materials for applications in OPV. Chemical structure of both P3HT and PCBM is reported in Fig. 4.

However, being still far from the efficiencies of the inorganic counterpart (more than 16% [61]), much effort is being done to improve P3HT:PCBM performances. The general aim is to optimize the percolation, structure and orientation of both the donor and acceptor materials in the film, in order to increase both conductivity and conversion efficiency. This latter parameter is strongly affected by the low band gap of organic materials, which can be tuned to make overlap better the absorption spectrum and the solar radiation [32], whose maximum is a wavelength corresponding to a band-gap of 1.8eV [62].

Hence as described in [63, 64], different approaches and issues must be taken into account when dealing with efficiency optimization of the active layer blend, which are connected with blend morphology control:

1.   Processing of materials (solvents and additives) and deposition procedures have been found

27

to play an important role in efficiency enhancement. For instance, they have shown to influence the light absorption of P3HT:PCBM [65]; also, the introduction of a few volume per cent of other substances (alkanedithiols) in solution used to spin-cast the blend [33], definitively enhances the efficiency through altering the bulk heterojunction morphology. Depending on the solvent (chloroform or chlorobenzene), the blend shows different absorption spectra which can indicate a higher degree of P3HT side chain ordering [66]. The ratio of the two components [67] and the molecular weight [68] can be determinant for the efficiency of the resulting bulk etherojunction solar cell, as well as the thickness of active-layer [69, 70]. Different solubilities and surface energies of the blend components as well as the dynamics of the spin-coating process influence vertical stratification and regularity [63] which favour charge transport.

2.   Structure and morphology are very important issues as well; an example is given by the study of regioregular (RR) P3HT blended with PCBM [62], where through GIXS measurement carried out in a Synchrotron facility it was possible to demonstrate that high RR is not necessary to achieve high-efficiency solar cells and that using a polymer with a lower RR actually has the benefit of improving the thermal stability of the device.

3.   Many studies focus on annealing, which seems to be one of the most used treatment to control structure and morphology: as a matter of fact, X-ray diffraction experiments [71] and other Transmission Electron Microscopy (TEM) studies [10,11] done to correlate structural to optical properties, showed that these properties can improve with pre-processing or post-processing treatments like annealing at proper temperatures and for specific time length (150°C for 30 minutes [32]). Annealing was also studied in combination with the concentration ratio of the two components[72]. Furthermore, EDXR was successfully used to demonstrate that the reorganization of the blend bulk can be inhibited by thermal annealing treatments capable of stabilizing the organic layer bulk morphology [73].

4.   Another important issue to address to in P3HT:PCBM blend, is the inter-diffusion or clustering of PCBM in the P3HT matrix. This issue will be discussed also in the experimental section, but we cite some interesting studies that have been carried on, like the one of Treat [74], which using a bilayer of P3HT and PCBM observes a fast interdiffusion of these two components at low temperatures in a homogeneous system previously annealed at 150 ° C for 30 s. Also, its results support the idea that the presence of PCBM within disordered P3HT has little influence on the increase in the number and size of P3HT crystallites during thermal annealing. Other interesting studies[75], applying grazing-incidence small-angle X-ray scattering (GISAXS) and wide-angle X-ray diffraction (GIWAXD) to study the morphology of P3HT/PCBM bulk heterojunction solar cells after their thermal annealing, show the relationship between the relative length scales of the PCBM clusters and P3HT crystallites and the devices' performance: after annealing, indeed, PCBM

molecules diffuse out of the P3HT matrix and forming larger PCBM clusters[76], and phase separation of P3HT and PCBM occurs to provide improved continuous pathways for the holes and electrons, with PCBM cluster with a radium of giration of about 15 nm. Phase-separated domain size is indeed imperative for good device performance, and the experimental data is consistent with theoretical studies [78,79] which shows that nanoscale phase separation with a bicontinuous pathway toward the electrode is the desired configuration.

From the above, it is evident that a better knowledge of structure and morphology of the blend is necessary in order to correlate the modifications or treatments which can be made before, during, or after the processing of the blend, to the structural properties that enhance efficiency and lifetime.

1.3.3 Incorporation of metallic nanostructures in P3HT:PCBM BHJs

The study of BHJs polymer blends structure and morphology can profitably overextend including non polymeric materials.

In the case of NPs, the principle is to make a blend in which small nanoparticles (10-30nm) are present. Nanoparticles can be also made with the composants of the blend (one or both) [80]. They are an intermediate system between bulk films and single molecules, but have a reduced complexity and heterogeneity compared to the bulk material because the number of molecules under investigation is lower.

Devices incorporating metallic nanostructures are promising candidates to overcome some traditional BHJs devices limits, among them: (i) the relatively low absorption of the P3HT:PCBM blend in the near-IR range, leading to rather poor spectral match with the solar spectrum, and (ii) the OPV devices "sandwich-like" configuration and the low carrier mobility of the polymer [81] imposing a restriction in the active layer thickness, so that it is not possible to gain absorption by using thicker films. Hence, NPs doped films take advantage of the localized surface plasmon resonance (LSPR), resulting from the resonant interaction of the surface electrons of the metallic nanostructures and the electromagnetic field of light.

In particular, incorporating metallic nanoparticles in the BHJ of OPV cells, the LSRP effect of the NPs enhances their surrounding electromagnetic fields, which is expected to boost the light harvesting (absorption) ability of active layer in their vicinity and increase the probability of exciton generation and dissociation, leading to an increase of the J_{sc} and FF of the NPs-doped devices.

Illumination induces the excitation of surface-waves (surface plasmons), propagating at the interface between the dielectric-polymer material and the metal nanostructures, having size smaller than the light wavelength. As a result of such collective electron oscillations, a local enhancement

of the incident electromagnetic irradiation field occurs, leading to enhanced exciton generation and improved device efficiency [82-86] .

Besides the possibility to obtain superior photovoltaic performance, we will show in the experimental section that the composite blends exhibit improved structural stability compared to the pristine bulk heterojunction layers.

1.4 Stability and degradation

1.4.1 Chemical physical aspects related to material and device degradation

Necessity of improving PCE through tailoring of polymer properties is not the only crucial aspect related to OSC. Another problem that must be faced is the degradation of materials which is strictly correlated to cell lifetime and stability.

Degradation can be considered as the loss of material's properties induced by any external or internal factor.

Many concomitant chemical-physical effects concur to the device degradation which are addressed in the review paper [129] and schematized below. According to [129] degradation phenomena can be grouped in two main categories: chemical degradation and physical/mechanical degradation.

The molecules playing a predominant role in the former type of degradation are oxygen and water that can be absorbed during fabrication process or can diffuse in the post-production phase into the device. Also, an important role is played by the chemical reactions between the electrode material and the active layer. Mechanical degradation is, as obvious, correlated to cell materials mechanics. In turn, materials structure and mechanics can be correlated to phenomenon like heating. It is indeed evident that the spatial organization of the different materials composing the layers strongly influences efficiency, which results to be enhanced when an organized morphology is adopted [111,112] but can be reduced in presence of phase segregations or clustering [9,113].

Chemical effects related to degradation

Diffusion of oxygen and water into the OPV device

Several studies also suggest that degradation can be correlated to the air exposure of the cell, as shown in [104], where the degradation is independent from light exposure, and is rather caused by the water absorption by the hygroscopic PEDOT:PSS buffer layer, which increases the resistance at the interface with the active layer. Also in this case a good strategy can be an annealing treatment, which causes an increase in conductivity correlated with evaporation of sorbitol (which can be regarded as a processing additive) from the film [105].

Photochemistry and photo-oxidation of polymers

Photo-oxidation can occur when active materials blends are exposed to illumination and to oxygen or water vapor as reported for MDMO-PPV/C60-PCBM[87], while they should be photochemically stable and the nanoscale bicontinuous donor-acceptor network (i.e. BHJ structure) should be

31

preserved. A way to decrease the photodegradation of such organic materials, is to mix them with fullerenes as demonstrated in [88,89], where the stability of the conjugated polymer-fullerene solar cell mixture, forming a charge-transfer donor and acceptor couple, has shown to be higher than the stability of conjugated polymers in light emitting diodes [90] .

Degradation as a function of polymer preparation

Polymer synthesis can be also correlated to lifetime of OPV, as shown in [130,131]

It is known, indeed, from literature that various amounts (a few %) of impurities and defects are present in PPV polymers when differently synthesized, probably affecting the performances. However a direct connection was not established. Consequently purification seems to play a primary role as reported in a few instances, but it is still far from being a general rule.

Degradation at the metal/organic interface.

Reese [99,100] investigated the stability of a variety of electrodes for devices stored in an inert, dark environment, and also performed a set of experiments to separate the effects at the metal/organic interface from the degradation of the active layer or the hole extraction interface. The results show that one of the most important factor for stability, compared to whether or not a device is exposed to sunlight, is the exposure time of a complete device to "one-sun illumination", at reasonably elevated temperatures. Also, air metal/organic interface can be a significant source of degradation in the devices. In this direction, a deeper study has been carried on in [101], evidencing the correlation between the decrease of photo-current and photo-oxidation phenomena occurring at the Al-organic film buried interface. Furthermore, as evidenced in some studies by mean of the Energy Dispersive X-ray Reflectometry technique [102], the Ca electrode could be subject to degradation in presence of PEDOT:PSS due to residual water molecules in the cell from PEDOT:PSS deposition, and this effect may be inhibited by depositing the organic film directly onto the ITO transparent electrode. Degradation effects due to instability of PEDOT:PSS can therefore be compensated by annealing treatments at a proper temperature, as described in [103].

Degradation of the PEDOT:PSS layer

As already described, the PEDOT:PSS often used as a buffer- hole transporting layer between the ITO electrode and active layer. Its instability in ambient condition, especially when exposed to humidity, has been studied in [132,133]

Rapid degradation was evident in the cells illuminated under humid conditions (>40% RH) either in air or in nitrogen. This phenomena were correlated to the hygroscopic PEDOT:PSS layer water uptake from the atmosphere, increasing sheet resistance. Experiments were carried on over a time of

about 8 hours.

In the buffer layer, PSS is present in excess amount compared with PEDOT and can thus diffuse to other parts of the device, i.e. to other layers and possibly react with other components of the device, thus giving birth to degradation phenomenon or particle formation [134]

In the present work this subject will be deeply investigated and morphological and structural aspects related to PEDOT:PSS instability will be shown, in the experimental section.

Mechanical effects related to degradation

Degradation caused by temperature

Another type of degradation is correlated to the high temperature that the solar cell can reach when exposed to sun light [9]. If it gets near to the glass transition temperature (Tg), a degradation can take place [7], which is not associated to the chemical stability, but rather to the increased molecules mobility; indeed, PCBM acceptor molecules can diffuse through the organic material matrix and form large clusters, thereby increasing the dimension and extent of phase separation [8]. In this case a basic strategy to compensate the limited thermal stability of the morphology is to obtain, through functionalization, materials with a higher Tg. Also, this nanomorphological instability can be fixed by post production cross-linking of the components, to prevent their diffusion [91] which hinder the conductivity of the thin film. Annealing can be an effective strategy to enhance blend stability under light induced heat. In P3HT:PCBM blend indeed, thermal annealing was used to produce and stabilize a nanoscale interpenetrating network with crystalline order for both components [92]. It results to be such a powerful treatment because it causes recrystallization (which is correlated with improved optical absorption [94] and to the mobility of holes [95]) and reduces the free volume and the density of defects at the interfaces [96]. Moreover, thermal annealing under chloroform vapor [97] or simple thermal treatment [98] leads to an overall increase in power conversion efficiency.

Morphology control and morphological stability

The relative high efficiency of bulk hetherojunction solar cell is correlated to the blend nanostructure. Indeed, after the creation of an exciton subsequent to the interaction between solar radiation and active layer material, the exciton must reach the donor/acceptor interface where it can split in a hole-electron couple. The exciton diffusion path in the organic material is of the order of 10 nm limiting the optimum size of the polymer domains. At the same time, the charges that are created at the interface between the donor and acceptor must have continuous paths to the outer electrodes. So the role of the nanostructured materials blend is evidently of primary importance.

It is, however, not obvious how to obtain the optimal nanophase separation in the final device since it is probably not the thermodynamically most favorable geometry.

An entire new scenario unrolls when methods for nanomorphology control are investigated, and a number of works reporting different techniques can be found, for instance: in [135] the presence of single wall carbon nanotubes (SWCNTs) is correlated to performances and structure of the active material; in the paper [136] the fibrillar nanostructure was investigated evidencing the intimate relationship between processing protocols, which define the mesoscale phase-separated domains, and the molecular level ordering within the domains, which determines local transport characteristics; the work [137] explored the direct writing approach of active layer (P3HT:PCBM) through inkjet-printing techniques, correlating different experimental conditions with cell performance.

Among the methods used to improve cell stability against degradation factors, annealing results to be one of the most suitable. For instance, it was used to improve the efficiency of solar cells based on P3HT [98,76] and studies have been carried on to determine the optimal duration of annealing [106]. Also it was demonstrated that by annealing the devices and simultaneously applying an external voltage, the characteristics of solar cells based on P3HT:PCBM are improved [107]. It is considered hence a powerful technique to increase cell efficiency which is strongly correlated to morphology, as shown in the next paragraph.

Still, annealing should be avoided in order to use flexible substrates as PET (Polyethylene terephthalate) and possible different strategies should be explored as well. An interesting possibility is offered by polymer-inorganic nanostructures nanocomposites, as will be discussed in the experimental section, presenting the results obtained by doping the BHJ active layer with metallic Nanoparticles (Nps).

Morphology control issues will be analyzed deeply in the next paragraph.

1.4.2 Characterization Methods

The ability of detecting the mechanisms which contribute to degradation is of primary importance in OPV devices studies, as evidenced in the previous paragraphs, in order to understand and avoid such phenomenona and also to improve performances.

As shown in [129], investigation methods can be grouped according to the type of information they can provide, that is to say chemical or physical information. In this perspective, a number of parameters can be enumerated in order to define a characterization method: type of analysis (bulk/surface), type of imaging (2D, 3D), possibility of depth profiling, destructive (non-destructive) analysis, type of information (chemical/morphological/structural), etc.

When performing a measurement, the achieved results can be average or site specific information.

In the first case the methods provide information from non-specific locations in the sample. This is the case of, for instance, impedance spectroscopy, Near-field scanning optical microscopy (NSOM) or reflectometry; in the latter case the experimental methods provide information from more or less specific locations in the sample, like in the case of time-of-flight-secondary ion mass spectrometry or Atomic Force Microscopy.

Impedance spectroscopy measures the dielectric properties of a material as a function of frequency, and for a polymer solar cell, the results can be interpreted in terms of the equivalent circuit with a resistive/capacitive (RC) element. It has been used successfully to monitor the progress of the annealing process [138] or to investigate the C60/metal interface [139]. This technique can provide a bulk, non destructive analysis and relevant information about chemical and morphological parameters can be obtained.

A variation of **NSOM** *called NSPM (near-field scanning photocurrent microscopy)* has been used to correlate morphology with current generation in polymer solar cells [140]. No conclusions on how the device morphology affects the efficiency or degradation of polymer solar cells were made. However this work demonstrated the possibilities offered by such technique, being one of a few methods able to characterize the solar cell performance at nanometer level.

Time-of-flight-secondary ion mass spectrometry has proven to be versatile in the study of degradation mechanisms of OPV. It can provide valuable information on the molecular structure and it allows to monitor the structural changes in variable environmental conditions, providing interesting information on surface, 2D imaging and depth profiling. However, being a mass spectrometry technique, it results to be destructive.

Time-resolved X-ray reflectometry and Atomic Force Microscopy are deeply discussed elsewhere in this work.
Ideally, techniques which could provide time-resolved analysis of structural and morphological parameters at the same time would be really helpful to understand the hidden mechanisms which contribute to performance lowering. Of course it is an ideal situation and it is not achievable with one single kind of measurement. However an interesting opportunity is given by the possibility of performing measurements with different techniques at the same time.
Following this philosophy, a very promising way seems to be the use of techniques which can give both local and average information, like the ones shown in the present work (Energy dispersive X-ray reflectometry and Atomic Force Microscopy)
Indeed, both surface and interface information can be obtained, thus providing a morphological

description of the sample. The particular set-up used allowed to carry on in-situ time resolved experiments, thus giving the possibility of monitoring morphological modifications over time. Additional information are also obtained by the use of in-situ time resolved X-ray diffraction, together with FTIR spectroscopy. Both techniques, as discussed in the experimental section, provide information about structural/chemical modifications of the studied samples in a non destructive way.

1.4.3 Increasing efficiency and lifetime through morphology control

Nanoscale morphology becomes a primary key parameter in bulk hetherojunction solar cells, and is important to improve cell efficiency, as demonstrated using different organic active materials [108-110]. Experiments show that when an organic material blend like P3HT:PCBM or MDMO-PPV:PCBM adopts an organized morphology, the cell's performance is improved [107, 111,112,31], while, on the other hand, a phase segregation and a formation of cluster [9] of one of the two blend's components reduces performance [113]. When morphology is organized, it is found that the absorption spectra is widened, ISC increases, while VOC slightly decreases. Moreover, surface resistivity decreases.

However, morphology can be subject to degradation during cell working mostly due to molecular diffusion of fullerenes at elevated temperatures for long times, which are the operation conditions of the cell exposed to sunlight. The thermally activated phase separation, which in polymer: PCBM blends consists in PCBM diffusion and formation of crystalline aggregates, increases the morphological instability [8].

Fortunately, nanoscale morphology can be somewhat controlled. Some parameters have been experimentally identified, like in the case of in MDMO- PPV/PCBM polymer-fullerene blends, as influencing the nanoscale morphology [30]: (a) the primary chemical structure of the materials determining tertiary organization structures, (b) the used solvent, (c) processing temperature,(d) the relative ratio in composition between polymer and fullerene, (e) the solution concentration, and (f) the before mentioned thermal annealing.

The primary chemical structures of polymer and fullerene determine the solubility in organic solvents and the miscibility between these two compounds. The solvent itself furthermore influences the drying time during film formation, whereas thermal annealing enables the recrystallization. Diffusion of one or both components in the blend leads to a modification of the phase separation [14] which, as already mentioned, is an undesired effect. Also, relative concentration of the two component of the blend plays an important role in determining morphology and hence performances [114,115].

36

Nanoscale morphology is of course correlated with the degree of order of the blend or of one of its components. For instance, the regioregularity of P3HT, if tuned within certain limits, has been found to increase the thermal stability [62]. The overview on organic photovoltaic of Spanggaard [6] reports different possible morphologies of hetherojunction solar cells, which we report in Fig.10 as an example. For a complete and exhaustive description of each morphology and corresponding performances we invite the reader to look at [6].
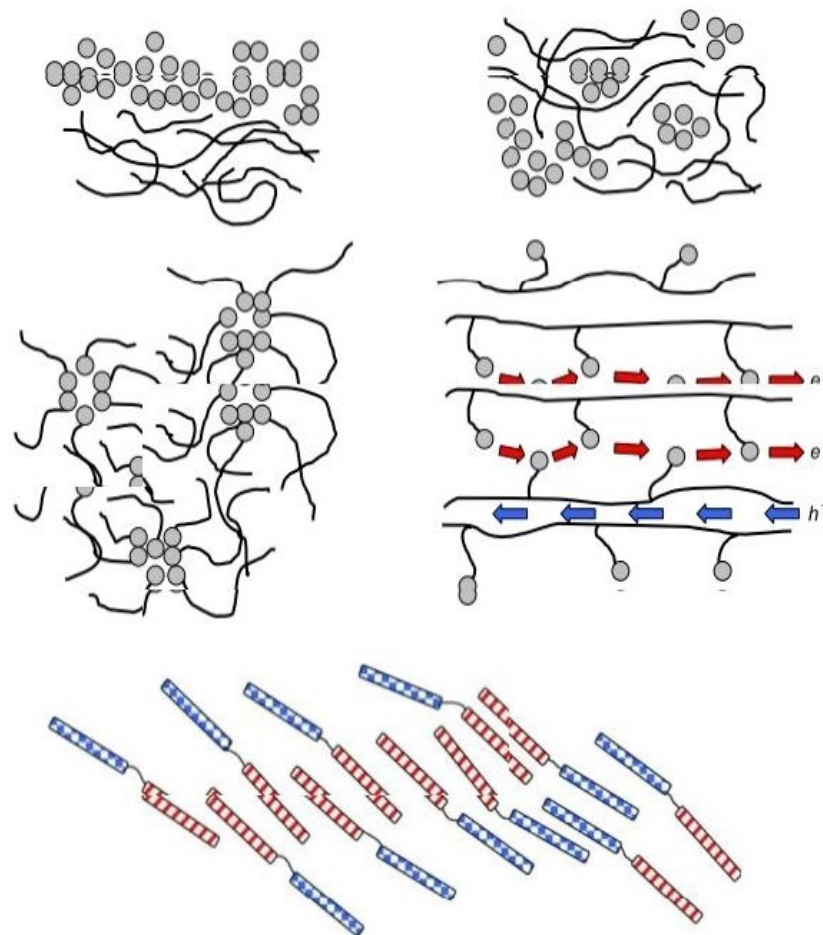
Figure 10: Different morphologies of heterojunction cells. Top, left: Two-layered structure of fullerenes and polymer chains. Top, right: dispersed heterojunction. Middle, left: fullerenes with polymer chains attached. Middle, right: self-assembled layered structure of double-cable polymers. Bottom: self-assembled layered structure of diblock copolymers. The layered structure of double-cable polymers and diblock copolymers are expected to facilitate efficient electron and hole transport. Courtesy of [6]

Also, different configuration of the blend can enhance morphology order and cell efficiency, as shown in [116], where a finger joint ordered configuration is suggested (In Fig. 11 we report the two device architectures for comparison).

37

Moreover, literature reports discussions on to obtain and construct ordered bulk heterojunctions for a better control of the nanomorphology itself, like using self-assembled inorganic nanostructures for the infiltration of conjugated polymers [117,118] or self-organizing diblock copolymers [119,120], where the two blocks carry the different functionalities of donor and acceptor, respectively.
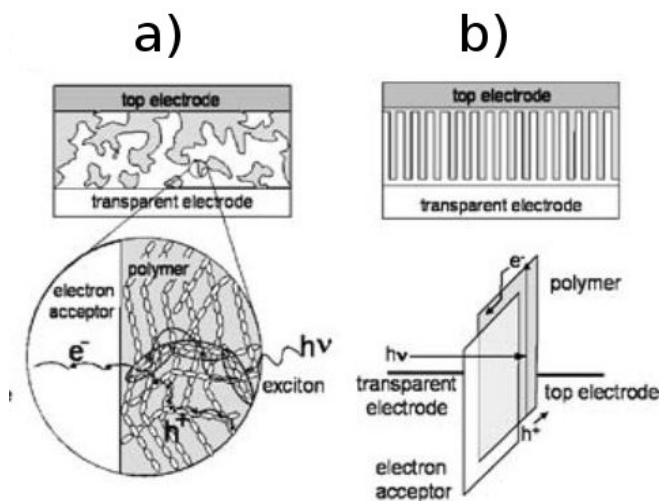

Figure 11: example of device architectures of conjugated polymer-based photovoltaic cells: a) disordered BHJs; b) ordered bulk hetherojuntion. Courtesy of [116]

Also, donor-acceptor blends with (metal) nanoparticles and blend with the polymeric material structured in nanofibers result to be extremely interesting.

In the case of nanofibers, they have attracted interest because of their one-dimensional nanostructures. They can be prepared by various procedures [121], and also they can enhance power conversion efficiency [92,122]. They result to be particularly interesting because they show optimized morphologies directly upon deposition, without annealing or other thermal treatments [123].

Still, conjugated polymers are inherently unstable and as a result limited device stabilities in model OPV systems aged under inert atmospheres has been measured [124,125]. Active layer degradation pathways include changing morphologies [73,126,127], photo-oxidation [89], and carrier accumulation within the active layer [128].

In order to mitigate the degradation pathway related to the active layer structural/morphological changes occurring during prolonged illumination in air, a different approach based on the introduction in the BHJ of metallic nanostructures can be considered. In the experimental part it will be discussed how Ag nanoparticles (NPs) can be incorporated in the P3HT:PCBM active layer,

38

leading to improved structural and morphological properties of the composite blend and, thus, to better PV performance and stability after long periods of continuous illumination in air, compared with the pristine ones.

In conclusion, when trying to improve performances and stability of an organic solar cell, morphological and structural aspect plays a primary role. Studies that make use of novel techniques like joint AFM/EDXR, object of this thesis, can play a crucial role in determining simultaneously the surface/interface morphology and bulk-structure modifications of organic thin-film deposited on substrates, and can be profitably used in organic layers for OPV applications, as will be discussed in the experimental section.

Bibliography

[1] Antonio Luque, Steven Hegedus, Handbook of Photovoltaic Science and Engineering,John Wiley and Sons, 2003

[2] Arnold Hanslmeiquileser, The sun and space weather, Springer, 2002 - 243

[3] B. Sinha, Current Science, Vol. 110, No. 5, 2011, p654-660

[4] European Photovoltaic Industry Association, Solar Generation 6, solar photovoltaic electricity empowering the world,2001

[5] Krebs, F.C.. Materials Science and Engineering B 138, 2007, p106–111.

[6] H. Spanggaard, , Solar Energy Materials and Solar Cells, 83, 2004, p125-146.

[7] S. Schuller, P. Schilinsky, J. Hauch, and C. J. Brabec, Applied Physics A: Materials Science & Processing, 79, no. 1, 2004, p37-40,

[8] X. Yang, J. K. J. van Duren, R. a J. Janssen, M. a J. Michels, and J. Loos, Macromolecules, 37, no. 6, .2004 p 2151-2158,.

[9] X. Yang, J.K.J. Van Duren, M.T. Rispens, J.C. Hummelen, R. a J. Janssen, M. a J. Michels, and J. Loos, , Advanced Materials, 16, 2004, p802-806.

[10] D. Chirvase, J. Parisi, J.C. Hummelen, and V. Dyakonov, Nanotechnology, Nanotechnology 15,2004, p.1317,

[11] T. Savenije, J. Kroeze, X. Yang, and J. Loos, Thin Solid Films, 511-512, 2006, p2-6.

[12] M. Campoy-Quiles, T. Ferenczi, T. Agostinelli, P.G. Etchegoin, Y. Kim, T.D. Anthopoulos, P.N. Stavrinou, D.D.C. Bradley, and J. Nelson, Nature materials, 7, 2008, p158-64.

[13] U. Zhokhavets, T. Erb, H. Hoppe, G. Gobsch, and N. Serdarsariciftci, Thin Solid Films, 496, no. 2, 2006, p679-682,.

[14]Hoppe, H.; Sariciftci, N. S. J. Mater. Chem., 19, 2004, p1924

[15] R. Caminiti and V. R. Albertini, International Reviews in Physical Chemistry, 18, no. 2, 1999, p263-299.

[16] J.M. Nunzi, Comptes Rendus Physique, 3, 2002, p523–542.

[17] J.L. Bredas and G.B. Street, Accunts of Chemical Research, 18, 1985, p309-315.

[18] Blom PWM, Vissenberg MCJM. Materials Science and Engineering: R: Reports. 27(3-4), 2000, p53–94.

[19] A. Pron, Progress in Polymer Science, 27, 2002, p135-190.

[20] N.S. Sariciftci, L. Smilowitz, A.J. Heeger, and F. Wudl, Science 258, 1992, p1474

[21] L. Smilowitz, N.S. Sariciftci, R. Wu, C. Gettinger, A.J. Heeger, and F. Wudl. Phys. Rev. B 47, 40

1993, 13835

[22]S. Morita, A.A. Zakhidov, and K. Yoshino. Solid State Commun. 82, 1992, p249

[23] K. Yoshino, X. H. Yin, S. Morita, T. Kawai, A. A. Zakhidov, 85, 2, 1993, p85-88

[24] C.H. Lee, G. Yu, D. Moses, K. Pakbaz, C. Zhang, N.S. Sariciftci, A.J. Heeger, and F. Wudl Phys. Rev. B 48, 1993, 15425

[25] Hoppe H, Sariciftci NS. Journal of Materials Research. 19(7), 2004, p1924-1945.

[26] A. Mozer and N. Sariciftci, Comptes Rendus Chimie, 9, 2006, p568-577.

[27] Nalwa HS., Handbook of Organic Conductive Molecules and Polymers, 2, ed. By Wiley, Chichester, (1997).

[28]A.C. Mayer, S.R. Scully, B.E. Hardin, M.W. Rowell, and M.D. Mcgehee, Renewable Energy, 10, 2007, p28-33.

[29] S.M. Sze: Physics of Semiconductor Devices (John Wiley & Sons, New York, 1981)

[30] Günes S, Neugebauer H, Sariciftci NS. Chemical reviews. 107(4), 2007, p1324-38.

[30bis] Nelson J. Solid State and Materials Science. 6(1), 2002, p87-95.

[31] Yu G, Heeger AJ. J Appl Phys; 78, 1995, p4510–5

[31bis] Kim, J.; Kim, S.; Lee, H.; Lee, K.; Ma, W.; Huong, X.; Heeger, A. J. AdV. Mater, 18, 2006 p572

[32] Halls JJM, Walsh CA, Greenham NC, Marseglia EA, Friend RH, Moratti SC, Holmes AB. Nature 376,1995, p498–500,

[32bis] M. Reyes-Reyes, K. Kim, J. Dewald, R. López-Sandoval, A. Avadhanula, S. Curran, and D.L. Carroll, Organic letters, 7, 2005, p5749-52.

[33] G. Yu, J. Gao, J. C. Hummelen, F. Wudl, and A. J. Heeger,   Science, 270, no. 5243, 1995 , p1789-1791

[33bis] J. Peet, J.Y. Kim, N.E. Coates, W.L. Ma, D. Moses, a J. Heeger, and G.C. Bazan,   Nature materials, 6, 2007, p497-500.

[34] S.C. Veenstra, W.J.H. Verhees, J.M. Kroon, M.M. Koetse, J. Sweelssen, J.J.A.M. Bastiaansen, H.F.M. Schoo, X. Yang, A. Alexeev, J. Loos, U.S. Schubert, and M.M. Wienk,   Chemistry of Materials, 16, 2004, p2503-2508.

[35] B. Sun, H.J. Snaith, A.S. Dhoot, S. Westenhoff, and N.C. Greenham,   Journal of Applied Physics, 97, 2005, p. 014914.

[36] N. Greenham, X. Peng, and A. Alivisatos, Physical Review B, 54, 1996, p17628-17637.

[37]Qing-Hua Xu, Daniel Moses, and Alan J. Heeger,   Phys. Rev. B. 67, 2003, p245417

[38] Chemical Information Profile for Indium Tin Oxide [CAS No. 50926-11-9], Nat. Toxicology

Program, US Dep. of Health and Human Services, Research Triangle Park, NC, Jun. (2009)

[39] E. Gautier, A. Lorin, J.-M. Nunzi, A. Schalchli, J.-J. Benattar, and D. Vital, Applied Physics Letters, 69, 1996, p. 1071.

[40] B. Paci, a Generosi, V.R. Albertini, P. Perfetti, R. de Bettignies, M. Firon, J. Leroy, and C. Sentein, Applied Physics Letters, 87, 2005, p. 194110.

[41] Y. Kim, a Ballantyne, J. Nelson, and D. Bradley, Organic Electronics, 10, 2009, p205-209.

[42]L. Li, G. Lu, X. Yang, and E. Zhou, Chinese Science Bulletin, 52, 2007, p145-158.

[43]Arbogast J W, Foote C S. Photophysical properties of C-70. J Am Chem Soc, 113(23), 1991, p 8886—8889

[44] Wienk M M, Kroon J M, Janssen R A J, . Angew Chem Int Ed, 42, 2003, p3371—3375.

[45] Kooistra F B, Mihailetchi V D, Hummelen J C, Chem Mater, 18, 2006 ,p3068—3073

[46] S. Gunes , C Linz Inst. Of OSC, Phys. Chem., Johannes Kepler Univ., Linz, Austria, PhD Thesis Sep. 17 2006

[47] L.H. Jimison, M.F. Toney, I. McCulloch, M. Heeney, and A. Salleo, Advanced Materials, 21, 2009, p1568-1572.

[48] E. Perzon, X. Wang, F. Zhang, W. Mammo, J. Delgado, P. Delacruz, O. Inganas, F. Langa, and M. Andersson, Synthetic Metals, 154, 2005, p53-56.

[49] A. Nardes, Electronic Sys. Eng. Dep. of the Polytech. School of the Univ. of Sao Paulo, Sao Paulo, Brazil, PhD Thesis Dec. 18 (2007)

[50] Makinen, A. J.; Hill, I. G.; Shashidhar, R.; Nikolov, N.; Kafafi, Z. H. Appl Phys Lett 79, 2001 p557.

[51] S. Khodabakhsh, B.M. Sanderson, J. Nelson, T.S. Jones, Adv. Funct. Mater. 16, 2006, p95.

[52] A.C. Arias, M. Granström, D.S. Thomas, K. Petritsch, R.H. Friend, Phys. Rev. B, 60, 1999 p1854.

[53] F. L. Zhang, A. Gadisa, O. Inganäs, M. Svensson, and M. R. Andersson, Applied Physics Letters, 84, no. 19, 2004, p. 3906.

[54] Y. Cao, G. Yu, C. Zhang, R. Menon, and A.J. Heeger, Synthetic Metals, 87, 1997, p171-174.

[55] H. Snaith, H. Kenrick, M. Chiesa, and R. Friend, Polymer, 46, 2005, p2573-2578.

[56] C. BRABEC, Solar Energy Materials and Solar Cells, 83, 2004, p273-292.

[57] X. Yang, J. Loos, S.C. Veenstra, W.J.H. Verhees, M.M. Wienk, J.M. Kroon, M.A.J. Michels, and R.A.J. Janssen, Nano letters, 5, 2005, p579-83.

[58] F.C. Krebs and H. Spanggaard, Chemistry of Materials, 17, 2005, p5235-5237.

[59] Chirvaze, D.; Chiguvare, Z.; Knipper, M.; Parisi, J.; Dyakonov, V.; Hummelen,J. C. J. Appl. Phys., 93, 2003 , p3376.

[60] D. Chirvase, J. Parisi, J. C. Hummelen, and V. Dyakonov, Nanotechnology, 15, no. 9, 2004.
42

p1317-1323,

[61] M.A. Green, K. Emery, Y. Hishikawa, and W. Warta, Progress in Photovoltaics: Research and Applications, 19, 2011, p84–92.

[62] C.H. Woo, B.C. Thompson, B.J. Kim, M.F. Toney, and J.M.J. Fréchet, Journal of the American Chemical Society, 130, 2008, p16324-9.

[63] L.-M. Chen, Z. Hong, G. Li, and Y. Yang, Advanced Materials, 21, 2009, p1434-1449.

[64] G. Dennler, M.C. Scharber, and C.J. Brabec, Advanced Materials, 21, 2009, p. 1323–1338.

[65] M. Al-Ibrahim, O. Ambacher, and S. Sensfuss, Applied physics letters, 86, 2005, p201120

[66] Theander, M.; Inganas, O.; Mamo, W.; Olinga, T.; Svensson, M.;Andersson, M. J. Phys. Chem. B 103, 1999, p 7771

[67] R.D.E. Bettignies, J. Leroy, M. Firon, and C. Sentein, Power, 5938, 2005, 1-14.

[68] R.J. Kline, M.D. McGehee, E.N. Kadnikova, J. Liu, J.M.J. Fréchet, and M.F. Toney, Macromolecules, 38, 2005, p3312-3319.

[69] A. Swinnen, I. Haeldersmans, M. vande Ven, J. D'Haen, G. Vanhoyland, S. Aresu, M. D'Olieslaeger, J. Manca, Adv. Funct. Mater. 16, 2006, p760-765

[70] K.M. Coakley and M.D. McGehee, Chemistry of Materials, 16, 2004, p4533-4542.

[71] T. Erb, U. Zhokhavets, G. Gobsch, S. Raleva, B. Stühn, P. Schilinsky, C. Waldauf and C.J. Babec, Funct. Mater., 15, 2005, p1193

[72] G. Kalita, M. Masahiro, W. Koichi, and M. Umeno, Solid-State Electronics, 54, 2010, p447-451.

[73] B. Paci, A. Generosi, V.R. Albertini, R. Generosi, P. Perfetti, R.D. Bettignies, and C. Sentein, Journal of Physical Chemistry C, 112, 2008, p 9931-9936.

[74] N.D. Treat, M. a Brady, G. Smith, M.F. Toney, E.J. Kramer, C.J. Hawker, and M.L. Chabinyc, Advanced Energy Materials,1, 2010, p 82–89

[75] M. Chiu, U. Jeng, C. Su, K.S. Liang, and K. Wei, Advanced Materials, 20, 2008, p2573-2578.

[76] D. Chirvase, J. Parisi, J. C. Hummelen, and V. Dyakonov, Nanotechnology, 15, no. 9, 2004, p1317-1323,

[78] B. Lei, Y. Yao, A. Kumar, Y. Yang, and V. Ozolins, Journal of Applied Physics, 104, 2008, p. 024504.

[79] P.K. Watkins, A.B. Walker, and G.L.B. Verschoor, Nano letters, 5, 2005, p1814-8.

[80] Z. Hu, D. Tenery, M.S. Bonner, and A.J. Gesquiere, Journal of Luminescence, 130, 2010, p771-780.

[81] V. Shrotriya, E. H. E. Wu, G. Li, Y. Yao, Y. Yang, Appl. Phys. Lett. 88, 2006, p064104

[82] G.D. Spyropoulos, M. Stylianakis, E. Stratakis, E. Kymakis, Photonics and Nanostructures -

Fundamentals and Applications, Volume 9, Issue 2, 2011, p184-189,

[83] E.Kymakis, E. Stratakis, E.Koudoumas, C. Fotakis, IEEE Transactions on Electron Devices, 58, issue 3, 2011, p 860-864.

[84] A. J. Morfa, K. L. Rowlen, T. H. Reilly, M. J. Romero, and J. van de Lagemaat, Appl. Phys. Lett. 92, 2008, 013504

[85] C. Min, J. Li, G. Veronis, J. -Y. Lee, S. Fan, and P. Peumans, Appl. Phys. Lett., 96, 2010 133302

[86] W.J. Yoon, K.Y. Jung, J. Liu, T. Duraisamy, R. Revur, F.L. Teixeira, S. Sengupta and P.R. Berger, Sol. Energy Mater. Sol. Cells, 94, 2010, p128–132

[87] Kroon JM. , Nano. 2005;:6-10.

[88] Neugebauer, H. Electrochem. Soc., Proc. 12, 2002, p19-21

[89] Neugebauer H, Brabec C, Hummelen J, Sariciftci N. Solar energy materials and solar cells. 61(1), 2000, p35–42.

[90] A. J. M. Berntsen, P. V. de Weijer, Y, Croonen, C. T. H. F. Liedenbaum, J. J. M. Vleggaar, Philips Journal Research, 51, 1998, p511-525.

[91] Drees, M.; Hoppe, H.; Winder, C.; Neugebauer, H.; Sariciftci, N. S.; Schwinger, W.; Scha¨ffler, F.; Topf, C.; Scharber, C.; Gaudiana, R. J. Mater. Chem. 15, 2005, p5158

[92]Yang X, Loos J, Veenstra S C, Verhees W J H, Wienk M M, Kroon J M, Michels M A J, Janssen R A J. Nano Lett. 5,2005, p579–583.

[94] T. Erb, U. Zhokhavets, H. Hoppe, G. Gobsch, M. Al-Ibrahim, O. Ambacher Thin Solid Films. 511-512, 2006, p483-485.

[95] Brown, P. J.; Thomas, D. S.; Ko¨hler, A.; Wilson, J.; Kim, J. S.; Rainsdale, C.; Sirringhaus, H.; Friend, R. H. Phys. ReV. B 67, 2003, 064203

[96] Ahn, T.; Sein Holta, H. L. Appl. Phys. Lett, 80, 2002, 392

[97] Zhang, F.; Svensson, M.; Andersson, M.; Maggini, M.; Bucella, S.; Menna, E.; Ingana¨s, O. AdV Mater. 13, 2001, p1871

[98] N. Camaioni, G. Ridolfi, G. Casalbore-Miceli, G. Possamai, and M. Maggini, Advanced Materials, 14, no. 23, 2002, p1735-1738,

[99] Reese, Matthew O.; Morfa, Anthony J.; White, Matthew S.;Kopidakis, Nikos; Shaheen, Sean E.; Rumbles, Garry; Ginley, David S.; Photovoltaic Specialists Conference, 2008. PVSC '08. 33rd IEEE 11-16 May 2008 1-3

[100]Reese M.O., Morfa A.J., White M.S., Kopidakis N., Shaheen S.E., Rumbles G., Ginley D.S. Solar Energy Materials and Solar Cells, 92 (7), 2008, p 746-752.

[101] B. Paci, A. Generosi, V. Rossi Albertini, P. Perfetti, R. de Bettignies, and C. Sentein, Solar Energy Materials and Solar Cells, 92, no. 7, 2008. p799–804,

[102] B. Paci, A. Generosi, V. Rossi Albertini, P. Perfetti, R. de Bettignies, C. Sentein, Chem. Phys. Lett. 461 ,2008, p77-81

[103] Y. Kim, a Ballantyne, J. Nelson, and D. Bradley, Organic Electronics, 10, 2009, p205-209.

[104]Kawano K., Pacios R., Poplavskyy D., Nelson J., Bradley D.D.C., Durrant J.R. Solar Energy Materials and Solar Cells, 90 (20), 2006 , p3520-3530.

[105] Nardes A.M., Kemerink M., de Kok M.M., Vinken E., Maturova K., Janssen R.A.J. Organic Electronics: physics, materials, applications, 9 (5),2008, p727-734.

[106] Huang Y-C, Liao Y-C, Li S-S, Solar Energy Materials and Solar Cells. 93(6-7):2009; p888-892.

[107]Padinger, F.; Rittberger, R.; Sariciftci, N. S. AdV. Funct. Mater. 13, 2003, p85-88

[108]Kim WH, Kushto GP, Kim H, Kafafi ZH. Journal of Polymer Science Part B: Polymer Physics. 41(21), 2003, p2522-2528

[109]Vogel M., Strotmann J., Johnev B., Lux-Steiner M.Ch., Thin Solid Films, 511-512,2006, p367-370.

[110] Yang X, Duren JKJ van, Janssen R a J, Michels M a J, Loos J. Macromolecules. 37(6), 2004, p2151-2158.

[111]Duren JKJ van, Yang X, Loos J, Advanced Functional Materials. 14(5), 2004, p425-434.

[112] Schilinsky, P.; Waldauf, P.; Brabec, C. J. J. Appl. Phys. Lett. 81, 2002, 3885.

[113] Hoppe H., Niggemann M., Winder C., Kraut J., Hiesgen R., Hinsch A., Meissner D., Sariciftci N.S. Advanced Functional Materials, 14 (10), 2004 , p1005-1011.

[114] Sean E. Shaheen1, Christoph J. Brabec1, N. Serdar Sariciftci1, Franz Padinger2, Thomas Fromherz, and Jan C. Hummelen3Appl. Phys. Lett. 78, 2001, p. 841

[115]T. Martens, J. D'Haen, T. Munters, Z. Beelen, L. Goris, J. Manca, M. D'Olieslaeger, D. Vanderzande, L. De Schepper, R. Andriessen, Synthetic Metals, Volume 138, Issues 1-2, 2, 2003, p243-247,

[116] H. Hoppe and N. Sariciftci, Photoresponsive Polymers II, no.1, 2008, p1–86

[117] Coakley KM, Liu Y, McGehee MD, Frindell K, Stucky GD (2003) Adv Funct Mater 13, 2003, p301

[118] Coakley KM, McGehee MD (2003) Appl Phys Lett 83, 2003, 3380

[119] Heiser T, Adamopoulos G, Brinkmann M, Giovanella U, Ould-Saad S, Brochon C, van
45

deWetering K, Hadziioannou G Thin Solid Films 511–512, 2006, 219-223

[120] SommerM, Lindner SM, ThelakkatM Adv Funct Mater 17, 2007, p1493–1500

[121] S. Samitsu, T. Shimomura, and K. Ito, Thin Solid Films, 516, 2008, p2478-2486.

[122] S. Bertho, W.D. Oosterbaan, V. Vrindts, J. D'Haen, T.J. Cleij, L. Lutsen, J. Manca, and D. Vanderzande, Organic Electronics, 10, 2009, p1248-1251.

[123] L. Li, G. Lu, and X. Yang, Journal of Materials Chemistry, 18, 2008, p. 1984.

[124] M. O. Reese, A. M. Nardes, B. L. Rupert, R. E. Larsen, D. C. Olson, M. T. Lloyd, S. E. Shaheen, D. S. Ginley, G. Rumbles, N. Kopidakis, Adv. Funct. Mat. 20 (20), 2010, p3476.

[125] Reese, M. O.; Morfa, A. J.; White, M. S.; Kopidakis, N.; Shaheen, S. E.; Rumbles, G.; Ginley, D. S. Solar Energy Materials & Solar Cells. 92, 2008, p746-752

[126] Paci B, Generosi a, Generosi R, Bailo D, Rossi Albertini V. Chemical Physics Letters. 483(1-3), 2009, p159-163.

[127] S. Bertho, I. Haeldermans, A. Swinnen, W. Moons, T. Martens, L. Lutsen, D. Vanderzande, J. Manca, A. Senes, A. Bonfiglio, Solar Energy Materials & Solar Cells 91, 2007, p385.

[128] K. Kawano, C. Adachi, Applied Physics Letters 96 (5), 2010, 053307

[129] Mikkel Jørgensen, Kion Norrman, Frederik C Krebs, Solar Energy Materials and Solar Cells (2008) Volume: 92, Issue: 7, Publisher: Elsevier, Pages: 686-714

[139] R. de Bettignies, J. Leroy, S. Chambon, M. Firon, C. Sentein, L. Sicot, L. Lutzen, Proc. SPIE 5464 (2004) 122.

[131] R. de Bettignies, J. Leroy, S. Chambon, M. Firon, C. Sentein, Sicot, L. Lutzen, Proc. SPIE 5520 (2004) 216.

[132] R. Pacios, A.J. Chatten, K. Kawano, J.R. Durrant, D.D.C. Bradley, J. Nelson, Adv. Funct. Mater. 16 (2006) 2117.

[133] K. Kawano, R. Pacios, D. Poplavskyy, J. Nelson, D.D.C. Bradley, J.R. Durrant, Sol. Energy Mater. Sol. Cells 90 (2006) 3520.

[134] K. Norrman, N.B. Larsen, F.C. Krebs, Sol. Energy Mater. Sol.Cells 90 (2006) 2793.

[135] H. Derbal-Habaka, b, C. Bergeretc, J. Cousseauc, J.M. Nunzi, Solar Energy Materials and Solar Cells Volume 95, Supplement 1, May 2011, Pages S53-S56

[136] Lawrence F. Drummy, Robert J. Davis, Diana L. Moore, Michael Durstock, Richard A. Vaia‡, and Julia W. P. Hsu, Chem. Mater., 2011, 23 (3), pp 907–912

[137] Jae Kwan Leea, Ue Jin Leeb, Myung-Ki Kimb, Sang Ho Leeb, Kyung-Tae Kangb, Thin Solid Films Volume 519, Issue 16, 1 June 2011, Pages 5649-5653

[138] M. Glatthaar, N. Mingirullim, B. Zimmermann, T. Ziegler, R. Kern, M. Niggemann, A. Hinsch, A. Gombert, Phys. Stat. Sol.A 202 (2005) R125.

[139] C. Melzer, V.V. Krasnikov, G. Hadziioannou, Appl. Phys. Lett. 82 (2003) 3101.

[140] C.R. McNeill, C.J.R. Fell, J.L. Holdsworth, P.C. Dastoor, Synth. Met. 153 (2005) 85.

- Chapter II -

Experimental Methods

2.1 Energy dispersive X-ray Spectroscopy

Information about the atomic structure of a sample can be gained by observing the modulation of the intensity spectrum of a probe whose wavelength is comparable with the interatomic distances. If the probe is an electromagnetic radiation, the wavelength is in the X-ray range.

When X-rays interact with matter, the incident photons can be (i) absorbed, (ii) inelastically scattered or (iii) elastically scattered. The absorption process occurs when photons are absorbed by matter, and can generate various effects like the photoelectric effect, which occurs when photons interact with matter with resulting ejection of electrons (photoelectrons or Auger Electrons) from the matter. The Compton effect or Compton scattering, also known as incoherent or inelastic scattering, occurs when the incident X-ray photon ejects a electron from an atom and an X-ray photon of lower energy is scattered from the atom. In this process, the incident X-ray changes direction and loses energy, imparting that energy to the electron. The elastic scattering, also known as Rayleigh, Thomson, coherent, or classical scattering, occurs when the X-ray photon interacts with the whole atom so that the photon is scattered with no change in internal energy to the scattering atom, nor to the X-ray photon. This effect is minor to when related to absorption, but is the primary effect which makes X-ray diffraction possible.

The incident X-ray beam scattering can be considered perfectly elastic, starting from the assumption that electrons are somehow integral with their nuclei.

The elastic contribution to the scattering is a function of the momentum Δp exchanged by the radiation with the atomic tightly bound electrons. For a generic system Δp, is a vectorial quantity, having three components. In the case of isotropic systems, the intensity only depends on the modulus of Δp and not on its orientation, and a scalar quantity q, called *scattering parameter* which

48

represents the modulus of Δp expressed in **h** units, can be defined as $q = \frac{1}{2} k \sin \vartheta$ **w**here 2ϑ is the total scattering angle and k the modulus of both wavevectors $\mathbf{k}_1$ and $\mathbf{k}_2$.

Spectroscopy patterns can thus be drawn by plotting the scattered intensity as a function of the free parameter q only. Fig. 1 shows the relation between q and the experimental quantities.
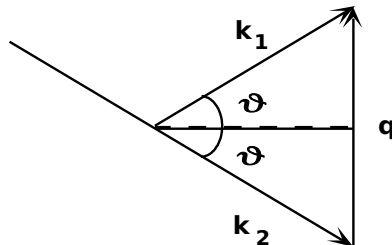

Figure 1: Diagram of the exchanged wavevector

Since the scattering is elastic, the energy E of the radiation remains unchanged during scattering, and as the wavevector (wave number) is proportional to energy, it can vary its direction but not its modulus, that is the X-ray beam can change its direction but not its wavelength. Being E proportional to **k**, the following equation holds: $q(E, \vartheta) = \alpha E \sin \vartheta$ where the constant α is 1.014 [Å^{-1} / KeV]. The preceding relation is another way of expressing the well-known relation $q = \frac{4\pi}{\lambda} \sin \vartheta$, where λ is the radiation wavelength. [1]

As q is function both of E and ϑ, when using an X-ray spectroscopy technique, two methods are available to perform a scan of q and to draw the scattered intensity profile as a function of it:

1) The first is to use a monochromatic beam (E fixed), for instance a fluorescence line produced by a laboratory X-ray tube, and carry out an angular scan (Angular Dispersive, AD)

2) The second consists of utilizing a continuous spectrum radiation, often called *white* by analogy with the visible light, for example the Bremmstrahlung of an X-ray tube, the scattering angle being fixed (Energy Dispersive, ED)

The former alternative is the conventional method and the distinction between the two methods was made in the late sixties [2]. The latter, which requires a certain amount of work to refine the diffraction data, is less conventional but can be profitable in some case. It is worth comparing the two techniques in order to illustrate quality and defects.

The merits of ED can be summarized as follows:

1.*The accessible region in the reciprocal space is wider.* In the AD technique, the maximum q value

is limited by the condition $\sin\vartheta \leq 1$, and by the upper limit $qmax\sim 19\ \text{Å}^{-1}$, imposed by physic-technical limitations (targets producing fluorescence lines of higher energy are not available). In the ED methods, once the scattering angle is fixed, $qmax$ is determined by the highest energy component contained in the white spectrum. For example, if the power supply voltage is 50 KV, the maximum energy is, by definition, 50 KeV. At an angle of 40°, theoretical $qmax$ is 30 Å^{-1}.

2.*Reduction of the acquisition time.* The Acquisition time depends on the total scattered intensity. As the intensity concentrated in the fluorescence line (in AD) is, in typical working conditions, from one to two orders of magnitude lower than the intensity distributed in the entire continuous spectrum (in ED), this is also, roughly, the ratio between the acquisition times in the two cases.

3.*Steady apparatus during data collection.* This simplifies the experimental procedure, since the beam hits always the same point and unlike AD, no movements compromise the alignment, which may induce systematic errors. Hence, also very small samples can be used. Furthermore, complex and cumbersome devices can be installed, such as high pressure or variable temperature cells, even though the path to the sample is very narrow: it is sufficient that the incoming hole of the device is wider than the transversal section of the X-ray beam.

4.*Parallel collecting of the spectrum points.* In the AD methods, spectrum points are collected sequentially, and the scanning rate is proportional to the angular speed of the diffractometer arms and to the acquisition time. Vice versa, ED permits a multiplex acquisition: the points are collected simultaneously at each value of q, and it can be strongly advantageous in the case of sample which dynamically change their structural configuration, as changes at different values of q are probed simultaneously.

On the other hand some drawbacks must be noticed:

1.*Decrease of q resolution.* The logarithmic derivative of q is $\frac{\Delta q}{q} \simeq \frac{\Delta E}{E} + \cot\vartheta\ \Delta\vartheta$ so the relative q resolution is then composed by two terms. The first contribution is due to the energy resolution of the detector and of its electronic chain; the second, originates from the angular divergence of the X-ray beam. In AD, only the latter is present. However while it can be a serious drawback in the case of crystallographic experiments, where accurate measurements are needed, in the case of not-crystalline or disordered system the effects are negligible. In the case of X-ray Reflecometry, the lower resolution is not a serious drawback, since patterns are characterized by broad modulations.

2.*Complex data processing.* elastic and inelastic scattering, absorption, polarization, and all other phenomena involved in the diffraction experiments, are energy dependent. Each chromatic component contained in the spectrum of the secondary beam has to be analysed separately.

3.*Limited accessible range in q space at fixed angle.* At a given ϑ angle and for a given energy

50

E_{MAX}, this range should span from zero to $qmax = a E_{MAX} \sin\vartheta$. From this point of view a change in ϑ which acts as an instrumental parameter to be set before the beginning of the measurement, corresponds to an expansion or contraction of the accessible window in the reciprocal space. Hence when, to cover the q-interval of interest, several patterns must be collected in correspondence to a set of angular value, the final join performed to recombine them in a unique pattern must be carried out by considering that, in the region where the spectra are overlapped, a fixed q value corresponds to different energies, being the spectra collected at different angles [3].

In conclusion, drawbacks can be more or less remarkable depending on the measurements to be carried out and on the samples studied. The ED techniques usually become really profitable in the case of measurements which include dynamical changes of the sample exposed to temperature or other environmental variations, which often involve the use of heat cell or other cumbersome devices; also, it is advantageous in the case of non-crystalline samples, disordered samples, or other devices for which extremely accuracy in q is not required.

In the following paragraphs we're going to describe the techniques used in the present work.

2.1.1 Energy Dispersive X-ray Diffraction

X-ray Diffraction is a spectroscopic technique based on X-rays that can enable one to gather information about the crystallographic structure, chemical composition, and physical properties of materials and thin films. It is of great interest when one needs to have structural information on single and multi-layered complex systems with materials which have a certain degree of structural order, as the case of organic photovoltaic cells. On those systems, the diffraction allows to determine the preferred orientation of substrate-anchored polymer thin films, the aggregation of active material components in crystallites and, if used in situ in a dynamical way (i.e. change of environmental parameters like temperature or pressure during the measurements), it can show the evolution of the parameters which characterise the system, in function of time.

X-ray Diffraction theory by Thomson and Debye describes the modulation of the intensity spectrum, due to the interaction with the sample, as the effect of coherent superposition of waves elastically scattered by atomic core electrons, which are regarded as small antennas scattering with a dipolar distribution.

Even though this approach is completely classic, it is sufficient to explain the features and the characteristics of diffraction patterns and to get the required structural information [4]. Quantum effects at these energies are still small, can be considered as perturbations and can be taken into account by introducing some suitable corrections connected to the inelastic contribution to the scattering of the outer shell electrons, that is the Compton effect.

51

As first assumption we can consider atomic electrons interacting with X radiation as if they were isolated and if they elastically scatter the incident wave. In this case we have simple scattering and according to Thomson's theory, the incident wave is plane and electrons behave as a classic vibrating dipoles. They re-emit waves with the same frequency as the incident ones and with amplitudes proportional to the sine of the deflection angle between the electrical field and the direction of observation. In Fig. 2, **k1** and **k2** are incident and scattered wavevector, respectively, and **q** is their difference.

To describe the overall effect of the interference, we must consider a system with at least two electrons where phase shift of scattered radiation must be evaluated. It can be done in the position domain, by calculating the length of the optical path of each scattered radiation. In fig 2 the two waves coming from the same direction (1 and 2), with the same length, are scattered by two electrons A and B.

They exhibit a phase shift, with respect to each other, which depends on the positions of the electrons and on the direction of observation. If the two electrons are connected by the vector **r** , the phase shift between the scattered waves is: $k\Delta x = k(\hat{k}_1 \cdot r - \hat{k}_2 \cdot r) = k(k_1 - k_2) \cdot r = q \cdot r$ where **q** is the exchanged wavevector.
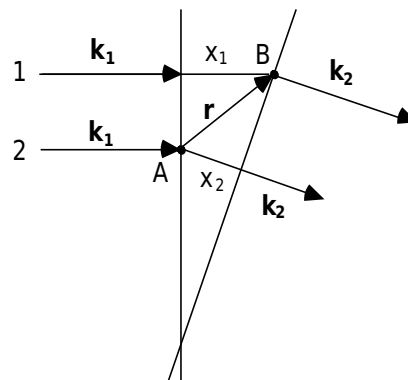

Figure 2: scattering of two electrons at distance r

Hence it demonstrate that the elastically scattered radiation shows a well defined phase difference induced by the position of scattering atoms. As an effect of this phase coherence they also interfere with each other[1] modulating the scattered (observed) intensity of the detected wave. Moreover, its value is affected by several effects (polarization, presence of cell or devices in which the sample is contained, etc). In conclusion, as shown in [5,6], the final master equation of diffraction of observed intensity can be written as:

$$I_{\text{Obs}}(E,E',\vartheta)=KI_0(E)P(E,\vartheta)A_{\text{Coh}}^{\text{Tot}}(E,\vartheta)[I_{\text{Coh}}(E,\vartheta)+.$$

$$\frac{E'I_0(E')P(E',\vartheta)A_{\text{Inc}}^{\text{Sam}}(E,E',\vartheta)}{EI_0(E)P(E,\vartheta)A_{\text{Coh}}^{\text{Sam}}(E,\vartheta)}I_{\text{Inc}}(E',\vartheta)]$$

$$+A_{\text{Coh}}^{\text{Sam}}(E,\vartheta)\cdot I_{\text{Emp}}(E,E',\vartheta)$$

where $A_{\text{Coh}}^{\text{Tot}}(E,\vartheta)=A_{\text{Coh}}^{\text{Sam}}(E,\vartheta)\cdot A_{\text{Coh}}^{\text{Cel}}$

In this equation inelastic scattering is taken into account as well, and E' is the photon energy before the deflection due to interaction with the sample, E after interaction. The quantity $\Delta E=E'-E$ can be determined with the Compton shift equation as shown in [6].

K is a constant different for each scattering angle, it contains the factor $(r_0/R)^2$ and all the quantities that modify the photon flux at the detector (X-ray tube to sample distance, sample-to-detector distance, positions of the collimation slits and the surface they delimit etc).

I_0 is the intensity of the primary beam in function of energy.

P is the polarization of the scattered beam, for the coherent and incoherent contributions.

A is the correction due to absorption, and the superscripts *sam, cell,* correspond to sample and cell respectively.

The subscript *emp* refers to the empty cell.

The subscripts *coh* and *inc* refers to coherent (elastically scattered) and incoherent inelastically scattered) radiation related to Absorption and scattered Intensity. The main difference between $I_{coh}(E,\vartheta)$ and $I_{inc}(E',\vartheta)$ is that the latter has no interference modulation.

Our purpose is isolating the term I_{Coh} which contains i(q), that is the structural information on the sample. We can define a new quantity $\tilde{I}_{\text{Obs}}(E,E',\vartheta)$ as follows:

$$\tilde{I}_{\text{Obs}}(E,E',\vartheta)=K[I_{\text{Coh}}(E,\vartheta)+\frac{E'I_0(E')P(E',\vartheta)A_{\text{Inc}}^{\text{Sam}}(E,E',\vartheta)}{EI_0(E)P(E,\vartheta)A_{\text{Coh}}^{\text{Sam}}(E,\vartheta)}I_{\text{Inc}}(E',\vartheta)]$$
temporarily neglecting the sample holder contribution.

In this form the equation is constituted by two terms on the right hand: the first is related to coherent contributions, the second to incoherent. It is then more simple to handle. Some observations can hence be done: first, it must be remembered that the measurements are carried out at a constant angle and the dependence of $\tilde{I}_{\text{Obs}}(E,E',\vartheta)$ on ϑ is parametric and disappears when the angle is fixed. Second, all the contributions on the right hand side can be measured and are supposed to be already known, so $\tilde{I}_{\text{Obs}}(E,E',\vartheta)$ is a known quantity as well. Third, E' is a function of E and ϑ, according to the Compton shift equation, thus the only free variable is E which is given in

53

a diffractogram.

Thus, the coefficient of I_{Inc} is also known and I_{Inc} itself can be theoretically calculated. The term K, which varies with the angle: $K=K(\vartheta)$, can be calculated in exact or approximate form as described in [5].

Advantages of ED mode for the study of films for OPVs

The energy dispersive technique has several advantages which have been fundamental for the type of sample studied in the present work.

1.First, it has been shown that theoretically it enable to remove or simplify the terms depending on the scattering angle, which in the energy dispersive mode is fixed.

2.Second, as the acquisition time is relatively short compared to the angular dispersive option, it allows to carry on in-situ experiments which monitor the sample structural variation in reasonable time intervals (from minuets to hours).

3.Third, with complex multi-layered sample for organic photovoltaics, which are the subject of this work, mechanical errors or movements, even if minimal, can interfere on the diffraction conditions an thus compromise the experiment or giving as result diffractograms affected by artifacts effects, which doesn't occur when arms are fixed as in EDXD.

4.Fourth, the use of relatively high energy, allows to investigate in a reasonable time multi-layered systems with layers of non-light metallic elements (Au, Ag, ITO).

In conclusion, the use of Energy Dispersive mode can enable one to carry on laboratory experiment in a reasonable amount of time and with reasonable precision on complex systems, without the strict necessity of requesting beam time in large facilities like synchrotrons.

2.1.2 Energy Dispersive X-ray Reflectometry

Through the use of X-ray reflectometry technique (XRR) it is possible to study monolithic and multilayered film properties on a mesoscopic scale. This technique result to be a powerful method for several reason: it is sensitive to electron density gradients regardless of the crystalline nature of the system investigated [7]; it allows one to gather informations (roughness) on the free surface and the (buried) interface(s) with great accuracy (at the Ångstrom resolution)[8]; it also enables to determine the mass density, the thickness and the roughness of thin layers along the direction normal to the specimen surface [9]. Those information can be profitably used in the case of organic

54

multilayered photovoltaic cells, where a particular attention is devoted to the understanding of interface phenomena between layer of different materials.

X-ray reflectometry is based on the total reflection phenomenon, common for all travelling waves. While, for light, total reflection occurs when light waves travel from an optically dense medium (high index of refraction) to a less dense (low index of refraction) medium[10], determining total reflection on *internal* surfaces of materials (of glass, for example), for X-rays, for which refractive index of most materials is smaller than that of air, total *external* reflection occurs. The total reflection is accompanied by an evanescent wave propagating along the interface between the two media and being exponentially damped into the less dense medium [11]. This fact enables one to use the reflectometry as a tool for physical and material science studies because an X-ray beam impinging a sample (either in air or in a vacuum) can be totally reflected by it, carrying morphological information on the reflection surface.

When a two-medium system is considered, this phenomenon can be described at a first approximation by Snell's law, which in reference to Fig.3 , can be written as : $n_1 \cos\alpha_i = n_2 \cos\alpha_r$

where α_i is the incidence angle of the primary X-ray beam, n_1 the refractive index of the first medium and α_r and n_2 the reflection angle and the refractive index of the second medium
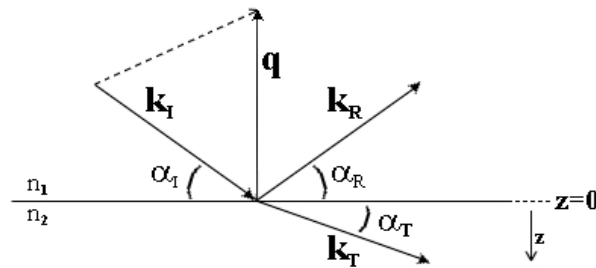

Figure 3: Geometry of specular reflectivity. The initial and final wave vector k_i and k_f define the scattering plane.

If $n_1 > n_2$, then $\alpha_i > \alpha_r$, $q = k_r - k_i$ consequently, there must be a value of α_i called critical angle α_c so that $\alpha_r = 0$. In this case $\cos \alpha_c = n_2 / n_1$. If the first medium is air, then the expression becomes: $\cos \alpha_c = n_2$. In these conditions the beam will not be refracted anymore but totally reflected.

In case of X-ray, at a first approximation, this is still true. Only a change is required: a different definition of the refractive index [12]. The (complex) index of refraction in the X-ray region can be written as: $n = 1 - \delta - i\beta$, where the real term δ is associated with the dispersion, and the imaginary term β with the absorption:

$$\delta = (\lambda^2/2\pi) \rho r_0 Z^2$$

$$\beta = (\lambda/4\pi)\,\mu$$

where λ is the incident wavelength, ρ the material density, r_0 the classical electron radius, Z the atomic number and μ the linear absorption coefficient [13].

Both terms are small compared to unity (about 10^{-4} to 10^{-8}) in this energy region.

β is usually much smaller than δ.

δ is a positive quantity for all elements in the energy region away from the absorption edges, so the real part of the refractive index is smaller than unity. Total reflection of X-rays can thus be observed in the region of incident angles below the critical angle of total reflection [14]: .

Hence, Snell law for an incident X-ray beam can be rewritten substituting the correct expression of the refractive index n into the equation

$\cos\alpha_c = n_2$, thus obtaining:

$\cos\alpha_c = 1 - (\lambda^2/2\pi)\,\rho r_0 Z^2 - i(\lambda/4\pi)\,\mu$

As the refractive index in case of X-rays is very close to unity, then the critical angle is very small [15]. It implies that the absorption effect can be neglected [16], and also that, expanding the expression till the third order in Mc Laurin series, for a given material at Z and ρ fixed, the previous expression becomes $\alpha_c/\lambda = $ constant.

Since the scattering parameter (momentum transfer) is $q \cong 4\pi\sin\alpha/\lambda$, the X-ray total reflection occurs when the critical wave vector value $q_c = \alpha_c/\lambda$, is reached.

Therefore, at a very good approximation, in a total reflection experiment far from the absorption edge, the relevant parameter is not the critical angle alone, since it changes with the X-ray energy, but rather the critical angle to wavelength ratio, i.e. the critical value of the scattering parameter q_c [17], where:

$$q = 4\pi\sin\alpha/\lambda = E\sin\alpha / hc = K\,E\sin\alpha$$

This approximate model show us that X-ray reflectometry can be used for the determination of surface and interface roughness, layer thickness of thin films and multilayer samples, and near-surface density gradients and layer density.

These information should be however determined quantitatively, so an accurate fitting procedure based on the more rigorous theoretical model must be performed. Those models take into account reflection and transmission coefficients as derived from electromagnetic wave propagation theory, the Fresnel coefficients [10]; also the multi-layer case, through the use of the Parratt formalism [8], is taken into account; this formalism is valid only in the case of ideal sharp surfaces and interfaces, and relates the reflected and transmitted amplitude, R_j and T_t, respectively, via:

56

$$X_j = \frac{R_j}{T_j} = \exp(-2\,\mathrm{i} k_{z,j}\, z_j \frac{)\cdot R_{j,j+1} + X_{j+1}\cdot\exp(2\,\mathrm{i} k_{z,j+1}\, z_j)}{1 + R_{j,j+1}\, X_{j+1}\cdot\exp(2\,\mathrm{i} k_{z,j+1}\, z_j)}$$

where $R_{j,j+1}$: $R_{j,j+1} = \dfrac{k_{z,j} - k_{z,j+1}}{k_{z,j} + k_{z,j+1}}$ is the Fresnel coefficient of interface j, and $k_{z,j} = k\sqrt{n_j^2 - \cos^2\alpha_I}$

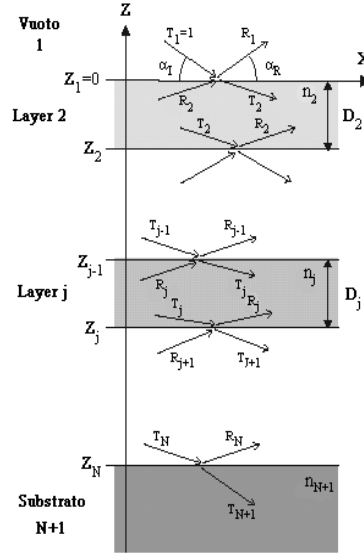indicates the wave vector component of the j layer along the z direction (in Fig. 4).

Figure 4: A schematic diagram showing the definitions used in the Parratt formalism for a multilayered film.

Finally, to introduce the effect of rough surfaces and interfaces into the reflectivity model, a roughness factor Q_j like the Debye-Waller factor [18] or Nevot-Croce Factor [19] must be used.

$Q_j = \exp(-2k^2_{z,j}\,\sigma^2_j)$ (Debye-Waller factor)

$Q_j = \exp(-2\mathrm{k}_{z,j} k_{z,j+1} \sigma^2_j)$ (Nevot-Croce Factor)

In Fig.5, an example of reflectivity patterns is shown, in the two cases of single layer and double layer; the differences between a Fresnel reflectivity pattern (on the left) and the reflectivity collected from a thin film on a substrate (right) are evident.

In the first case the reflected intensity decays after the critical q value more than exponentially following the Porod's "q^{-4}" law valid in case of large q [5]. The critical parameter is easily deduced by the position of the reflection edge.

In the second case the characteristic Kiessig fringes [20] are visible and the Parratt model calculated for two layers can be applied in order to deduce all morphological information. Those fringes are
57

intensity oscillations due to the interference of waves, which are reflected from different interfaces within a system, and can be related to the thickness d of the film with the equations: $d \approx 2\pi / \Delta q_z,$
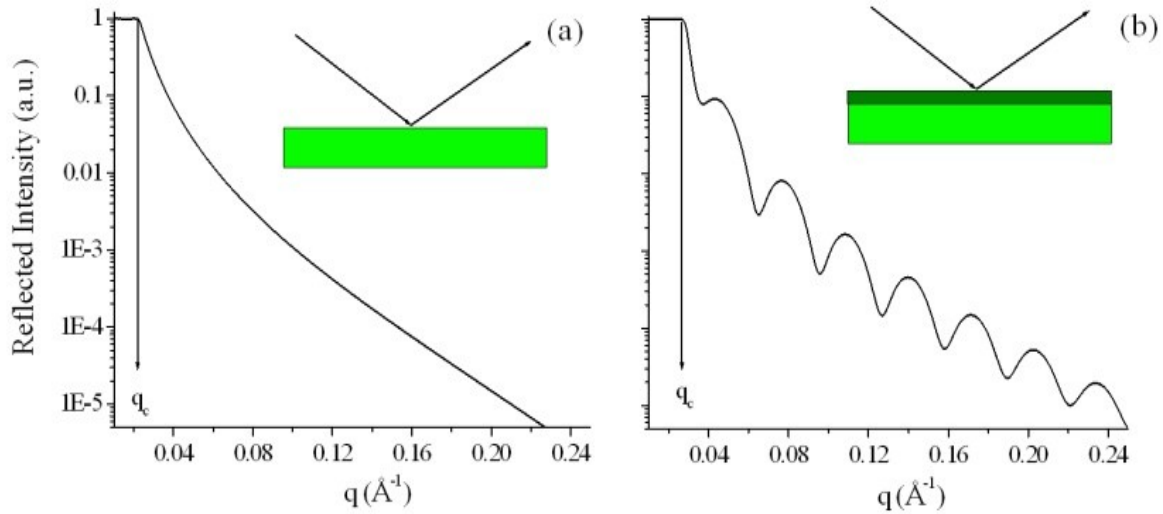

Figure 5: An example of reflectivity patterns is shown, in the two cases of single layer and double layer

Advantages of ED mode

Since a reflectivity measurement consists in collecting the reflected intensity as a function of the scattering parameter [21], $q = 4\pi \sin\alpha/\lambda = KE \sin\alpha$, which depends on the radiation energy and on the scattering angle, it is possible to perform the q scan and to draw the reflected intensity profile as a function of it also in the energy dispersive mode, and not only in the most common angular dispersive (AD) mode. The advantages of the ED mode in X-ray reflectometry are remarkable and the disadvantages become almost irrelevant.

The experimental geometry remains in fact unchanged during data collection, which is a fundamental advantage for in situ studies [22-23]: in the grazing incidence geometry required in reflectivity measurements, any misalignments may induce relevant relative errors during the angular scan necessary to collect the reflectivity pattern in the Angular Dispersive mode. As in situ ED X-ray reflectivity the sample is not removed from its location and no instrumental movements are required, misalignment problems are prevented and film morphology modifications to be followed with extreme accuracy [24,25].

The most important feature may be related to the resolution in the k space. A single spectrum collected at fixed angle, using the whole white beam of a conventional W anode X-ray tube, covers typically a range of some 10^{-2} Å^{-1}. A few hundred points, whose number is decreased by a factor 5 (groups of 5 adjacent points are summed to encounter the SSD resolution), are collected in this range.

58

To get the same resolution using the k_α of a Cu anode tube as primary beam, in the same k range, angular steps of 0.001° are required, and even if such angular movements may be performed by extremely accurate goniometers, the time expense to collect all points constituting the reflectivity pattern, would not allow to perform real time measurements.

The increased signal intensity and the parallel collection of the spectra, together with the fixed geometry, make the Energy Dispersive mode a powerful laboratory reflectometry technique to perform in situ and time resolved measurements.

On the other hand, the decrease in q resolution due to the uncertainties on both the angle and the energy which is the main drawback of the ED mode in diffraction measurements, does not significantly affect the reflectometry patterns, because they are characterized by broad peaks or long period oscillations.

2.2 Atomic Force Microscopy

Atomic Force Microscopy (AFM) technique belongs to the wider family of scanning probe microscopy (SPM), which is a branch of microscopy that deals with the creation of images of surfaces using a physical probe that scans a given specimen.

The basic working principle is very simple: a sharp tip (the probe) with a radius of curvature on the order of nanometers, is mounted on a cantilever. Then the tip is brought in proximity of the surface of the studied specimen, and the forces interacting between the tip and surface cause the deflection of the cantilever according to Hooke's law [26]. The intensity of such interaction is measured in real time by force sensors, and, through the use of electronic apparatus, the topography of the surface is reconstructed [27,28].

An AFM measurement can be carried out in three different modes:

• In *contact* mode the tip scans the surface of the sample at contact distance (Ångstrom's order), and the force between tip and surface is kept constant by an electronic feedback system. In this mode it is also possible to estimate the friction coefficient. Although contact mode allow one to have the best image quality, it could damage samples whose surface is made of soft matter.

• In *non contact mode,* the tip is not in contact with the sample surface, and the cantilever is oscillated at a frequency near to its resonance frequency. This mode doesn't suffer of tip or sample degradation.

• In *tapping mode* the cantilever is oscillated at a frequency near to its resonance frequency as well, but before reaching the maximum of oscillation's amplitude, the tip gets in contact with the sample surface so that Van der Waals force, dipole-dipole interaction, electrostatic forces, and other forces, cause the amplitude of this oscillation to decrease as the tip gets closer to the sample. Measuring the variation of phase and amplitude it is hence possible to obtain (i) a topographic image and (ii) a "phase lag" image which allows to discriminate different types of materials.

Moreover, AFM technique has the advantage of performing surface characterization with nanometrical resolution in a non-destructive way and without surface preparation. Again, it is extremely useful on materials like organic thin films used as active materials in OSC, in which surface components are not stable and sometimes subject to wear (ageing, friction strains, damages), and must be characterized while preserving their integrity[29].

2.3 Joint EDXR/AFM

Microscopy and X-ray scattering are very different techniques, which are also based on different physics phenomena. However, they both share the ability of imaging objects at high resolution: the former probes the samples structure in the direct (physical) space, the latter provides a representation in the reciprocal space [30]. In particular X-rays, as seen in the previous paragraphs, can be also used to study the characteristics of a surface by utilizing their reflection properties at the interface between two means having different electronic densities [31], i.e. using the X-ray Reflectometry technique.

Both X-ray reflectometry and AFM microscopy can be used to study the surface roughness ρ of a sample, although using two different physical effects. From an AFM image, indeed, the surface roughness is obtained by applying the definition of ρ itself, that is the rot mean square of the height fluctuations (around the height average value) at the surface. From an X-ray Reflectometry spectra, on the other hand, ρ can be calculated as the slope of the reflection curve above the total X-ray reflection edge [32].

Theoretically, the two techniques should be equivalent, but when comparing the experimental data, discrepancies between the two numerical values of roughness may be observed, which can be caused by different experimental errors that may occur, and by the fact that one technique gives the ρ mean value (EDXR), while the other a local ρ value (AFM). By comparing the data collected in both ways is possible to prevent mistakes in interpreting the results. In the case of samples undergoing modification for which time-resolved measurements are required, the possibility to compare results given by different techniques can be essential.

An example is given in the case in which this joint technique is used to study the surface morphology of a sample: AFM can give local information about the surface arrangements, but as it samples small portions of the surface, to obtain statistically meaningful data several zones must be measured; X-ray reflection, on the other hand, provides the (average) surface roughness of a large portion of surface, even though it is not able to describe what kind of surface arrangement corresponds to such roughness.

Also, when we apply the joint technique to the study of thin films deposited on substrates, as the case of OSC where substrate plays a functional role, acting as either an electrode or a current collector [25,33], reflectometry gives a reflection pattern whose fit allows in theory to discriminate the surface and interface roughness parameters, ρ_s and ρ_i respectively. From the practical point of view, analytical expressions of ρ_s and ρ_i are tightly entangled, so while their joint value can be

accurately determined, their individual values are rather uncertain. An independent determination of one of them, for instance the surface roughness by AFM, allows to separate the two contributions.

The possibility of simultaneous AFM/EDXR measurements is hence to be regarded as new opportunity: this is particularly true when the modifications of the morphological parameter (film thickness and roughness) over time are to be followed in situ, which cannot be done by using the two techniques separately because, like in the case of OPV cells active layers [34,35], these materials can exhibit a bad stability upon working or ambient conditions.

2.4 Fourier Transform Infrared Spectroscopy

Fourier Transform Infrared Spectroscopy (FTIR) is one of the most common infrared spectroscopy techniques used to determine the molecular composition of a specimen.

Infrared spectroscopy is a technique able to detect the non symmetrical functional groups of a molecule [36], in which the electric dipole moment of the molecule changes during the vibration due to absorption of infrared radiation. An infrared spectrum indeed is commonly obtained by illuminating a sample with infrared radiation and determining what fraction of the incident radiation is absorbed at a particular energy. The energy at which any peak in an absorption spectrum appears, corresponds to the vibration frequency of a sample part and represents a molecular fingerprint of the sample. Hence this technique enables one to make qualitative analysis, that is to identify unknown materials, to determine the quality or consistency of a sample and, through the use of algorithms and with a reference specimen, also a quantitative analysis [37] which helps to determine the amount of components in a mixture.

The original infrared instruments were of the dispersive type [38]. These instruments separated the individual frequencies of energy emitted from the infrared source, through the use of a prism or grating. The detector measures the amount of energy at each frequency which has passed through the sample. This results in a spectrum which is a plot of intensity vs. frequency.

Fourier Transform Infrared (FT-IR) spectrometry was developed in order to overcome the limitations encountered with dispersive instruments, the main difficulty being the slow scanning process. Then, a solution was developed which employed a very simple optical device called an interferometer which allowed to measure all of the infrared frequencies simultaneously. The resulting signal, called an interferogram, contains information about all frequency components of the direct (intensity vs. wavelength) spectrum, which can be decoded in the direct space using Fourier transformation [36,38] .

Fourier transform infrared spectroscopy is preferred over dispersive or filter methods of infrared spectral analysis for several reasons: (I) it is a non-destructive technique, (ii) it provides a precise measurement method which requires no external calibration, (iii) it can increase speed collecting a scan every second, (iv) it can increase sensitivity – one second scans can be co-added together to ratio out random noise, (v) it has greater optical throughput, (vi) it is mechanically simple with only one moving part [38].

When studying complex sample like organic materials for OPVs, the use of FTIR spectroscopy can

support, validate and add information about chemical compositions, bondings, configurations and conformations of the specimen [39], as a complement to the results of other techniques used in combination with it. These information can be used for a better comprehension of the process the cell is subject to when exposed to particular environmental conditions like humidity or heat [40].

Bibliography

[1]James, R.W., 1982, The optical principles of the diffraction of X-rays (Woodbridge, connecticut: ox-Bow Press), p. 464

[2] B. C. Giessen, G. E. Gordon, Science, 159, 1968, p973

[3] Y. Murata, K. Nishikawa, Bull. Chem. Soc. Jpn., 51, 1978, p. 411

[4] Schwartz, L.H. And Cohen, J.B., 1987, Diffraction from materials, (Berlin: springer Verlag), p.46

[5] R. Caminti, V. Rossi Albertini, Int. Rev. Phys. Chem., 18 (2), 1999, p263-299

[6] K. Nishikawa, T. Iijima, Bull. Chem. Soc. Japan, 57, 1984, p.1750

[7] M. Tolan, X-ray Scattering from Soft-Matter Thin Films, Springer Tracts in Modern Physics, 148, 1999, Springer Heidelberg.

[8] L.G. Parratt, Surface Studies of Solids by Total Reflection of X-rays, Phys. Rev. 95, 1954, p359-369 .

[9] R. Felici, The Rigaku Journal, 12 (1), 1995, p11-17.

[10] E. Amaldi, R. Bizzarri, G. Pizzella, Fisica Generale, 2, (Zanichelli Editore), 1991.

[11] R. M. Richardson, S. J. Roser, Liquid Crystals, 2 (6), 1987, p797-814

[12] M. J. Grundy, R. M. Richardson, S. J. Roser, J. Penfold, R. C. Ward, Thin Solid Films, 159, 1988, p43-52.

[13] J. Penfold, R. K. Thomas, J. Phys.: Condens. Matter, 2, 1990, p1369.

[14] L. Ljaer, J. Als-Nielsen, L. A. Helm, P. Tippman, H. Mohwald, J. Phys. Chem., 93, 1989, p3200.

[15]J. Lekner, Theory of Reflection, Nijhoff Publ.: Dordrechet, The Netherlans, 1987.

[16] J. B. Hayter, H. A. Mook, J. appl. Cryst., 22, 1989, p35.

[17]W. E. Wallace, W. L. Wu, Appl. Phys. Lett.,67 (8), 1995, p1203.

[18] J. Penfold, R. K. Thomas, J. Phys.: Condens. Matter, 2, 1990, p1369.

[19] L. Névot, P. Croce, R. Phys. Appl., 15, 1980, p761-779.

[20] Di Jean Daillant,Alain Gibaud, X-ray and neutron reflectivity: principles and applications, ed. Springer, 2009

[21] S. J. Roser, R. Felici, A. Eaglesham, Langmuir, 10, 1994, p3853.

[22] E. Chason, M. Chason, J. Vac. Sci. Technol. A, 12(4), 1994, p1565.

[23] K. Orita, T. Morimura, T. Horiuchi, K. Matsushige, Synt. Met., 91, 1997, p155-158.

[24] J. Mio Bertolo, A. Bearzotti, A. Generosi, L. Palummo, V. Rossi Albertini, Sensors and Actuators B,111-112, 2005, p145-149.

[25] B. Paci, A. Generosi, V. Rossi Albertini, P. Perfetti, R. de Bettignies, M. Firon, J. Leroy, C. Sentein, Appl. Phys. Lett. 87, 2005, 194110

[26] James M. Gere, Barry J. Goodno, Mechanics of materials, Cengage Learning, 2009

[27] Rugar, Hansma. Atomic force microscopy, Physics Today. 1990. p23-30

[28] Alessandrini A, Facci P. Measurement Science and Technology.16(6), 2005, R65-R92.

[29] G Pompeo, M Girasole, G Longo, A Cricenti, D Bailo, F Ronci, A Maras, M Serracino, P F Moretti . 230(Pt 2):21, 2008, p8-23.

[30]M. Born, E. Wolf, Principles of Optics, Pergamon, Oxford, 1970

[31] V. Rossi Albertini, B. Paci, A. Generosi, J. Phys. D: Appl. Phys. 39, 2006, R461.

[32]S.K. Sinha, Z.B. Sirota, S. Garoff, H.B. Stanley, Phys. Rev. B 38, 1988, p2297.

[33] Paci, B. Generosi, A. , Albertini, V.R. , Perfetti, P. , De Bettignies, R. , Leroy, J. , Firon, M. , Sentein, C. Appl. Phys. Lett. 89,4 ,2006, 043507

[34] B. Paci, A. Generosi, V.R. Albertini, R. Generosi, P. Perfetti, R.D. Bettignies, and C. Sentein, Journal of Physical Chemistry C, 112, Jul. 2008, 9931-9936..

[35] J.M. Nunzi, C. R. Phys. 3, 2002, p523.

[36] Barbara S. Infrared Spectroscopy: Fundamentals and Applications. Analytical Techniques in the Science. 2004.

[37]K. Torabi, A. Karami, S. T. Balke, T. C. Schunk, Journal of Chromatography A, Volume 910, Issue 1, 23, 2001, p19-30

[38] Thermo Nicolet Corporation, Introduction to Fourier Transform Infrared Spectrometry, 2001

[39] Billmeyer, F W, textbook of polymer science, John Wiley & Sons Inc., New York 1984

[40] B. Paci, a Generosi, D. Bailo, V. Rossi Albertini, and R. de Bettignies, Chemical Physics Letters, vol. 494, no. 1-3, 2010 pp. 69-74, .

- Chapter III -

Experimental Apparatus and set-up

When characterizing a specimen or, as in the case of present work, thin films of organic materials, the synergic use of different techniques can enable one to gather information on different aspects of the sample, as for instance layer thickness and roughness, or bulk structural information like aggregations of active materials in crystallites of different sizes.

However the use of different characterization techniques can be seriously improved when they are used in a joint way, which allows to study the sample simultaneously with the different methods. Hence the data obtained are much more correlated than data obtained making single non-simultaneous measurements on similar samples, as seen in [1].

Using different techniques simultaneously, however, usually requires the integration of different scientific instrumentation in a single machine, which results to be a more complicated object than the assembly of the various different instruments. So in some cases it could be convenient to project and create non-commercial instruments which combine the different techniques and that, having more degrees of freedom respect to the single technique instruments, have a more complicated set-up. These are the instruments described in the following paragraphs.

3.1 Energy Dispersive Techniques and joint AFM

3.1.1 EDXR and EDXD

All measurements were performed by a non-commercial [1] Energy Dispersive machine joint with an AFM at the X-ray laboratory, I.S.M., C.N.R., Area della ricerca di Tor Vergata, Roma.

As this machine is basically made by a combination of a non-commercial ED machine and an AFM, we can describe separately the two apparatus.

From a geometrical point of view, the energy dispersive (ED) diffractometer/reflectometer (Fig. 1) is similar to a conventional angular dispersive (AD) one: the main differences concern the detection, the absence of monochromator [2] and the arms motion which in the case of ED is executed prior to measurement and can hence can be regarded as an instrumental parameter.
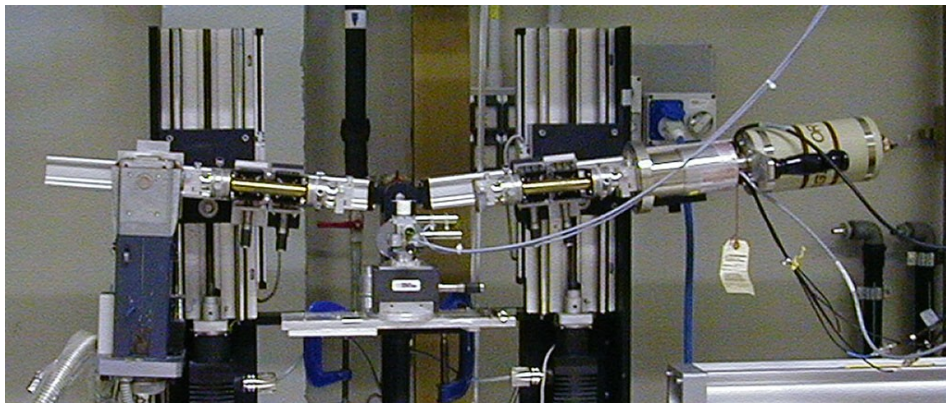
Figure 1: Photo of the energy dispersive X-ray Diffractometer/Reflectometer. The fundamental components are as follows: (1) X-ray source (W anode tube), (2) collimation slits, (3) sample holder, and (4) Ge single crystal energy-sensitive detector.

The instrument is mechanically very simple [3], with two arms contained in the vertical plane, pivoting around a single central axis. The arms are moved by two linear actuators driven by step motors and the tangent of the inclination angle is read by two linear encoders. Both the minimum step movement and the resolution of the encoders are $1\mu m$, leading to a minimum angle increment and reproducibility of $(4 \times 10^{-4})°$ [4].

An ordinary X-ray source [5] can be used as the radiation source, and in Fig. 2 the typical spectrum produced by a hot cathode W tube (Philips, model PW 2214/20) is shown: the tungsten L fluorescence lines and the continuous Bremmstrahlung hunch (white beam) can be recognized. While the fluorescence lines are produced by de-excitation of tungsten atoms when ionized by the

fast electrons beam impinging the target , the rest of the spectrum (white beam) is not a quantized phenomenon, as it is due to a deceleration of the same electrons in the electrostatic field present in the tungsten crystalline lattice, which produces the emission of radiation, according to classical electro dynamical laws [6].
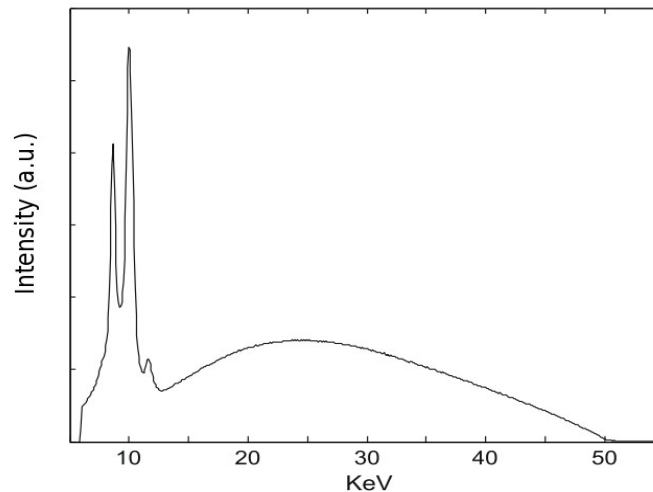

Figure 2: typical X-ray spectrum produced by produced by a hot cathode W tube (Philips, model PW 2214/20) is shown: the tungsten L fluorescence lines and the continuous Bremmstrahlung hunch (white beam) can be recognized.

To detect the X-rays spectrum an EG&G ultra-pure Ge solid-state detector (SSD) is used, cooled with X-cooler cryostat unit. The sensitive part of the detector is a semiconducting high purity germanium single crystal which is doped by another suitable element (lithium) in order to create a p-n junction inside it and make it behave like a diode that, in working conditions, is directly polarized by applying a high voltage at its sides. Many different mechanisms of excitation are activated in the Ge lattice when a photon of a certain energy penetrates the crystal and is absorbed. However the final result is the production of electron-hole pairs which are pushed in opposite directions under the effect of high external voltage. The integral over time of this pulse gives the total charge, that is the number of electron- hole pairs. Since this number is directly proportional to the energy of the absorbed photon, the intensity vs energy graph can be plot .

The detector is connected to an integrated spectroscopy amplifier-multichannel analyser system (92X Spectrum Master), which is basically a frequency histogram of the detected energies, quantized in channel. Depending on the calibration, every channel represents an energy interval., with an energy resolution of ca. 1.5% with a maximum counting rate of 10 Kcounts/s. By mean of home made software created for the laboratory system [8,9] the resulting spectrum can be visualized and also a preliminary analysis can be done, together with the option of running measurements programmatically [8].

The same ED instrument is used both for Reflectometry and Diffraction experiments, the main difference being the angle of incidence of the X-ray primary beam on the sample, which in the case of reflectometry is, depending also on the studied material, less than 0.3 ° degrees.

3.1.2 EDXR joint AFM

In the setup used for joint measurements, an AFM microscope and a X-ray Reflectometer are bundled together.

The AFM instrument is a home made machine which consists of a stainless-steel unit made of two separable cylindrical supports equipped with a passive vibration isolating system. The sample holder, placed in the lower unit, is mounted at the top of a piezoelectric scanner which allows a maximal scan size of $30 \times 30 \times 6$ μm. Additionally an x-y-z motor-controlled translator is used to move the sample and hence to select the sample area to be measured. The cantilever holder, together with the mirror deflection system and a four-sector position-sensitive photodiode used as deflection detector, are placed in the upper unit. Finally, an electronic feedback loop is used to integrate the optical signal and maintain a constant cantilever deflection during the data acquisition. Also, an additional active vibration isolation system was mounted as the basis of al microscope, the Accurion Halcyonics Nano 20, which enabled to carry out measurements getting rid of disturbing vibrations caused by machinery, air conditioning systems, vibrations caused by nearby traffic etc. The tip is ticked to the cantilever is an AFM tips from Veeco, made of antimony (n) doped Si; the cantilever has a resonance frequency f_0=257-308 kHz, and a spring constant k= 20-80 N/m. The electronic stage is then connected to an home made software which allows to perform experiment in different probing modes, as well as running measurements programmatically. This latter option enable us to synchronize the AFM acquisitions with the EDXR acquisition, thus obtaining coherent data from the two different techniques.

The AFM microscope, in this configuration, plays the role of the X-ray Reflectometer sample holder. It is therefore mounted on translators and rotating stages to allow a fine centering and alignment of the sample (see Fig. 3).
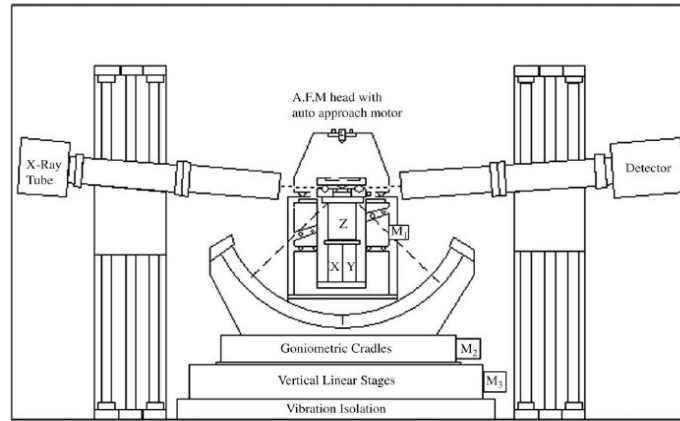
Figure 3: sketch of the EDXR joint AFM instrument. The AFM is used as a sample holder and can be moved and rotated to permit the sample centring and alignment (see movementation stages).

The sketch of Fig. 3 shows the Atomic Force Microscope specifically constructed taking into account the characteristics needed to perform simultaneous AFM and EDXR experiments. The microscope chamber is provided with two thin Al windows, expressly designed to allow the passage of both the incident and out coming X-ray beam with negligible absorption. Moreover, the microscope can be moved and rotated to permit the sample centring and alignment, as discussed in [7]. In addition, a chamber that can be placed in the AF microscope allows performing the two morphological characterizations under controlled atmosphere, thus preventing difficult procedures required to avoid the contact of the sample with air during its transport from the AFM to the XR instrument in a non-joint machine, as well as the sub sequent repositioning.

When performing a joint measurement, preliminary EDXR measures should be done to check that neither the presence of the microscope mechanical components, nor the motion of the AFM tip influence the original reflection pattern.

71

3.2 Fourier Transform Infrared Spectroscopy setup

A sketch representing the working of a FT-IR instrument from the source to the displayed data is shown in Fig. 4.
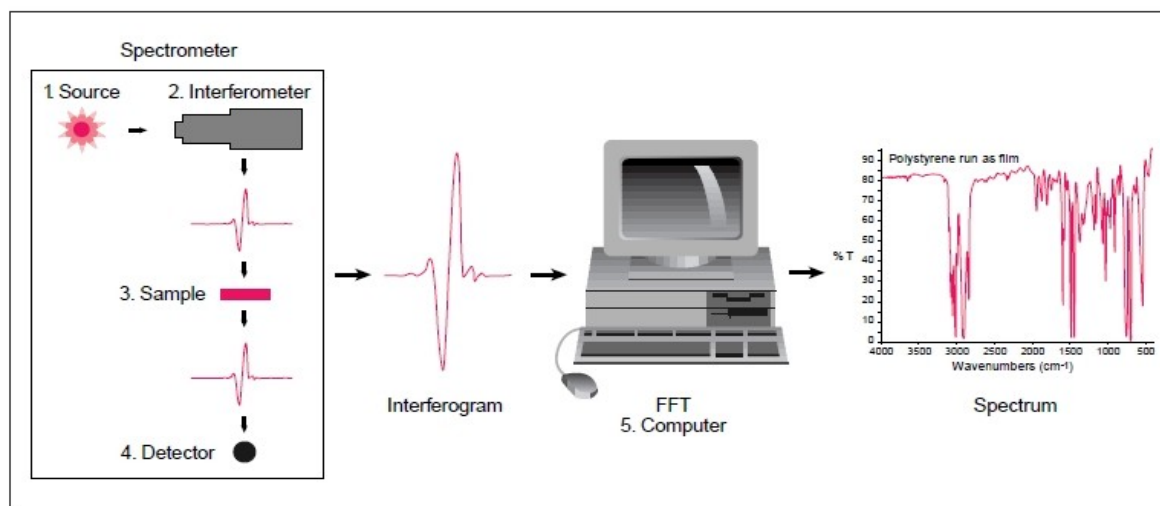

Figure 4: sketch representing the working of a FT-IR instrument from the source to the displayed data

The common instrumental process is as follows:

1. *The Source*: Infrared energy is emitted from a glowing black-body source. This beam passes through an aperture which controls the amount of energy presented to the sample (and, ultimately, to the detector).

2. *The Interferometer*: The beam enters the interferometer where the "spectral encoding" takes place. The resulting interferogram signal then exits the interferometer.

3. *The Sample*: The beam enters the sample compartment where it is transmitted through or reflected off of the surface of the sample, depending on the type of analysis being accomplished. This is where specific frequencies of energy, which are uniquely characteristic of the sample, are absorbed.

4. *The Detector*: The beam finally passes to the detector for final measurement. The detectors used are specially designed to measure the interferogram signal.

5. *The Computer*: The measured signal is digitized and sent to the computer where the Fourier transformation takes place. The final infrared spectrum is then presented to the user for interpretation and any further manipulation.

In the case of the present work, spectra of Fourier Transform Infrared Spectroscopy measurements were obtained by means of a Jasco FT/IR 470 Plus interferometer (Italy), equipped with an IRTRON IRT-30 microscope. Spectra were acquired in transmittance mode by executing 300

scans/point at 8 cm^{-1} resolution.

Bibliography

[1] 1. Paci B, Generosi a, Generosi R, Bailo D, Rossi Albertini V. Chemical Physics Letters. 483(1-3), 2009, p159-163.

[2] R. Caminiti, V. Rossi Albertini, Int. Rev. Phys. Chem. 18, 1999, p263

[3] R. Caminiti, C. Sadun, V. Rossi Albertini, F. Cilloco, R. Felici, Proceedings of the 25th National Congress of POhysical Chemistry, Cagliari, Italy 17-21 June, 1991.

[4]R. Felici, The Rigaku Journal, 12 (1), 1995, p11-17.

[5]K. Nishikawa, T. Iijima, Bull. chem. Soc. Japan, 57, 1984, p1750

[6]R.W. James, The optical principles of the Diffraction of X-rays, Woolbridge, Connecticut: Ox-Bow Press,1982

[7] V. Rossi Albertini, B. Paci, A. Generosi, J. Phys. D: Appl. Phys. 39, 2006, R461.

[8] D. Bailo, P. Escarate Monetta, V. Rossi Albertini, and A. Brunetti, International Journal of Online Engineering (iJOE), 5, 2009, p4-10.

[9] D. Bailo, nota interna ISM-CNR, 1-2010, 2010.

- Part Two -

Results and Discussion

In the previous part of the thesis the advantages of Solar Devices based on organic materials, and in particular bulk hetherojunction blends of P3HT:PCBM, have been emphasized to give reason for the great interest that these materials are generating both in the research field and in the worldwide market. In fact, despite the efficiencies which just nowadays begin theoretically to be slightly comparable to their inorganic counterpart [1], i.e. the silicon-based solar cells, the several advantages connected to the use of organic materials and in particular polymeric blends, as (i) the relatively cheap in production and purification, (ii) possibility of tailoring materials properties "on demand", (iii) possibility of use on flexible substrate, (iv) possibility to be shaped or tinted to suit architectural applications, (v) ease of processing and many other, make them competitive on the market [2].

Also, disadvantages of organic materials used as active layers in thin film organic solar cells have been pointed out. They can be roughly grouped in two categories: (i) problems connected to the materials chemical and molecular properties, like the band gap which in the case of polymer blends can be tailored in order to enhance solar radiation harvesting and thus efficiency, (ii) problems connected to stability of materials blends, which under the effect of environmental agents are subject to aging effects which influence the morphology of the blend and eventually lifetime and efficiency. It is worth observing that molecular and chemical properties as well can be influenced by the structure and morphology of the blend, in fact when organic semiconductors can reach an ordered solid crystalline structure, their absorption band becomes broadened with evident benefits with respect to the solar cell efficiency [3].

Still, in order to increase lifetime and efficiency, two key aspects for a wide spreading of devices based on organic materials blend, *control* and *monitoring* of *structural* and *morphological* characteristics, are fundamental issues. These characteristics can be subject to relevant modifications when exposed to environmental agents or other external agent, as already mentioned, thus affecting cell performances and lifetime.

In general OPV devices are composed by different organic layers, as discussed in previously (see Illustration 13 chapter 1, part I) .

The glass transparent substrate is the depositions substrate which needs to be transparent to let the solar radiation pass through and hit the active layers where the energy production occurs. ITO layer is the transparent electrode. PEDOT:PSS layer and P3HT:PCBM layer are thin films which are studied in the present work: the first is traditionally used as buffer layer to avoid conduction and ageing effects, the second is the active layer which deals with the conversion of solar energy into electric energy.

In this work a systematic study of the organic layers will be carried on, focusing on the morphological and structural parameters which influence efficiency and lifetime. The approach mainly relies on the in-situ joint EDXR/AFM studies. Preliminary investigations on a model sample, were needed in order to point out the major experimental aspects connected to the joint characterization using a non commercial apparatus, as discussed in the next section.

- Chapter I -

Optimization of Procedures and Techniques

The thesis work, aiming to address the fundamental problem in OPVs of the degradation of the organic layers structural/morphological characteristics, mainly relies on a joint use of EDXR and AFM techniques, as discussed.

A fist part of the experimental work is, therefore, devoted to the validation of the novel approach and to the optimization of the set-up here applied for the first time to organic films for OPV applications. This set-up, far from being straightforward, needs indeed an accurate calibration in order to obtain affordable and reproducible results.

1.1 Preliminary studies validating the Joint EDXR / AFM technique approach

The great advantages presented by EDXR / AFM technique, which is a unique tool for the study of thin film organic layers of solar devices, become evident when one needs to investigate the surface and bulk properties of organic layers, whose behaviour at the interface with the substrate is of the uttermost importance for the device performances.

To harvest these information together in real-time, it follows that it is necessary to perform joint AFM and EDXR, to be sure that the two measurements are executed on the system in the same state. A further advantage of the technique setup shown in the first part of this work, is that a chamber that can be placed in the AF microscope allows performing the two morphological characterizations under controlled atmosphere and thus, if necessary, avoids difficult procedures required to prevent the contact of the sample with air during its transport from the AFM to the EDXR instrument.

Prior to the use of this techniques on the samples of interest, i.e. organic layers for organic solar cells, a validation has been necessary in order to verify the applicability of the technique and prove the accuracy of the results.

As a test sample, a Co-porphyrazine metallo-organic film was chosen, being particularly suited for the purpose of this work because of some of its characteristics: (i) it belongs to a family of metallo-organic sensing films whose morphological behaviour in static or dynamic environmental conditions is well known [4-5] (ii) it is a single layered films, hence multiple effects due to superposition of signal coming from different layers are avoided, (iii) it shows an optimal film-substrate optical contrast [5], (iv) it is stable in ambient conditions (air and light). It was grown by vacuum sublimation on a Si (001) wafer. The deposition of these molecules is a well established and reliable procedure, typically resulting in highly homogeneous and smooth films. The film surface is expected to be finely textured with small structures of a few Ångstroms of diameter. The "landscape" is, therefore, varied and rich in details but regular, so that no discrepancy between the AFM and the EDXR results is expected, allowing extracting the interface characteristics with a high level of confidence.

First of all, in order to verify that the presence of the AF microscope produces no relevant effects on the X-ray reflection, a sequence of EDXR patterns on a reference sample was collected in various experimental conditions.

All the EDXR measurements we're going to describe were carried on with a beam energy of 55KeV, at a scattering angles of 0.150° degrees, with a square collimation slides shape and slides apertures of 50µm*50µm. The AFM measurements were performed in non-contact mode. The first measurement was executed on the test-sample using a standard sample holder (pattern A of fig. 1). The subsequent measurements, instead, were accomplished after replacing the sample holder with the AF microscope. In the latter arrangement, referred to as B, several patterns were collected (fig. 1) in order to observe, step by step, the possible interference of the single mechanical parts of the AF microscope with the primary or the reflected X-ray beam. In particular, B1 represents the pattern acquired keeping the microscope head open and B2 corresponds to that obtained after closing the microscope head. Finally, patterns B3 and B4 correspond to two EDXR measurements performed while collecting AFM images (reported in Fig. 2), i.e. the microscope head closed and the tip upon working. As it can be noticed by observing Fig. 1, no visible change in the pattern shape is observed. This confirms that neither the replacement of the sample holder with the AF microscope, nor the presence of the microscope mechanical components, nor the motion of the AFM tip to explore different zones of the surface, influence the original reflection pattern A.
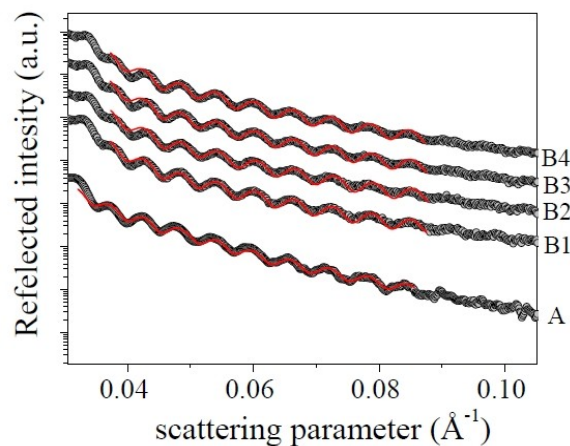

Figure 1: ED Reflectivity profiles collected upon the test sample using a traditional sample holder (A); positioning the sample into the AFM keeping the microscope head opened (B1), closed (B2), and during the simultaneous EDXR/AFM data collection (B3 and B4).

The two AFM images in Fig. 2 appear very similar, testifying that the slight vibrations of the X-ray apparatus do not compromise the stability and the accuracy of the AFM system and that the sample surface is homogeneous as expected. Two equivalent profiles were extracted from both images along the arrows drawn in Fig. 2, which confirms what previously stated on qualitative bases.

As visible in the 3D maps, an ordered granular texture corresponding to the characteristic porphyrazine morphology was observed, the average grain size being 0.5nm in vertical and 50nm as lateral dimension.
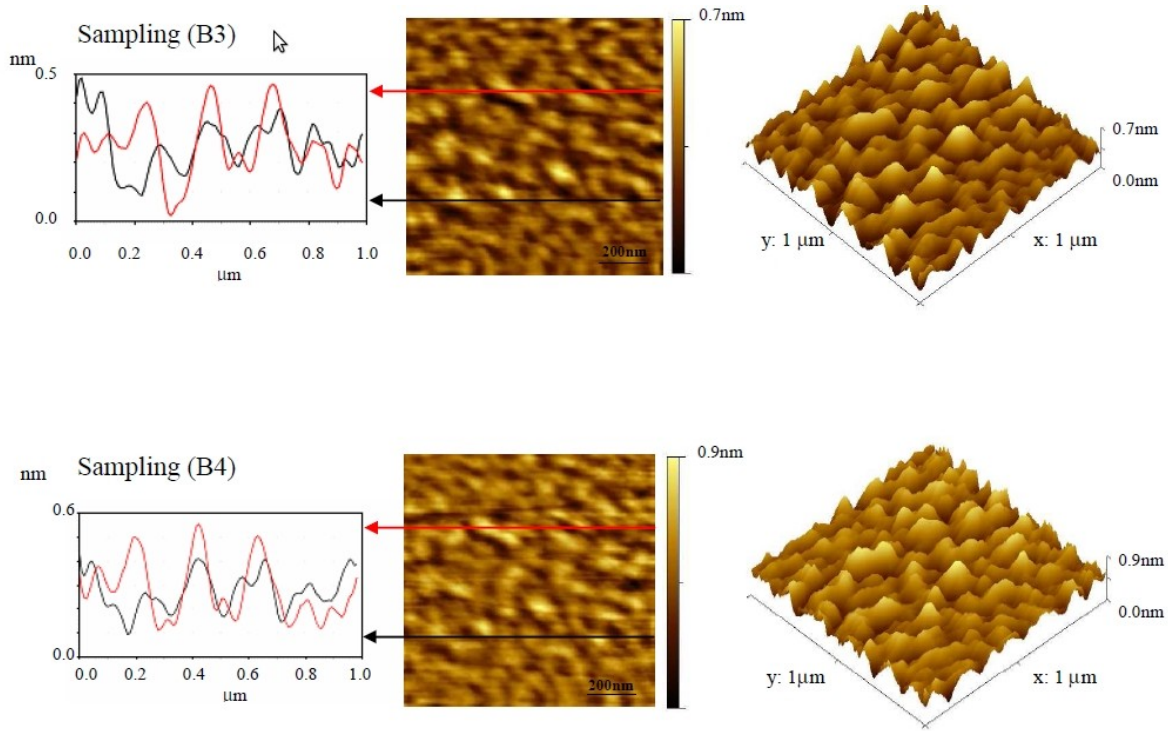
Figure 2: AFM images (1mm*1mm) and their 3D projections (right side) collected upon a Co-porphirazine film simultaneously with the EDXR patterns. The upper and the lower image correspond to the B3 and B4 spectra respectively.

In table II quantitative results obtained through a Parratt fit of the reflectivity profiles and from statistical procedures (standard deviation from the average height) applied on AFM images, are reported: sample thickness, calculated for all the samples, and sample roughness deduced both from AFM (only samples B3 and B4) and EDXR experiments, show that the values of the considered physical quantities remain constant within the statistical error for all the samples. This confirm the above-mentioned assumptions, that is to say the independence of measurement results from the possible interaction of the primary beam with microscope tip or mechanical parts, and independence of measurement from slight external vibrations.

Sample	Si(001)	A	B1	B2	B3	B4
σ_{AFM} (Å)	0.7 (0.7)				1.7(0.7)	1.9(0.7)
σ_{EDXR} (Å)	1.0 (0.4)	2.8 (0.5)	2.7 (0.5)	2.4 (0.5)	2.0 (0.5)	2.2 (0.5)
d_{EDXR} (Å)		1010.0 (0.5)	1011.0 (0.5)	1010.5 (0.5)	1011.7 (0.5)	1010.2 (0.5)

Table II. Roughness values deduced from AFM images and EDXR patterns are shown for all samples considered,

together with the thickness values as obtained by the accurate fitting procedure of each reflectivity spectrum.

However looking at the roughness values σ calculated for samples B3 and B4 both in AFM and EDXR, some discrepancies can be noticed: the fact that the σ_{AFM} is in the two cases lower than the σ_{EDXR} give us the occasion to deeply discuss and investigate the relation between the two roughness calculated both in EDXR and AFM. As stated in the first part of this work, they have two main differences: the first is that the σ calculated from AFM images, is calculated in the direct space, while in EDXR it is deduced from the reciprocal space. The second difference is that while the σ_{AFM} is a measure of surface roughness, the σ_{EDXR} incorporates both surface and interface roughness terms, which even if theoretically distinct, under the practical point of view are tightly entangled: while their joint value can be accurately determined, their individual values are rather uncertain. In fact the overall film roughness represents the variance of two joint distributions (the distributions of the film surface and interface local heights). When they can be considered independent [6], as in the case of film not extremely thin or not deposited layer by layer, they fulfil the relation

$$\sigma^2_{film\ overall} = \sigma^2_{film\ surface} + \sigma^2_{film\ interface} \quad (1)$$

where $\sigma^2_{film\ overall}$ and $\sigma^2_{film\ surface}$ correspond in our case to $\sigma^2_{film\ EDXR}$ and $\sigma^2_{film\ AFM}$, respectively

In this perspective, the two joint AFM/EDXR experiments B3 and B4 were used to show the possibility offered by the proposed set-up of gaining reliable information on the surface of a bulk sample and most of all on the *interface* between a film and its substrate. Indeed an additional AFM/EDXR measurements was performed on the Si (001) wafer used as substrate. Its reflectivity profile is plotted in Fig. 3 together with its Parratt fit, while the 3D representation of the (1μm*1μm) AFM image is shown in the inset of the same figure. The roughness values deduced from the EDXR and the AFM measurements are reported in table II. They are coincident within the error, and correspond to an atomically flat surface ($\sigma_{Si\ surface} \approx 1.0$ Å), thus confirming that in the EDXR roughness value previously deduced the only term having a significant contribution is surface roughness. Furthermore, it is worth noticing that, from the AFM image, no structure can be detected, the surface being so flat that the apparent topography is actually due to electronic noise only.

Applying the eq. 1 to roughness values of sample B3 and B4, it turns out that $\sigma_{film\ interface}$ for the film is about 1.0 Å, which equals the Si wafer roughness value $\sigma_{Si\ surface}$ just shown. This is the expected result, since soft metallo-organic films deposited on hard material substrates do not disturb the original morphology of the substrates, adhering to the surface and following its morphology.
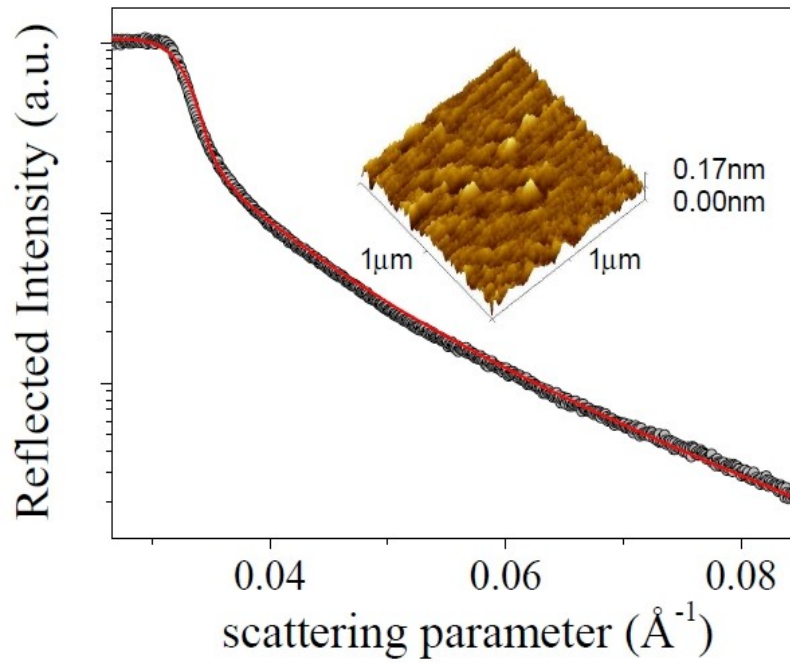
82

Figure 3: ED Reflectivity profile (dots) and Parratt fit (continuous line) of a Si (100) surface plotted as a function of the scattering parameter. In the inset a 3D projection of an AFM topographic image collected upon the same surface is shown.

1.2 Conclusions

In summary, the results of this first joint EDXR/AFM study [7],enabled to:

•validate the joint EDXR/AFM technique set-up, showing that measurements carried on a test sample (film deposited on a substrate) are feasible, they also give the expected results and most of all are not affected by instrumental errors and do not present artefacts.

•validate the joint EDXR/AFM technique set-up for the use with multilayered samples or devices

•validate the joint EDXR/AFM technique as a unique tool for a quantitative estimation of interface roughness at buried interfaces.

Bibliography

[1] J.D. Kotlarski and P.W.M. Blom, Applied Physics Letters, 98, 2011, p. 053301.

[2] T.L. Benanti and D. Venkataraman, Photosynthesis research, 87, 2006, p73-81.

[3] G. Chidichimo and L. Filippelli, International Journal of Photoenergy, 2010, 2010, p1-12.

[4] A. Generosi, P. Paci, V. Rossi-Albertini, P. Perfetti, A. M. Pa- oletti, G. Pennesi, G. Rossi, and R. Caminiti., Appl. Phys. Lett. 87, 2005, 181904.

[5] A. Generosi, B. Paci, V.R. Albertini, P. Perfetti, A.M. Paoletti, G. Pennesi, G. Rossi and R. Caminiti, Appl. Phys. Lett. 88, 2006, 104106.

[6] A. Papulis, Probability and Statistics (Prentice-Hall Ed., U.S.A. 1990).

[7] B. Paci, a Generosi, R. Generosi, D. Bailo, and V. Rossi Albertini, Chemical Physics Letters, 483, no. 1-3, 2009, p159-163

- Chapter II-

PEDOT:PSS buffer layer

Because of its processability and good mechanical properties, the optical transparent polymer poly(3,4- ethylenedioxythiophene):poly(styrenesulfonate) (PEDOT:PSS) results to be a promising candidate for a wide range of applications in OSC.

However it is not free from disadvantages: as already cited, ambient moisture can have a negative influence on the conducting properties of the blend [1] and the elevated temperatures reached inside the cells during illumination may cause interface degradation effects, as interfacial diffusion [2,3], as well as structural and morphological changes that may compromise the correct cell working [4].

Hence, a deeper investigation both in ambient moisture and at the high temperatures at which OPV devices operate, addressing problems related to the preservation of the PEDOT:PSS film chemical-physical properties, is still needed.

In the present work PEDOT:PSS blends were studied by means of the time-resolved EDXR/AFM joint technique previously described. The samples were investigated in-situ both under controlled moisture conditions and during thermal treatments (45°C and 70°C). This temperature range allowed to simulate the heating conditions reached by the components of the cell upon device working. AFM measurements provided information on the surface morphology, while EDXR measurements allowed to monitor the changes experienced by the blend morphological parameters (thicknesses and joint interface/surface roughness). The cross monitoring provided by EDXR/AFM technique supplied direct information on the PEDOT:PPS layer / ITO substrate interface, very sensitive to the possible reaction or diffusion processes involving the two materials.

2.1 System and materials

The studied sample is represented in Fig 1. Being a multilayer composed by a substrate of glass, a layer of ITO, the transparent electrode, and finally a PEDOT:PSS layer. The indium tin oxide substrate was cleaned in an ultrasonic bath with acetone and isopropanol, then rinsed in deionized water, dried in an oven and, finally, treated with UV-ozone. The substrate was then spin-coated with PEDOT:PSS from Baytron PH at 1500 rpm, and oven dried at 100 °C for 60 min. The samples were fabricated by the research group Composants Solaires CEA INES-RDI, France.
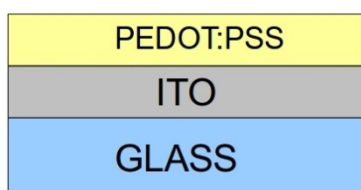
Figure 1: Sketch of the PEDOT:PSS sample

Measurements were carried by means of X-ray reflectometry, Atomic Force Microscopy, and Fourier Transform Infrared Spectroscopy. EDXR and AFM experiments were carried out jointly by means of the homemade EDXR/AFM joint instrument. All the EDXR measurements were carried on with a beam energy of 55keV, at scattering angles of 0.120° degrees, with square collimation slides shape and slides apertures of 50μm*50μm. The AFM measurements were performed in non-contact mode. FTIR measurements were performed by means of a Jasco FT/IR 470 Plus interferometer (Italy) equipped with an IRTRON IRT-30 microscope. Each spectrum was acquired in the transmittance mode by executing 300 scans at 8cm^{-1} resolution.

2.2 Results and discussion

In order to have a wider view of morphological and structural phenomena occurring in the PEDOT:PSS layer, experiments were performed in different phases which correspond to the different working conditions OPV cell may be submitted to:

1. preliminary measurements, i.e. ex-situ EDXR/AFM

2. in-situ EDXR/AFM up-on isothermal heating

3. in-situ EDXR/AFM up-on exposure to saturated moisture atmosphere

As last step, a FTIR characterization was performed in order to gain deeper information about processes occurring at ITO/PEDOT:PSS interface.

2.2.1 Ex-situ EDXR/AFM

Preliminary EDXR/AFM ex-situ experiments were performed on both the glass/ITO substrate and on the glass/ITO/PEDOT:PSS system. Fig. 2 shows a comparison between the EDXR patterns and the AFM images collected on the
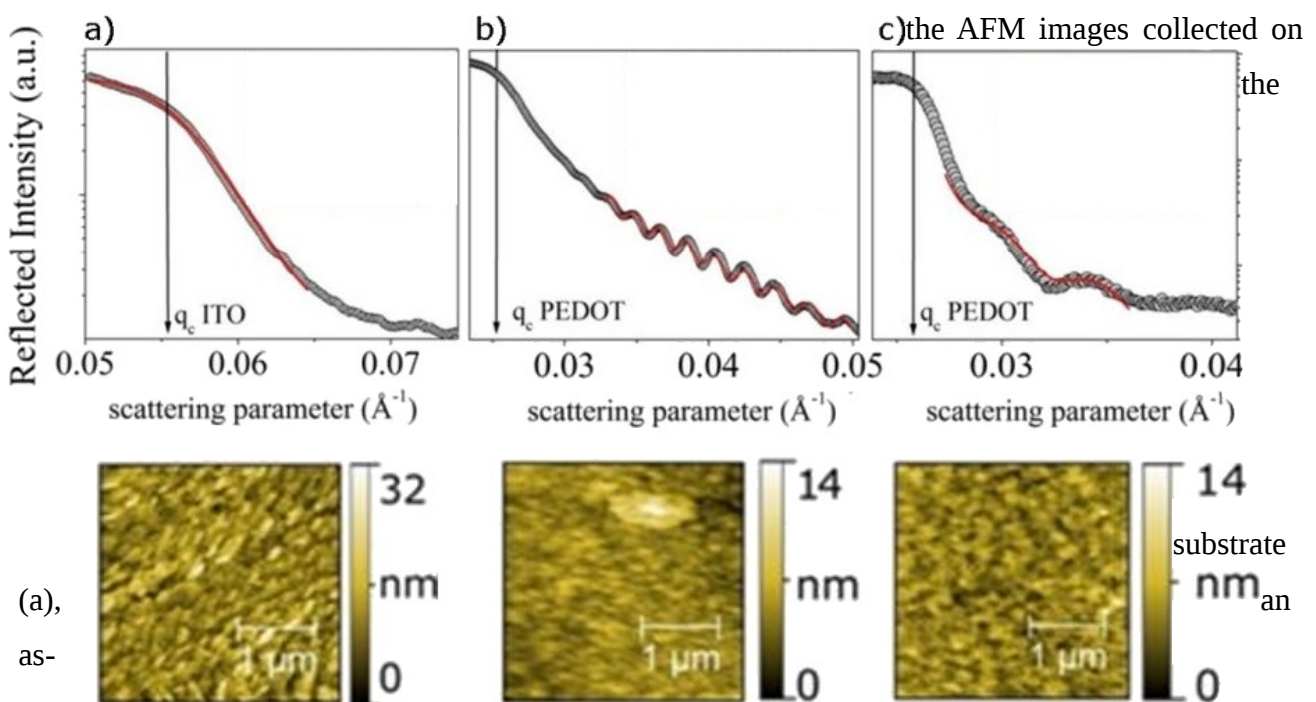
substrate (a), an as-deposited PEDOT:PSS film (b) and an film stored in ambient conditions (c).

Figure 2: EDXR patterns and corresponding AFM images (lower part) collected on the substrate (a), the as-deposited PEDOT:PSS film (b) and the film stored in ambient moisture conditions (c). Red lines: fit of the experimental spectra.

A fit procedure was performed on EDXR reflectivity patterns to calculate sample surface and

interface roughness, and thickness, using the Parratt model. Also, the surface roughness of AFM images was calculated as the standard deviation from the average height. The roughness values obtained by the AFM and the EDXR data reported in Fig. 2 are summarized in table I.

Sample	σ_{AFM}	σ_{EDXR}
ITO	4.0 nm	3.0 nm
(ITO/PEDOT:PSS)	1.5 nm	0.5 nm
(ITO/PEDOT:PSS) 100%RH	1.2 nm	1.5 nm

Table I: surface roughness (obtained by AFM) and joint surface/interface roughness (obtained by EDXR) of ITO, ITO/PEDOT:PSS AND ITO/PEDOT upon exposure to saturated moisture atmosphere .

As already discussed, the absolute roughness value retrieved by AFM measurements, σ_{AFM} , is not directly comparable to the one given by EDXR, σ_{EDXR}. However, what is relevant to the present study is that the roughness modifications follow the same trend regardless of the technique used. That is to say the deposition of a PEDOT:PSS layer on top of the ITO substrate actually allows a roughness reduction. Reversely, after storage in ambient conditions a raise in roughness was detected by EDXR. This latter process may, in principle, be associated to both surface or interface modifications. Nevertheless, here, additional information on the film surface topography gained by AFM, give evidence that the surface roughness is comparable (table I). This morphological characterization performed applying both AFM (sensible to surface modifications) and EDXR (sensible to both surface and interface roughness) technique, allowed the detection of an aging process limited to the film buried interface, in contact with ITO. Such degradation may be imputable to the production of an acid aqueous-solution environment in contact with the ITO substrate, leading to decomposition of ITO and consequent diffusion of Indium species to into the PEDOT:PSS layer, in accordance with literature [3,5]. Indeed, absorption of water molecules from ambient moisture is expected, owing to the highly hygroscopic nature of PSS. In the next sections we will elaborate on such premise, investigating the effect of water uptake/release on the chemical-physical characteristics of the blend, which in turn influence in its conducting properties and application in OPV systems.

2.2.2 In-situ EDXR/AFM up-on isothermal heating

In order to reproduce the cell working temperature, the sample previously studied after storage in

air at ambient temperature was measured in-situ during temperature ramps. The results of the time-resolved EDXR measurements are reported in Fig. 3. The reflectivity profiles are shifted in height for clarity. The minima in the EDXR patterns show a progressive shift toward higher q values as a function of time (see, for example, the line connecting the second oscillation minima). This indicates a modification in the film thickness, connected to the oscillation period Δq by the approximate relation $d \approx 2\pi/\Delta q$.
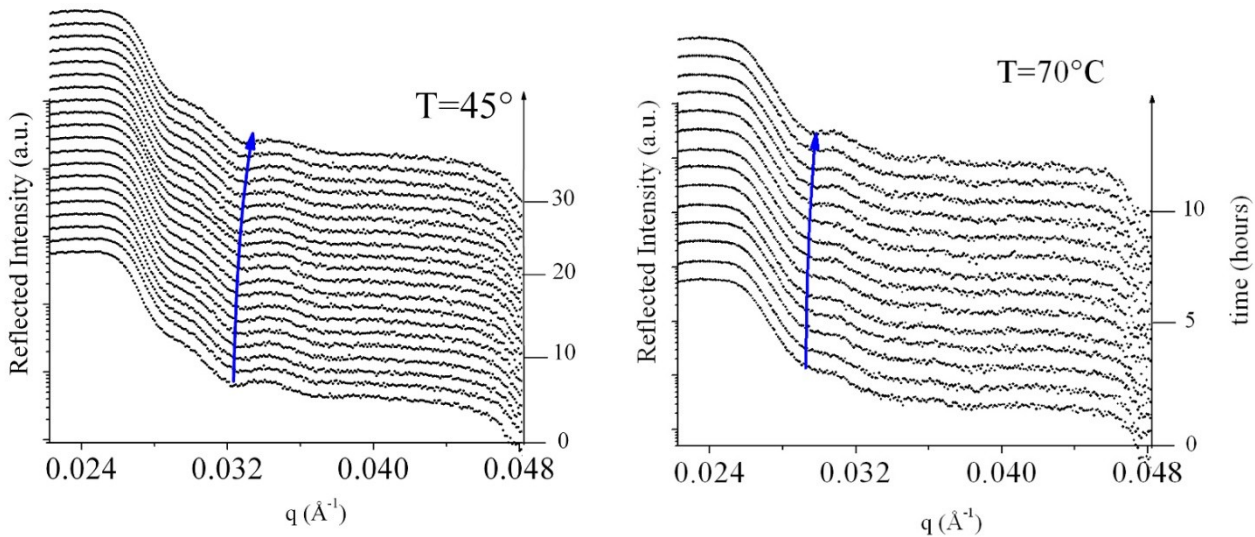
Figure 3: results of the time-resolved EDXR studies of the PEDOT:PSS film: the reflectivity profiles, shifted in height for clarity, were collected in-situ during temperature ramps.

The time dependence of the PEDOT:PSS layer thickness d and roughness σ, obtained by fitting the EDXR data using the Parratt model, is reported in Fig. 4. The film thickness decreases for both temperature stages, while the overall roughness remains constant (for both temperature stages).

The amplitudes (and time constants) of the overall d variations are: $\Delta d_{45°C} = (4.0\text{Å} \pm 0.5)$ Å (at $\tau = 8$ h) and $\Delta d_{70°C} = (10.0 \text{ Å} \pm 0.5)$ Å (at $\tau = 4$ h), respectively, where t is the characteristic time of the sigmoidal fit of $\Delta d/d_0$ plots reported in fig 4. The overall thickness decrease is about 2%.
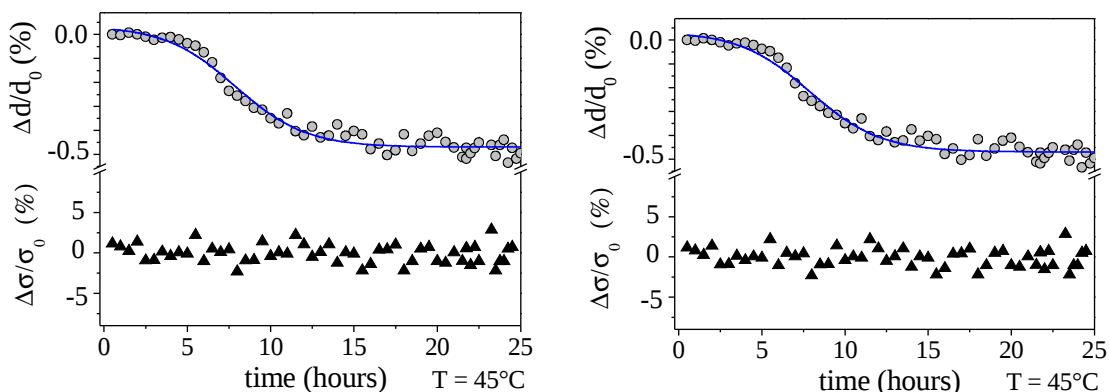

Figure 4: Time dependence of the PEDOT:PSS layer thickness d and roughness σ, obtained by fitting the EDXR data in

90

fig.3.

The surface topography of the sample was studied in situ by AFM: images were collected during sample heating, during EDXR experiments. Importantly, using such time-resolved AFM approach and monitoring a fixed portion of the film surface, minimal modifications of the film surface and changes in the surface roughness in the order of magnitude about 1 Å can be sampled [3,6].
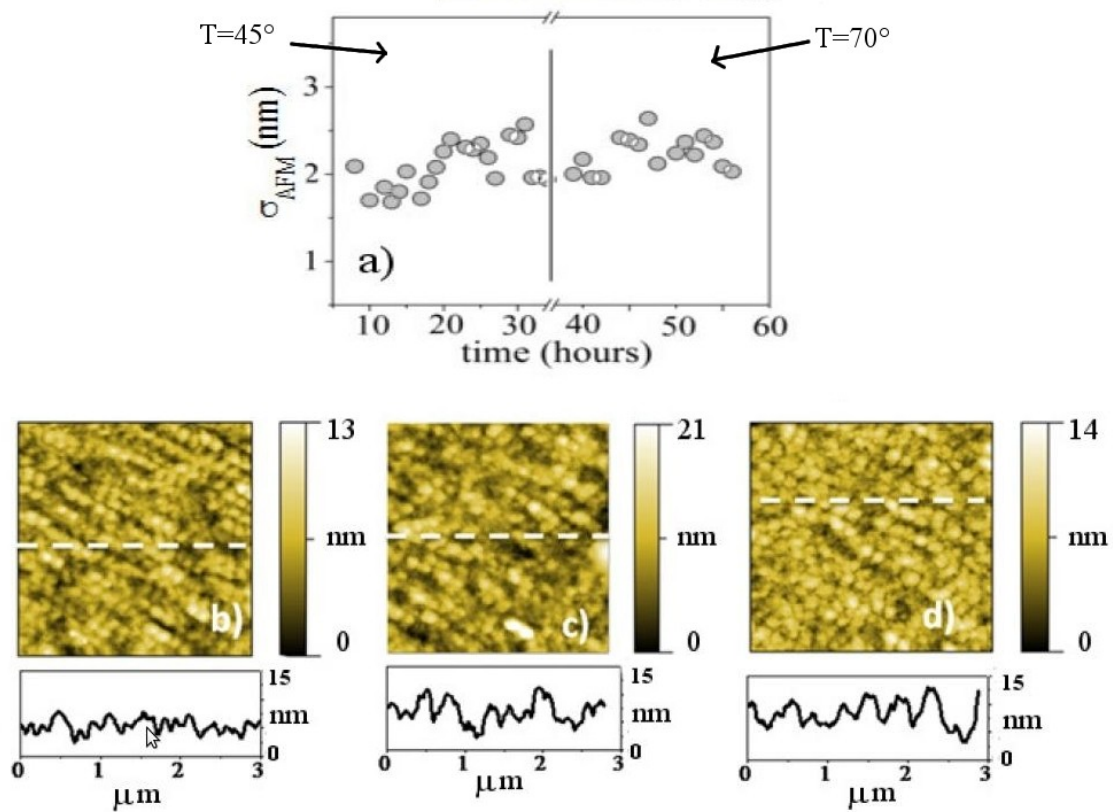

Figure 5: Results of the in-situ study of the PEDOT:PSS film surface morphology during sample heating: σ_{AFM} vs time curve (a), last image at RT(b), at 45 °C (c) and at 70°C (d).

The result of this sequential collection of images is that the surface morphology is not subject to modifications, in accordance whit EDXR analysis. This is evident, looking at the σ_{AFM} vs time curve shown in Fig. 5a and at the comparison of the last image at RT, at 45 °C and at 70°C, reported in Fig. 5 b, c and d, respectively.

Therefore, such in-situ study evidences that, during sample heating, release of water molecules absorbed due to long storage in ambient moisture, produces bulk morphological modifications (shrinking of the layer) while no surface deterioration occurs.

2.2.3 In-situ EDXR/AFM up-on exposure to saturated moisture atmosphere

In the third and final step of the in-situ study, the PEDOT:PSS layer was monitored during exposure

91

to saturated humidity conditions (100%RH) by joint EDXR/AFM experiments. In Fig. 6, a selection of AFM images, representative of the film surface at the beginning of the exposure to 100%RH atmosphere (Fig. 6a) and of the film surface after 3 hours and after 8 hours (fig. 6b–c), respectively, is reported. All images were then processed and their mean roughness was calculated and plotted as a function of time in fig. 6d. In this case, in the first 30 hours the surface roughness decreases.
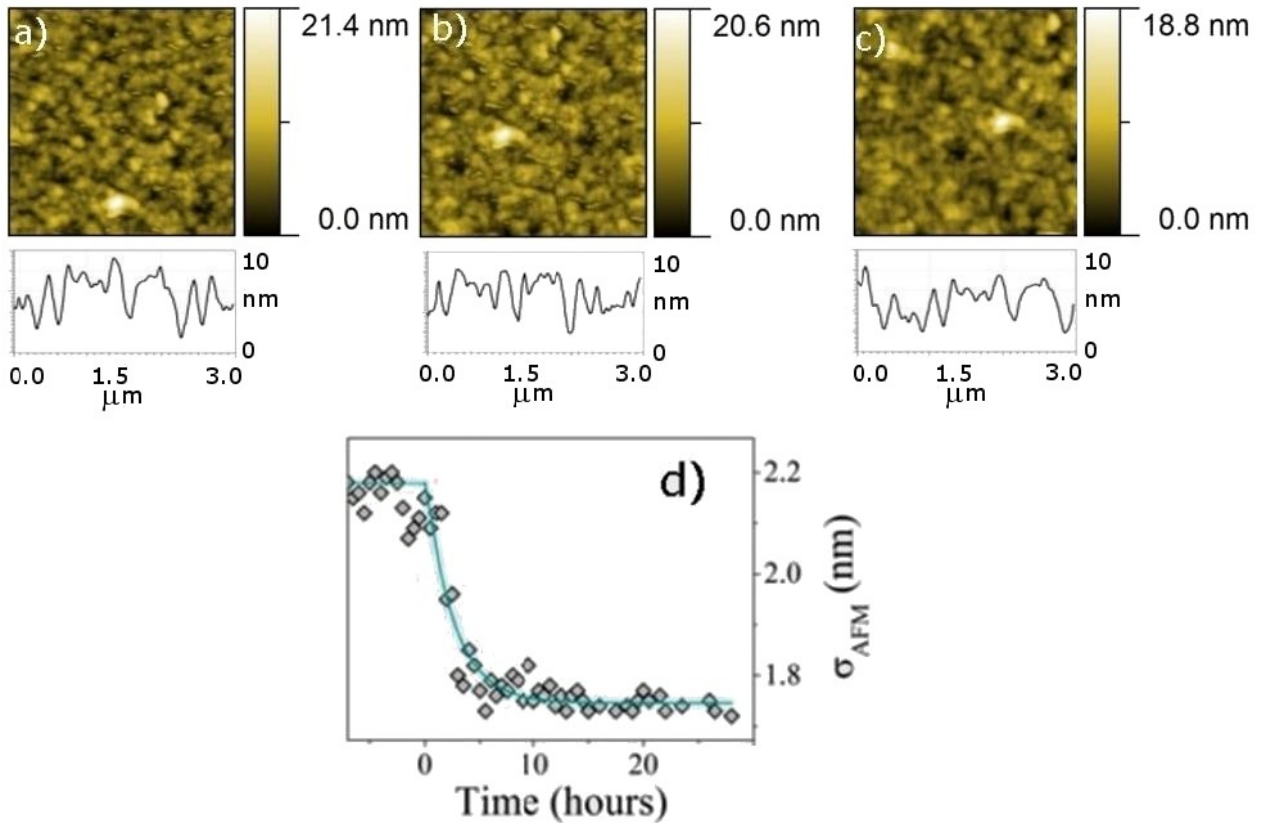

Figure 6:Results of the in-situ study of the PEDOT:PSS film surface morphology during to saturated humidity (100%RH) conditions: AFM images at the beginning (a), after 3 hours (b), and after 8 h (c), and σ_{AFM} vs time curve (d).

A lower roughness is consistent with a growing number of H_2O molecules populating the film surface and determining a higher uniformity. Complementary information, reported in Fig. 7, is supplied by EDXR: after a first induction time in which the film thickness remains unchanged, the water molecules, crowding on the film surface as suggested by AFM, start diffusing inside the film so that a rise in thickness is detected. Such increase is minimal (0.4%) and compatible with a diffusion involving only the superficial layer of the film.
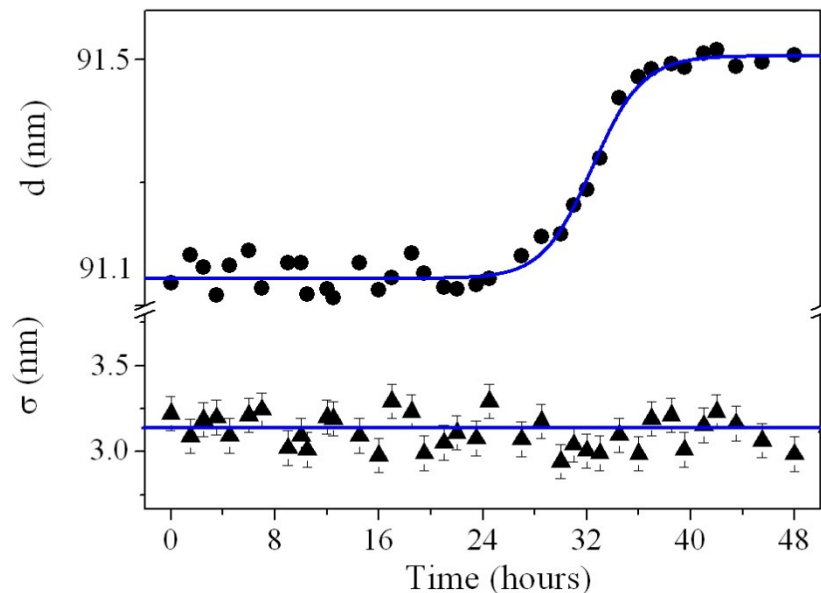
Figure 7: Time dependence of the PEDOT:PSS layer thickness d and roughness σ, during exposure to saturated humidity conditions (100%RH).

This fact, in turn, provides some hint that the PSS component may have loss its hygroscopic properties, as we will see in the next section. It is worth noticing that detecting a surface roughening as small as 0.4-0.5 nm, close to the AFM detection limit, was possible thanks to the fact that the experiment was performed in-situ, so that we were able to follow in real time the kinetics of the surface modification.

This is not the case of the EDXR technique, which, in the same time scale, was not able to perceive any modification in σ. Indeed, as discussed above, the joint surface and interface roughness, to which EDXR is sensitive, is dominated by the rough interface, making it difficult to distinguish a small surface modification.

2.2.4 FTIR characterization

Further FTIR results provided the information needed to clarify the chemical process at the basis of the morphological behaviour observed by the previous studies. FTIR data are reported in Fig. 8 and the vibrational modes are labelled in Table II. The samples were measured after each described step: storage in atmosphere; heating (at 45 °C and 70 °C) and final exposure to saturated moisture atmosphere. In the FTIR spectra the bands showing the most remarkable modifications are the following:

•A strong reduction in the broad band in the 3400-3640 cm^{-1} range, well visible for the sample

93

exposed to moisture, occurs as a consequence of heating. This feature indicates a loss of free water molecules, as expected.

•A remarkable drop of the modes related to the PSS solfonic groups, conferring the hygroscopic character to the polymer, at 3200 cm^{-1}, at 1522 cm^{-1}, at 1305 cm^{-1} and at 1140 cm^{-1} is revealed, as a consequence of heating. This fact suggests that sulphur ions SO$^{-}_3$ were produced, in accordance with what reported in literature for LEDs having PEDOT:PSS intermediate layer [7].

On the contrary, no relevant modification of the FTIR spectrum was detected repeating the experiment after that the sample was kept in moisture saturated atmosphere (during in-situ joint EDXR/AFM experiments). This fact validates the previous hypothesis that the hygroscopic properties were lost.
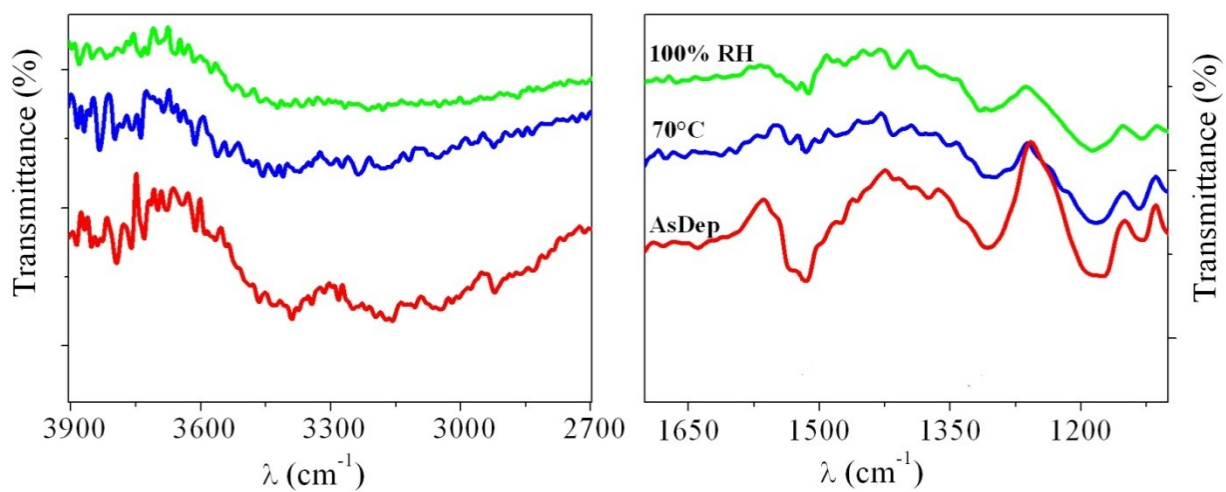

Figure 8: FTIR data after the each step of the in-situ study: storage in ambient atmosphere; heating (at 45 °C + 70 °C) and final exposure to saturated moisture atmosphere.

Wavelength (cm-1)	PSS	H2O
3400-3640		-OH
3200	-OH	
3100	C=C aromatic	
2918	C-H alkyl	
1522	C=C alkyl	
1305	S=O	

Table II. PEDOT:PSS vibrational modes labelled in fig. 8.

In summary, the overall results of FTIR studies suggest that, due to hygroscopic properties of the PSS component, the incorporation of ambient moisture in the pristine blends affects the film bulk and interface properties. During thermal treatments, the water molecules are released, leading to

94

morphological rearrangement of the blend, as observed by X-ray experiments. This picture is supported by FTIR data, also detecting chemical modifications of the PSS component. Subsequently, in saturated humidity conditions, only a minimal increase in the thickness of the film is observed, consistent whit a process involving only the superficial layer, as confirmed by FTIR data, suggesting that PSS may have loss its hygroscopic properties.

2.3 Conclusions

In conclusion, the morphological and chemical properties of PEDOT:PSS, used as polymeric buffer layer in photovoltaic devices, were investigated by means of the unconventional joint use of time resolved EDXR/AFM measurements, also integrated by FTIR complementary studies [8].

The results suggested that when storing the samples in non-controlled ambient conditions, the buried interface results to be corrupted. Such degradation is imputable to water molecules absorption, due to ambient moisture, and consequent production of an acid aqueous-solution environment in contact with the ITO anode (considered the PPS hygroscopic nature).

The effect of water uptake/release on the chemical-physical characteristics of the blend is studied in-situ by further investigations performed simulating the range of temperatures in which OPV cells work. In this case, a modification of the film morphological parameters over time is detected (progressive shrinking of the film) during water desorption.

A subsequent joint EDXR/AFM in-situ experiment under humidity saturated atmosphere evidenced a swelling process, followed in real time, compatible with diffusion of water molecules limited to the superficial layer of the blend. The bulk morphological modifications, induced by water uptake/release, resulted to be irreversible, evidencing denaturation of the PSS component with loss of hygroscopic properties of the film. This latter hypothesis is well confirmed by FTIR experiments, performed at each stage of the various treatments.

These results identify possible sources of degradation of the PEDOT:PSS blend, that may compromise the role as hole transport layer in organic devices. The overall study provides a new step toward the identification of those aging effects limiting the present applications of organic devices, suggesting the need for more stable polymer buffer layer materials and effective encapsulation method.

Bibliography

[1] K. Kawano, R. Pacios, D. Poplavskyy, J. Nelson, D. D. C. Bradley, J. R. Solar Energy Materials and Solar Cells, 90 (2006) 3520-3530.

[2] S. Schuller, P. Schilinsky, J. Hauch, C. J. Brabec, s, Appl. Phys.A: Mater. Sci.Process. 79, 2004, p37-40.

[3] B. Paci, A. Generosi, D. Bailo, V. Rossi Albertini, R. de Bettignies, Chem Phys. Lett. 494 (1-3) 2010, p69-74.

[4] E. Vitoratos, S. Sakkopoulos, E. Dalas, N. Paliatsas, D. Karageorgopoulos, F. Petraki, S. Kennou, and S. Choulis, Organic Electronics, 10, 2009, p61-66.

[5] J. Guo, N. Koch, S. L. Bernasek, J. Schwartz, Chem. Phys. Lett. 426, 2006, p370–373.

[6]B. Paci, A. Generosi, V. Rossi Albertini, P. Perfetti, R. de Bettignies,C., Chem. Phys. Lett. 483 2009, p159–163

[7] A. W. Denier van der Gon, J. Birgerson, M. Fahlman, W. R. Salaneck, Org. Electron. 3, 2001, p111-118.

[8] D. Bailo, A. Generosi, V. Rossi Albertini, R Caminiti, R. De Bettignies and B. Paci, Submitted to Synthetic Metals.

- Chapter III -

P3HT:PCBM Bulk Heterojunctions

As already extensively discussed in the first part of this work, the P3HT:PCBM bulk heterojunction blend is at the moment on of the most promising and used materials for applications in OPV.

Still, in order to fully understand the origin of the aging mechanisms, a deeper inspection of the nano-metric processes involved is still required.

In particular, heating due to illumination may result in thermal induced modifications of the active layer and consequent phase separations, PCBM clustering [1,2] and interfacial diffusion [3]. In addition, in the improvement of plastic photovoltaic cells efficiency and lifetime, the interfaces between adjacent layers play a crucial role. Indeed, morphological instabilities of the interface between the organic film and the transparent electrode were indicated as possible causes of a rapid degradation [4,5].

In order to face this situation, this study intends to contribute to the understanding of morphological and structural modification and ageing processes which may occur in the cell photoactive layer, making joint use of complementary experimental tools. For the first time in fact, the time-resolved AFM technique is applied in synergy with EDXR, to study of the effects of white light illumination on the morphology of P3HT:PCBM bulk heterojunctions blends.

3.1 P3HT:PCBM preliminary studies

The study of the cell active component, i.e. the P3HT:PCBM organic blend, was carried out by applying different experimental characterization tools to an intermediate step of the device construction, that is before the deposition of the metallic electrode, in order to observe also the organic film surface by AFM.

The samples have the structure depicted in fig 1, and were prepared with the following procedure: the indium thin oxide (ITO) substrates were cleaned in an ultrasonic bath with acetone, isopropanol, then rinsed in deionized water, dried in an oven and, finally, treated with UV- ozone. This latter procedure was performed in order to remove residual organic impurities, and to increase both the surface free energy and the work function of the ITO layer [6]. Organic layers of P3HT:PCBM in weight ratio (1:0.6) and (1:1) were deposited by spin-casting from an anhydrous chlorobenzene solution on the substrate. In addition, in order to perform the electrical characterization, complete cells were prepared. The deposition of the aluminium layer, with a nominal thickness of 110 nm, was performed through a shadow mask with 6mm diameter openings. The active surface of these devices is 0.32 cm^2.

In some cases (were specified) the substrates were spin-coated with 50 nm films of PEDOT/PSS (Baytron PH) and, subsequently, the P3HT/PCBM active layers (~120 nm) were deposited by spin-casting from an anhydrous chlorobenzene solution, thus obtaining a device such the one represented in fig. 1 b.

All the samples studied in this section were provided by the researcher of the Composants Solaires-CEA laboratory in France: realization, annealing treatments (at 170 °C for 5 min) and initial electrical characterization of the cell (J/V characteristics under simulated AM1.5, 100 mW/cm^2 illumination) were done in a glove box under controlled atmosphere (<1 ppm O_2 and H_2O).

For the cells with organic layers of P3HT:PCBM in weight ratio (1:0.6) the obtained PV parameters are Voc = 0.631 V, Jsc = 11.09 mA/cm2, FF = 65.7%, and PCE = 4.6%, for (1:1) the PV parameters are Voc = 0.594 V, Jsc = 10.67 mA/cm2, FF = 64.2%, and PCE = 4.07%.

The tools used in this study, AFM and EDXR techniques, deeply described in the first part, allow us to monitor surface roughness σ in the direct (AFM) and reciprocal space (EDXR) and the single layer thickness d. Also, by means of AFM imaging, the organic layer surface can be analysed deeply in order to individuate clusters or other surface structures that might be present.

The aim of this preliminary study is to investigate the influence of PEDOT:PSS underlying buffer

layer and of the P3HT:PCBM weight ratios on the structural properties of active layer. In fact, two different configurations of devices have been studied (Fig. 1), which correspond to two different pristine sample of un-complete cells whose upper electrode layer has not been deposited.
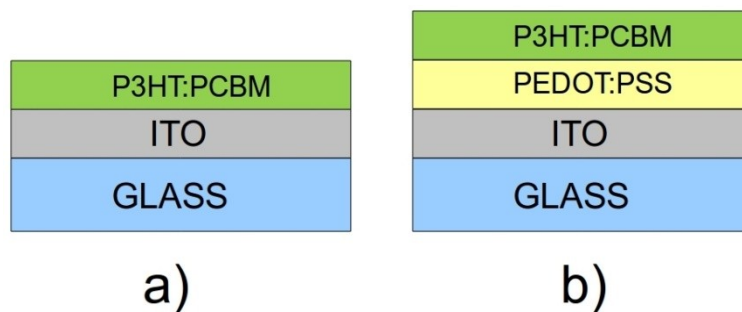

Figure 1: The two samples investigated in the preliminary study: a) device without PEDOT:PSS layer, b) device with PEDOT:PSS layer. Both samples represent an intermediate step of the device construction, that is before the deposition of the metallic electrode, in order to observe also the organic film surface by means of AF Microscopy.

The first one (a), is a device without PEDOT:PSS layer. The second sample (b), includes the PEDOT:PSS buffer layer.

In the following study, all the EDXR measurements were carried on with a beam energy of 55keV, at a scattering angles of 0.210° degrees, with a square collimation slides shape and slides apertures of 50µm*50µm. EDXD experiments had the same beam energy (55keV), with a square collimation slides shape and slides apertures of 300µm*300µm. The AFM measurements were performed in non-contact mode. FTIR measurements were performed by means of a Jasco FT/IR 470 Plus interferometer (Italy) equipped with an IRTRON IRT-30 microscope. Each spectrum was acquired in the transmittance mode by executing 300 scans at 8cm^{-1} resolution.

3.1.1 Influence of concentration ratio on structural/chemical parameters

The first step of this preliminary study, carried out by means of EDXD and FTIR techniques, aims to determine the influence of concentration ratio on structural and chemical properties of the active layer. Two sample of type a) were compared, the first one (sample 1) having P3HT:PCBM (1:1) concentration ratio (black triangles), the second one (sample 2) having P3HT:PCBM (1:0,6) concentration ratio (grey circles). The results of the EDXD study are reported in Fig. 2.
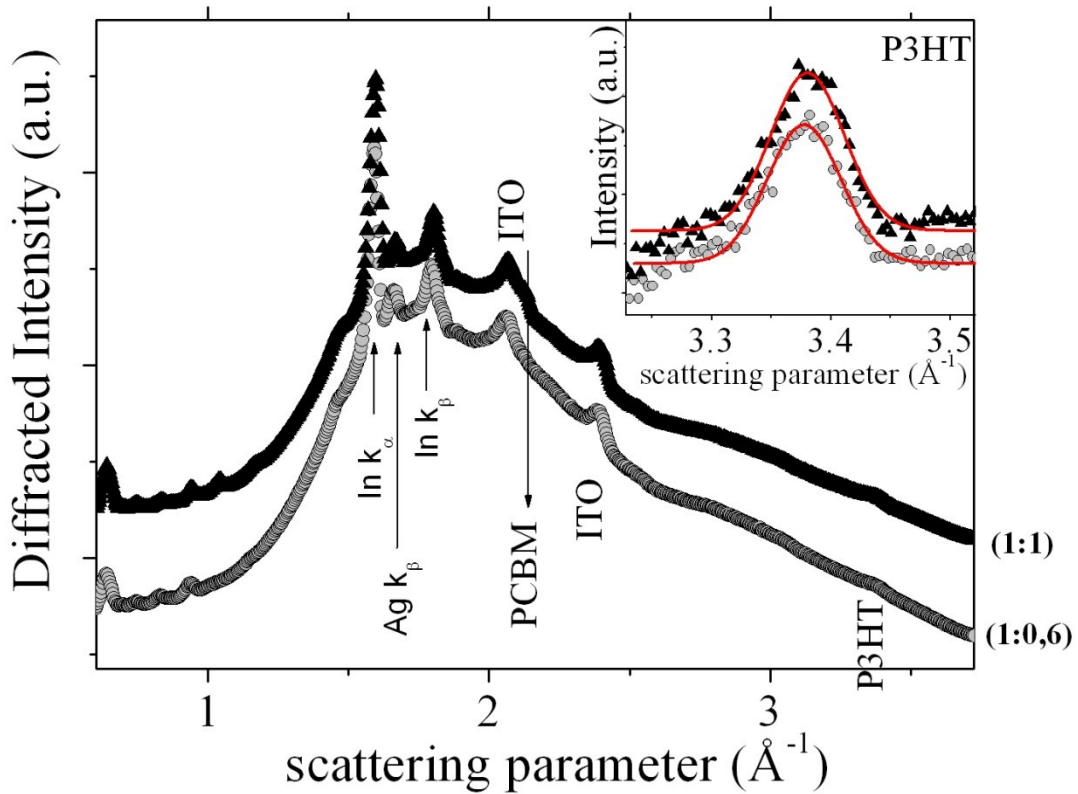
Figure 2: Comparison of EDXD patterns of two sample of type a): the first one having P3HT:PCBM (1:1) concentration ratio (black triangles), the second one having P3HT:PCBM (1:0,6) concentration ratio (grey circles). In the inset at high q region, the intensity of the q = 3.32 (1) Å^{-1} P3HT (0 2 0) reflection is shown together with its Gaussian fit.

In both samples the diffraction peaks corresponding to PCBM and P3HT are detected. In the inset, where the intensity of the q = 3.32 (1) Å^{-1} P3HT (0 2 0) reflection is shown, it is possible to notice that the two peaks are almost identical. After proper normalization (counting rates and scattering volumes), the Gaussian fit performed on the P3HT peaks shows a slight difference in peak's height , i.e. a difference in overall cristallinity between the two samples. Indeed , as expected, the (1:1) concentration sample shows an slightly higher crystallinity of the polymeric component compared to (1:0,6) sample.

Subsequently FTIR studies were carried on the same samples previously described and the comparison of the two spectra is reported in Fig. 3. Various bands are visible and have been assigned (see table I) to the blend components. The (1:1) sample shows more intense PCBM spectral markers, confirming that such film contains a higher PCBM content, as indicated by the nominal weight ratios.
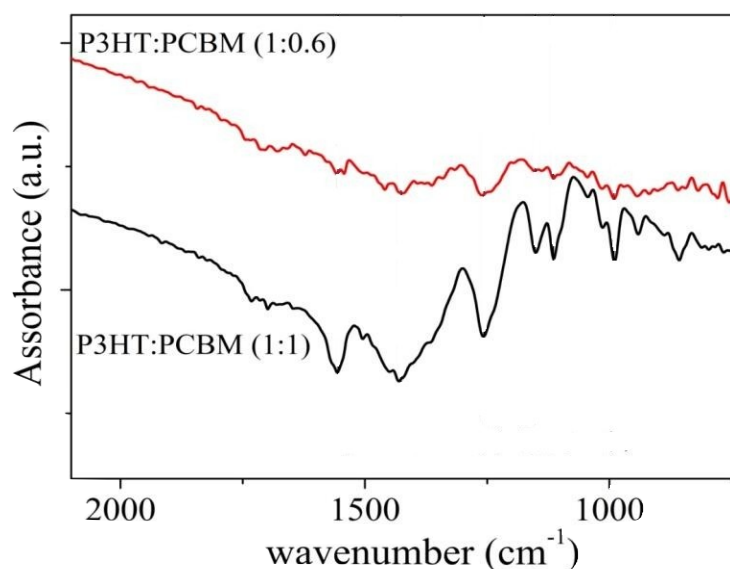
Figure 3: Comparison of the FTIR experiments: (1:0.6) pristine film (red line) and (1:1) pristine film (black line)

λ (cm⁻¹)	Modes	Molecule
990	δ (=CH & =CH$_2$)	P3HT & PCBM
1120	ν esther	PCBM
1165	δ (CH$_2$)	P3HT & PCBM
1256	ν esther	PCBM
1427	δ (CH) alkyl	P3HT & PCBM
1557	δ (C=C)	PCBM

Table I. Major FTIR bands assigned to the blend components for the (1:0.6) and (1:1) films

3.1.2 Influence of PEDOT:PSS buffer layer on structural/morphological parameters

The second step aims to investigate the influence of PEDOT:PSS buffer layer on structural properties of the active layer. Also in this case EDXD technique was used, and two sample with P3HT:PCBM concentration ratio of (1:1) were studied, one without PEDOT:PSS buffer layer, and one with PEDOT:PSS buffer layer. Results are shown in Fig 4.
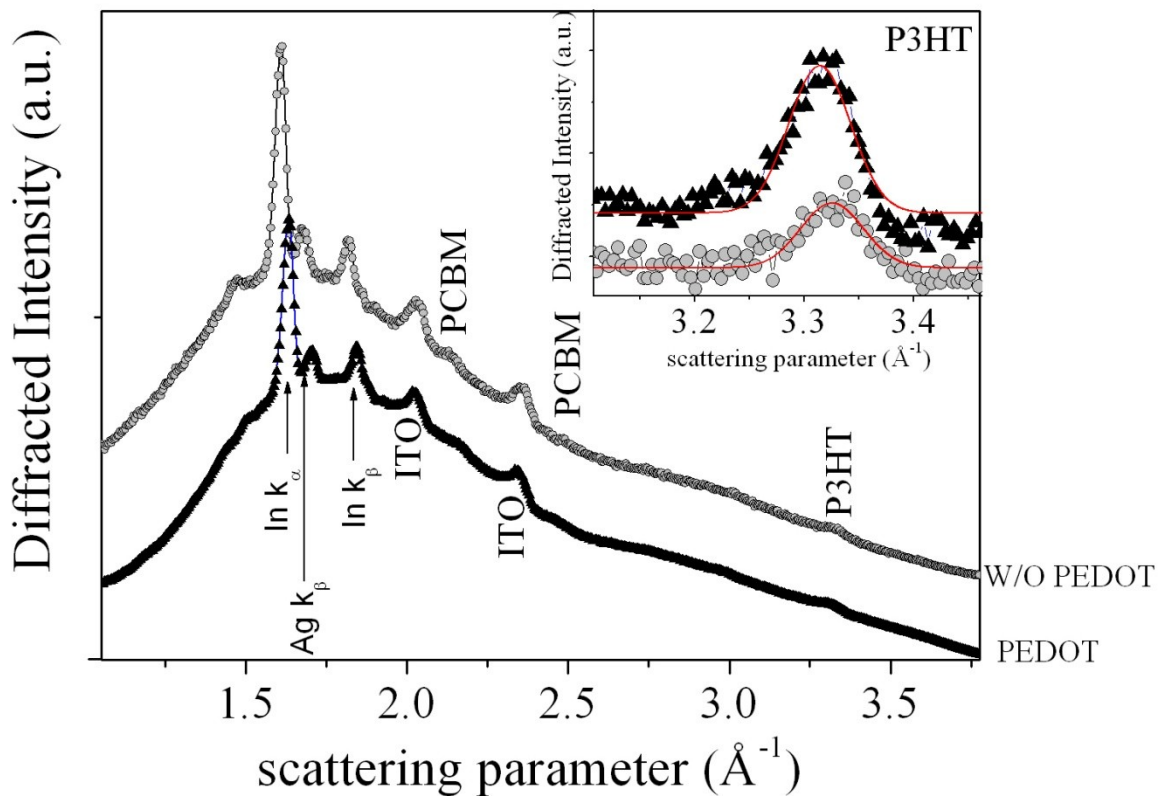
Figure 4: Comparison of EDXD patterns of two sample, one of type a) without PEDOT:PSS buffer layer, the other of type b) without PEDOT:PSS buffer layer , both with a P3HT:PCBM concentration ratio of (1:1). In the inset at high q region, the intensity of the q = 3.32 (1) Å^{-1} P3HT (0 2 0) reflection is shown together with its Gaussian fit.

Both samples show the presence of crystalline P3HT and PCBM. However, after performing the proper normalizations of the spectra, the Gaussian fits of the P3HT reflection show a quantitative difference (inset of Fig. 4). Indeed despite the measurements were performed ex-situ, thus affected by an higher error due to the repositioning of the samples, the intensity of the P3HT peak is enhanced when the PEDOT:PSS buffer layer is present. In fact when the buffer layer is deposited, a more crystalline active layer is obtained, as expected by literature [20].

A slightly visible shift of the P3HT peak towards higher q-values (less d-spacing) is also detected in the film deposited without buffer layer, which might be an hint of a somewhat stressed growth of the active layer.

Once the effect of PEDOT:PSS buffer layer on the structural parameters was addressed, its influence on surface morphology, being a crucial issue for the Al electrode deposition, was also studied. AFM measurements were performed on several portions of both samples, and the results are reported in Fig. 5, these high resolution images being representative of the whole surface. The quantitative analysis of the images revealed the average surface roughness being comparable:

(0.60±0.05)nm without buffer layer and (0.70±0.05)nm with buffer layer.
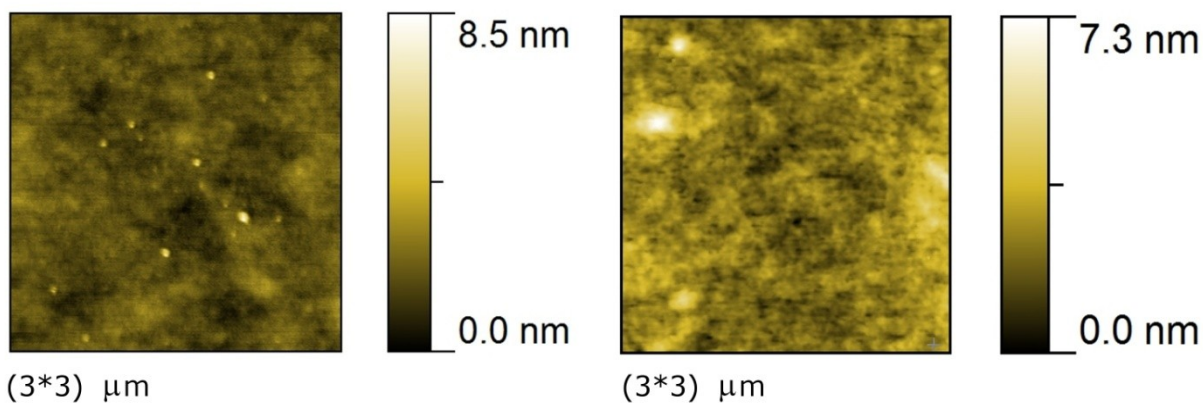

Figure 5: Comparison of 3*3 μm AFM images: pristine film without PEDOT:PSS buffer layer (left side) and pristine film deposited on PEDOT:PSS /ITO/glass (right side)

In conclusion, in both sample structures (with or without buffer layer) and both concentration ratio (1:1 and 1:0,6) the presence of crystalline P3HT is detected and good surface morphology was observed, thus indicating that the active layers presents optimal parameters for application in photovoltaic devices. Hence a layer-by-layer approach to the study of such devices can be done, taking into account P3HT:PCBM blends with different weight ratio deposited directly on ITO or on the PEDOT:PSS buffer layer, in order to clarify the phenomena occurring at the active layer or at its interface with adjacent layers.

3.2 P3HT:PCBM in situ study of morphological ageing

In the previous sections, the use of the EDXR/AFM joint technique was validated. Also, a preliminary study confirmed the applicability of this joint technique to different sample structures, whose layer of interest is actually the active P3HT:PCBM bulk heterojunction layer. In this section the effects of white light illumination on the morphology of P3HT:PCBM heterojunctions with different weight ratio and in different configuration are investigated, in order to detect morphology modifications related to efficiency and degradation issues, the two main disadvantages of active materials for solar organic devices.

3.2.1 Materials and methods

All samples based on P3HT:PCBM blends studied in this section were fabricated by the research group "Composants Solaires CEA INES-RDI, France", as described in the previous paragraph.

In sample A, B and C the use of PEDOT:PSS interlayer was avoided, in order to limit the occurrence of possible concomitant chemical–physical processes that may cause devices instability. Indeed, investigations carried on by the EDXR technique, focusing on the role of the metallic electrode in OPV devices [7], evidenced degradation of the electrode in cells having PEDOT:PSS underlayer and demonstrated that this effect may be inhibited by depositing the organic film directly onto the ITO transparent electrode. The samples represent an intermediate step in the organic device construction, in which the top layer cathode is absent, to be able to physically reach, and observe by atomic force microscopy (AFM), the organic film surface.

In the following study, all the EDXR measurements were carried on with a beam energy of 55keV, at a scattering angles of 0.210° degrees, with a square collimation slides shape and slides apertures of 50μm*50μm. EDXD experiments had the same beam energy (55keV), with a square collimation slides shape and slides apertures of 300μm*300μm. The AFM measurements were performed in non-contact mode. FTIR measurements were performed by means of a Jasco FT/IR 470 Plus interferometer (Italy) equipped with an IRTRON IRT-30 microscope. Each spectrum was acquired in the transmittance mode by executing 300 scans at 8cm^{-1} resolution.

3.2.2 Results and discussion

As a first step of this characterization, EDXR was applied in situ to study possible modifications in the P3HT:PCBM (1:0.6) films morphology, due to light exposure. The results of the time-resolved

EDXR measurements on the as deposited sample (*sample-A*), are reported in Fig. 6. The reflectivity profiles (shifted in height for clarity) were collected during the irradiation of the sample by a 10mW/cm^2 white lamp for about 70 h.
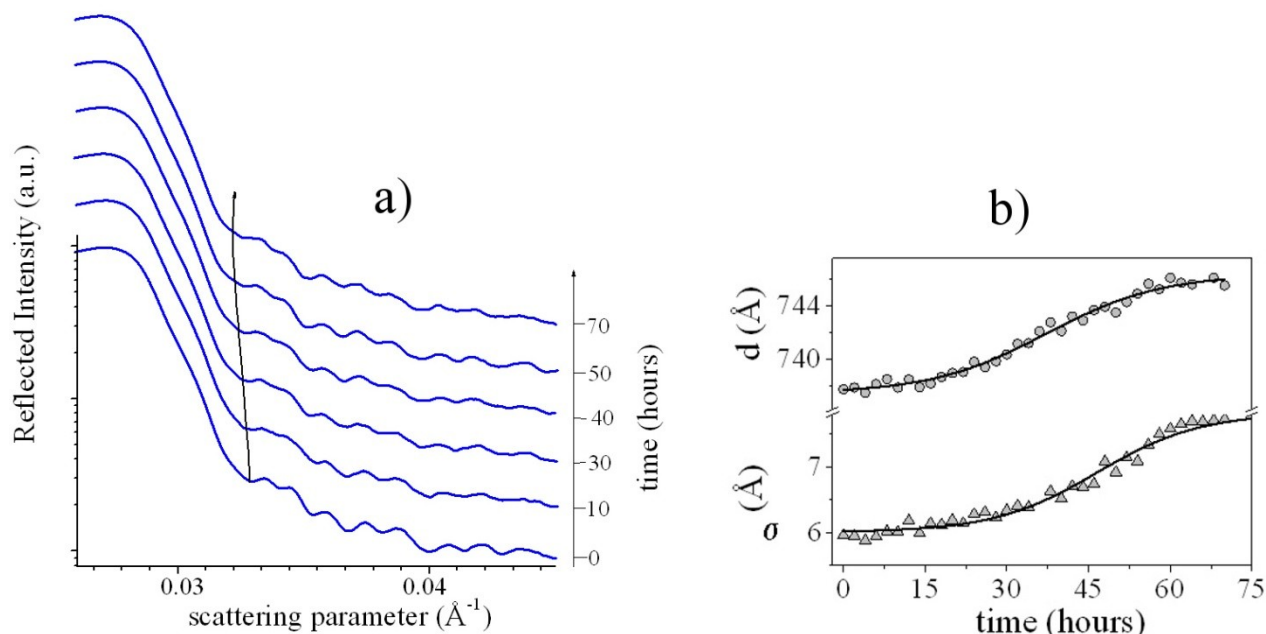

Figure 6: ***a)*** *EDXR profiles (shifted in height for clarity) collected on P3HT:PCBM as deposited sample, during illumination for about 70 h.* ***b)*** *morphological data points evolution (film roughness σ vs. time, film thickness d vs. time) obtained by the analysis of the EDXR patterns.*

Each pattern was fitted according to Parratt model and the thickness d and roughness σ so determined are plotted in Fig 6 b). The curves undergo a progressive compression, testified by the shift of their minima toward lower q values as a function of time (see, for example, the line connecting the second oscillation minima). This indicates an increase in the film thickness, connected to the oscillation period Δq by the approximate relation $d = 2\pi/\Delta q$. The d(t) and σ(t) curves can be described by Boltzmann growth. The amplitudes (and time constants) of the overall variations are about: $\Delta d = 8$ (0.5) Å ($\tau = 37$ h) and $\Delta\sigma = 7.5$ (0.7) Å ($\tau = 40$ h), respectively. The overall thickness increase is about 1%.

The change in the morphological parameters gives evidence of a modification in the film packing, suggesting that the blend molecules undergo a bulk reorganization under illumination, likely due to heating effects (the measured samples temperature was about 70 °C). Therefore, a first finding is that the bulk of such low PCBM content films is morphologically quite stable, only a minimal change (few Ångstroms) being detected. Still, it appears important to understand the origin of the latter modification and possibly inhibit it.

Additional information on the structural properties of the P3HT:PCBM layer is gained by EDXD, applied to the sample before and after exposure to light (during the in situ EDXR experiments). The diffraction angle was chosen in order to have a diffraction pattern whose diffraction peak do not superpose to fluorescence peaks, and in general to have a clear diffraction pattern of simple interpretation. Hence the selected angle is $\vartheta=5.1°$ degrees. The patterns reported in Fig. 5 are characterized by several contributions arising from the various layers. Fluorescence lines from barium (contained in the glass substrate), indium (from ITO) and of Ag are present. The latter, suggests the presence of impurities in the deposition chamber, likely due to the fact that Ag cathodes were deposited in the same environment). Several reflections from the ITO underlayer are also well visible (labeled in Fig. 7). In addition, the P3HT (0 2 0) reflection at q = 3.32 (1) Å^{-1} [8] is detected, together with a (minimal) modulation of the signal at about q = 2.11 (1) Å^{-1}, where a reflection due to PCBM is expected [9].

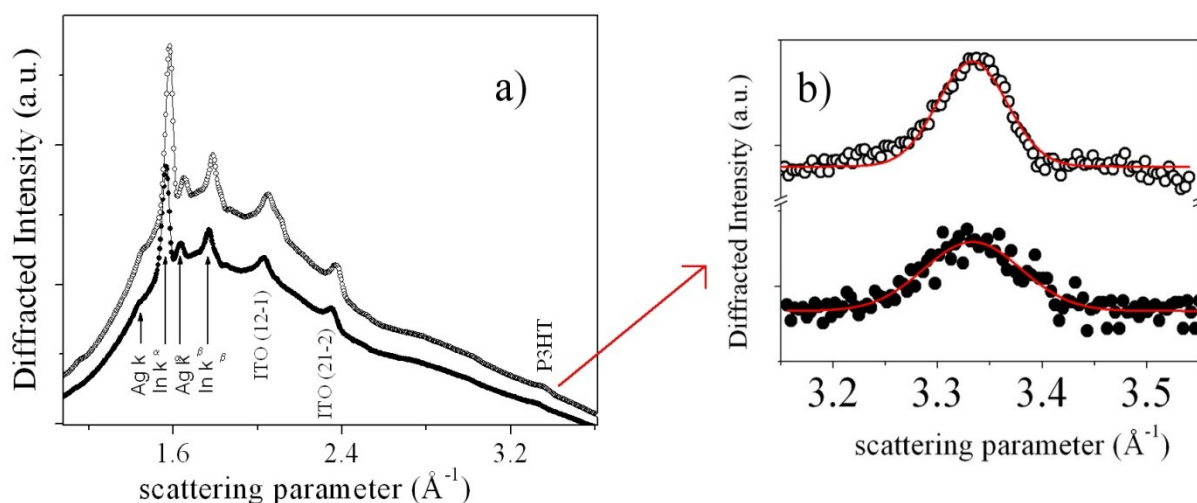*Figure 7: a): Comparison of the EDXD patterns: pristine film (open circles) and illuminated film (black circles). b): high q region, showing the intensity increase and the sharpening of the q = 3.32 (1) Å^{-1} P3HT (0 2 0) reflection*

Therefore, the blend morphology appears to consist of regions characterized by a partially crystalline texture of P3HT (as evidenced by the presence of the P3HT (0 2 0) reflection at q = 3.32 (1) Å^{-1}), embedded in an amorphous polymer matrix. Some evidence of PCBM nanocrystalline domains is also gained. These data are in agreement with literature, where the presence of a P3HT crystalline component in pristine films made from low PCBM concentration blends is reported [10].

The P3HT crystallite average size was estimated from the diffraction pattern, by means of an equation based on the Laue relations (equivalent to the Scherrer formula valid for the Angular Dispersive X-ray Diffraction mode):

107

$$\frac{1}{2}tq_2 = (n+1)\pi \text{ and } \frac{1}{2}tq_1 = (n-1)\pi$$

where t is the crystallites average diameter; q_1 and q_2 are the interference function zeros adjacent to the function maximum ($q_1 < q_2$); n is the order of the interference function peaks (the parameter that labels the features of the 'sinc' interference function).

The grain size of the P3HT nanodomains is estimated to be about *7 nm*.

These results point out that the active layer shows interesting structural/morphological characteristics. In addition, the diffraction profile collected after the irradiation allowed to verify the effect of light on the film nanoscale properties. A sensible change of the shape of the P3HT (0 2 0) reflection is observed in the illuminated sample, consisting of both an intensity increase and a peak sharpening. The peak intensity, obtained by a Gaussian function fit, increased of about 105%. All the rest being unchanged, this latter parameter is proportional to the sample crystallinity (number of P3HT crystallite nanodomains for unit volume). Therefore, the EDXD data gives evidence for a crystallization process of the P3HT component of the blend during exposure to light. Furthermore, the diffraction peak sharpening indicates an increase in the P3HT nanodomains size, up to a grain dimension of about *10 nm*. Finally, in the pattern acquired after illumination, the PCBM reflection around $q = 2.11$ (1) Å^{-1} is largely enhanced.

These data demonstrate that illumination favours a further organization of the P3HT in crystalline domains, proceeding by nucleation of the pre-existing crystallites (secondary crystallization process). At the same time, after illumination, an improved signal form PCBM nanocrystalline domains is obtained. Therefore, the picture gained by EDXD suggests a reorganization of the active layers molecules, that, in turn is likely the origin of the changes in the film morphological parameters observed by in situ EDXR technique. Importantly, controlling modifications in the structure and morphology of bulk heterojunction films, that may result in phase separation between the donor and acceptor materials, is among the key aspects in addressing cell durability and reliability.

Annealed Sample - EDXR

Therefore, to deeper address the blend aging, a further in situ investigation was executed. A new film, *sample-B*, was prepared, annealed at 110 °C for 5 min after deposition, and measured during exposure to light.

The morphological data points (film roughness σ vs. time, film thickness d vs. time) of sample-B, obtained by processing the EDXR patterns are reported in Fig. 8 (left side).
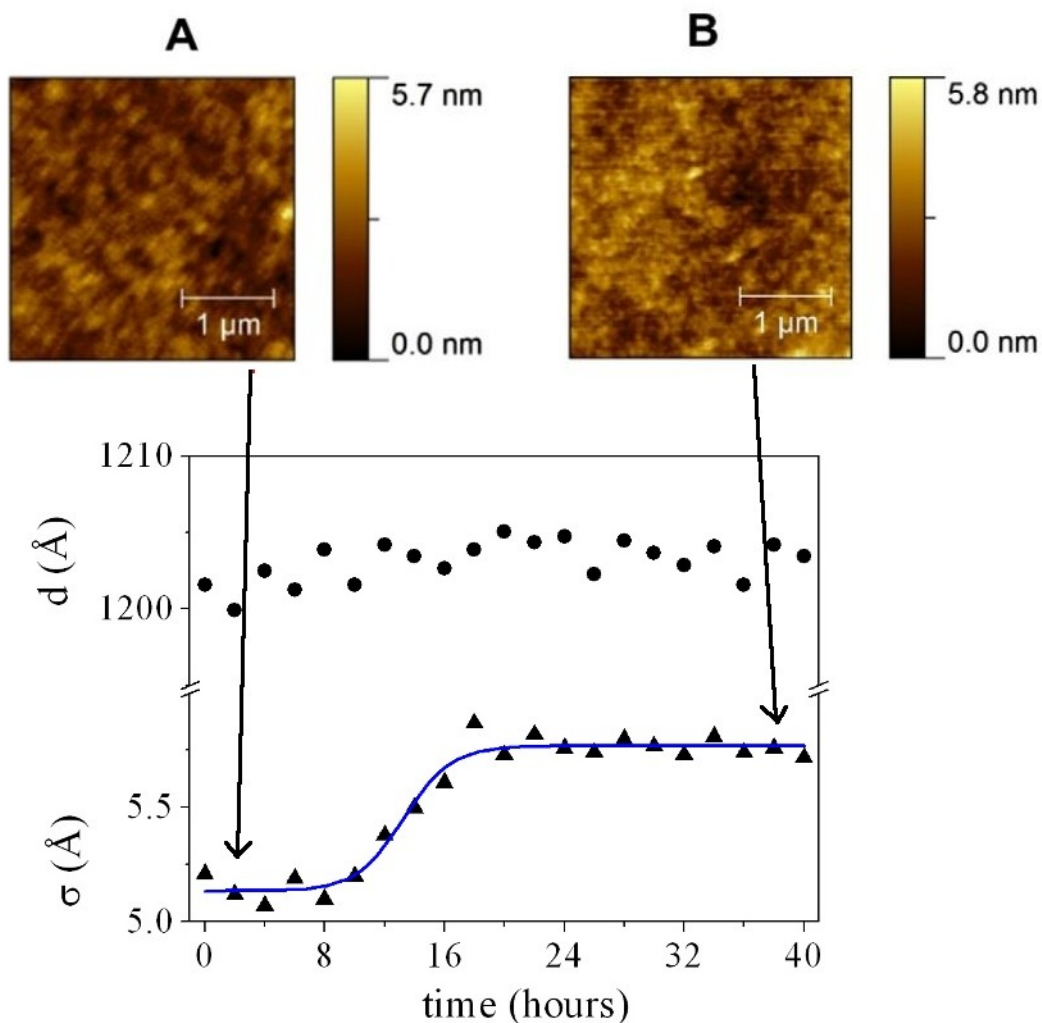
Figure 8: Results of experiments on P3HT:PCBM annealed film: time evolution of the morphological data points, obtained by EDXR (lower side) and comparison of the AFM images (A) collected before illumination and (B) after illumination.

The thickness resulted to be constant, while the film roughness augments over time. The time-resolved experiment allows to appreciate the sigmoidal increase trend of the $\sigma(t)$ curve, despite that the overall roughening is minimal. In this case, the amplitude and time constant of the roughness increase process are: $\Delta\sigma = 0.7\ (0.6)$ Å and $\tau = 13h$, respectively. Therefore, unlike the previous case, where a bulk process occurred, this time only the film surface and/or, possibly, its interface with the substrate are involved in the morphological modifications produced by illumination.

As a result of the reported time-resolved EDXR experiments, we can conclude that, if a reorganization inside the blend occurs during illumination, the process concerns a negligible number of molecules, not modifying the bulk structure. Nevertheless, a roughening phenomenon still occurs, testifying the deterioration of the organic layer surface and/or of its buried interface.

At this point, in order to understand the origin of this latter process, additional information is

109

needed to understand the nature of the roughening increase, that is to say if it depends from the interface or from surface modifications that have occurred. Indeed as already discussed the roughness value includes both terms (surface and interface roughness) which are tightly entangled from the analytical point of view, and their exact calculation is difficult.

To solve the difficulty, here an independent measurement of the surface roughness was executed by AFM, performed on the annealed sample before and after its exposure to light (during the time-resolved EXDR measurements). Comparing the AFM results (Fig. 8, right side: image A before illumination and B after illumination) no surface modifications up-on simulated working conditions of the annealed sample is observed. The initial surface morphology is qualitatively analogous to the final one: the sample is characterized by uniform topography, testifying that the components are homogenously dispersed in the blend matrix. In particular, no significant modification of the surface roughness was detected (σ_{AFM} = 6.8 (0.5) Å before illumination (A) and σ_{AFM} = 7.0 (0.5) Å after illumination (B)).

Therefore, this first EDXR/AFM cross-monitoring suggests that the major responsible for the film roughening is its buried interface. To further conform this statement, a number of AFM experiments was performed on several region of the surface to verify that the images are representative of the sample topography. However, despite this multiple sampling, an accurate description of the surface may not be gained by such ex situ AFM experiments, since small differences in the local morphology may result in large variations of the roughness calculated by processing the images.

Annealed Sample - AFM

To overcame this problem, and have a direct proof that the roughening increase is limited to the buried interface, a new sample (*sample-C*) was deposited, submitted to the same annealing procedure and studied by in situ AFM up-on exposure to light, thus reproducing the same conditions in which sample-B was studied by EDXR.

The subsequent time-resolved AFM study monitored a fixed portion of the sample surface, allowing to detect any possible change in real time. The result of this sequential collection of images is that the surface morphology does not modify (see Fig. 9 A and B comparing the first and the last image). The roughness values deduced from the AFM measurements (σ_{AFM}) are reported in Fig. 9. The σ_{AFM} vs. time curve is constant, indicating that no surface deterioration occurs.

Therefore, a direct information on the evolution of the buried interface and/or of the sample surface may be obtained by comparing the results of AFM/EDXR time-resolved experiments. Indeed, as a major result of this synergic study, it becomes clear that the raise in roughness, observed by EDXR, is due to the deterioration of the organic film buried interface, the surface roughness (obtained by
110

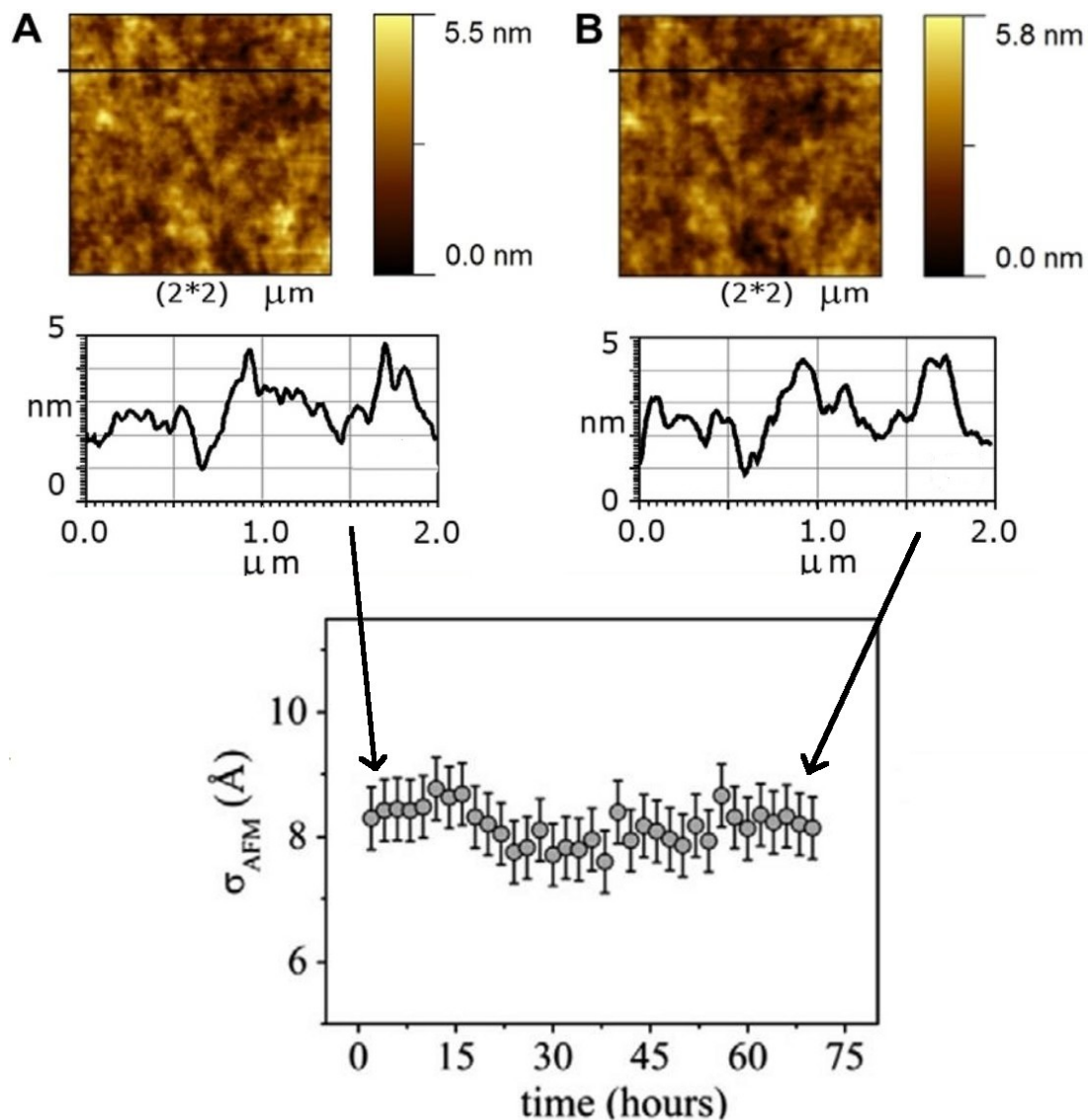AFM) remaining practically unchanged.

Figure 9: Surface morphology of P3HT:PCBM annealed film: AFM images (and line profiles) at the beginning (A) of illumination, at the end (B) of illumination and σ_{AFM} vs. time curve obtained processing each AFM image acquired during illumination.

At this point, the origin of such interface variation must be established. One possible explanation is that inter-diffusion between the polymer and the ITO substrate may occur, in analogy to what observed in polymer light-emitting diodes, based on a different polymeric film (polyphenylene vinylene) [11]. An alternative justification may be a film adhesion loss consequent to intense heating of the blend at its interface, due to ITO strong absorption in the IR band.

The following study, based on Fourier Transform Infrared Spectroscopy (FTIR) measurements acquired on the samples, before and after illumination, provided additional information useful to discriminate among the different hypothesis. The FTIR spectra relative to sample-B, after subtraction of the background signal from the ITO substrate (measured separately), are reported in Fig. 10.
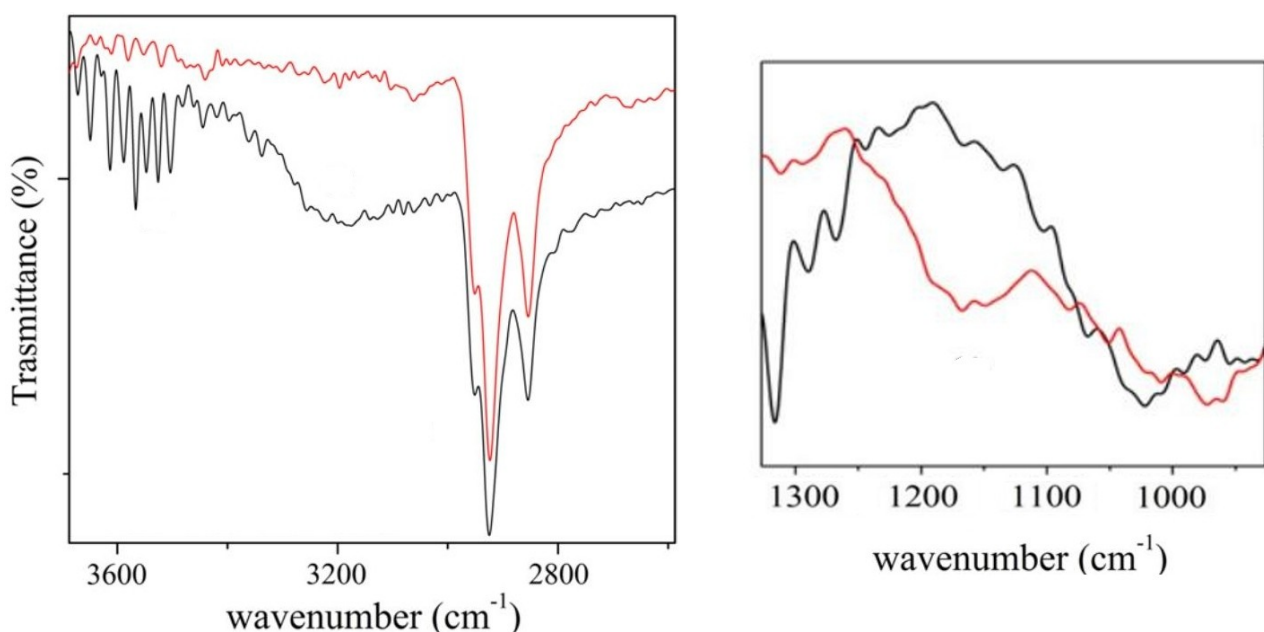

Figure 10: FTIR spectra relative to P3HT:PCBM annealed film. The spectrum of the as deposited sample (red line) is compared with that acquired after illumination (black line).

The spectrum of the as deposited sample (red line) is compared with that acquired after illumination (black line). The most remarkable differences between the two spectra are the following (see fig. 101):

(1). The appearance, for the illuminated blend, of the broad band at 3550 cm^{-1}, i.e. a spectral marker of the stretching mode of (-OH), both in H_2O and bounded in carboxylic acids

(2). The appearance of the (-OH) band at 3200 cm^{-1}, i.e. a spectral marker of bounded (-OH) in alcohols

(3). The dramatic reduction of the PCBM (C–O) ester band at 1165 cm^{-1}

Therefore, indication is gained of the presence of H_2O free molecules inside the illuminated blend. Indeed, water is present in the hygroscopic ITO substrate (both residual from the deposition and adsorbed from ambient moisture). Then, during illumination, sample heating may have promoted

112

the H_2O molecules release in the blend. In addition, the observed spectral changes can be interpreted as a signature of the fact that PCBM ester hydrolysis has occurred, with the formation of PCBM–carboxylic acid and methanol. Such reaction occurs spontaneously in presence of H_2O molecules [12]. As a consequence an acid environment is formed at the interface. It is, in turn, known that ITO is unstable and may decompose in contact with an acid solution [13], so that Indium diffusion in the polymeric layer may well occur.

Therefore, the FTIR experiments support the hypothesis that the roughening of the ITO/P3HT:PCBM interface, during light exposure, originates from inter-diffusion process consequent to chemical instability of ITO interface in contact with the organic layer.

3.2.3 Conclusion

The morphological properties of P3HT:PCBM blend with (1:0.6) ratio were studied[14]. The results obtained, simulating working conditions, allowed to correlate the modifications of the film surface topography (observed by AFM) with the film morphology (detected by EDXR). In particular, a bulk aging effect of the organic layer was detected, under illumination, by EDXR experiments for the pristine samples. Moreover, diffraction data allowed to relate this latter phenomenon to a secondary crystallization process of the blend polymeric component.

The annealed films, on the other hand, were shown to have a good bulk stability and only a minimal augmentation of the roughness was detected up-on illumination. The joint use of AFM/EDXR measurements established that the observed roughening is limited to the film buried interface. Additional information obtained by FTIR spectroscopy allowed to identify the origin of the interface aging. Indeed, comparing FTIR and AFM/EDXR results it appeared clear that, among the different hypothesis, inter-diffusion at the ITO–organic layer interface is most likely the cause of degradation.

3.3 P3HT:PCBM in situ study of structural aging

In the previous section the morphological modifications correlated to P3HT:PCBM active layer aging processes were investigated in-situ and in simulated working conditions. Also, a structural ex-situ study was performed, pointing out that illumination favours a further organization of the P3HT in crystalline domains. In this section, in order to better understand the dynamic structural phenomena occurring in P3HT:PCBM bulk heterojunction active layer, a structural in-situ study is performed.

3.3.1 Materials and methods

The bulk heterojunctions were made from blends of PCBM and P3HT, respectively, (1:1) in weight ratio. PCBM is from Nano-C and P3HT is from Rieke Metal Inc. The samples were fabricated by Laboratoire de Composants Solaires CEA INES-RDI, following the procedure described in chapter 3. In order to avoid the cathode material diffusing directly into an active layer suggested by studies in the previous section and in literature [15,16], a layer of PEDOT/PSS was also included (device of type depicted in fig 1.a)

In the following study, all the EDXD experiments were carried on with a beam energy of 55keV, with a square collimation slides shape and slides apertures of 300µm*300µm. The AFM measurements were performed in non-contact mode. FTIR measurements were performed by means of a Jasco FT/IR 470 Plus interferometer (Italy) equipped with an IRTRON IRT-30 microscope. Each spectrum was acquired in the transmittance mode by executing 300 scans at 8cm^{-1} resolution.

3.3.2 Results and discussion

To monitor the dynamical evolution of structural properties of P3HT:PCBM active layer, an EDXD analysis was performed during irradiation of the sample, by a 10 mW/cm^2 white light lamp, for about 150 h. A selection of the patterns, shifted in height for clarity, is reported in Fig. 11 upper-left side and a zoom of the high q region of the EDXD diffraction patterns is reported in Fig. 11 upper-right side. Several contributions arising from the various layers are present. The patterns are characterized by a broad signal arising from the amorphous contribution, to which the diffraction reflections from the crystalline components are superimposed. Together with the strong reflections

from the ITO underlayer, both the P3HT (0 2 0) reflection at q = 3.32 (1) Å^{-1} and the PCBM signal, at about q = 2.11 (1) Å^{-1}, are detected [8,9]. The former is a clear signature of the partially crystalline texture of P3HT and the latter gives evidences of the presence of PCBM nanocrystalline domains. In addition, several fluorescence lines are present in the low energy range, coming from glass/ITO substrate.
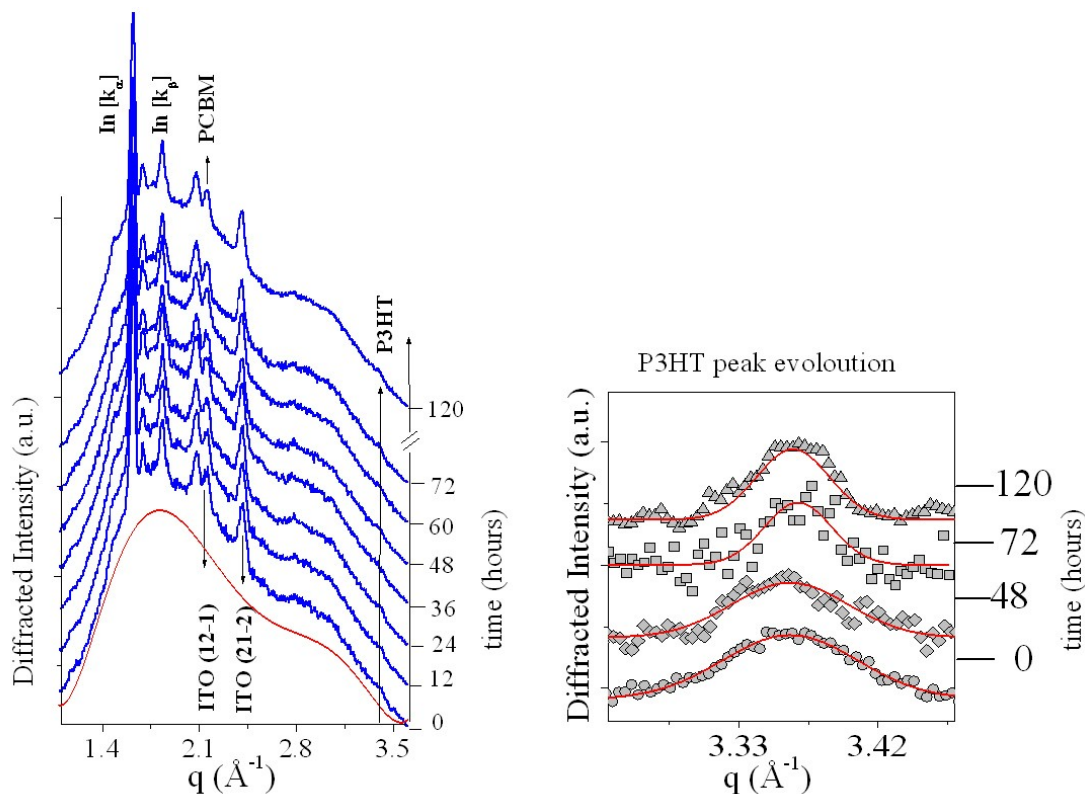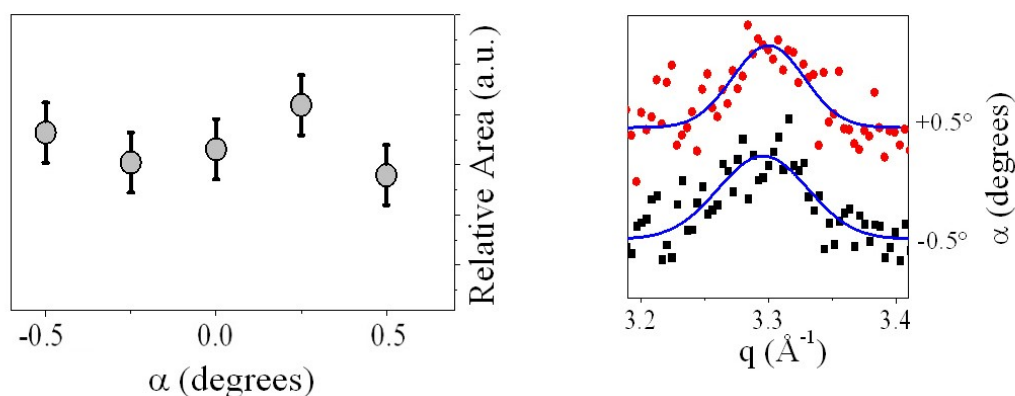

Figure 11: Time-resolved EDXD data on P3HT:PCBM sample. Upper side, left: selection of EDXD diffraction patterns (shifted in height for clarity) collected on P3HT:PCBM sample during illumination. The amorphous contribution to the X-ray diffractograms was obtained by performing the integral of a six order polynomial fit of each pattern (red line). Upper side, right: high q region of EDXD diffraction patterns, showing the P3HT (0 2 0) reflection. Lower side: result of Rocking Curve analysis (left) and comparison of the P3HT signal at the rocking angles α = -0.5° and α = 0.5° (right).

115

The time dependence of the amorphous contribution to the X-ray diffractograms was obtained by performing the integral of a six order polynomial fit of each pattern (see red line in fig. 12).

The main effect of light is a reduction in the contribution coming from the amorphous matrix, as reported in Fig. 12, upper side. These data can accommodate a model with two decay times, suggesting that two processes eventually contribute to the amorphous to crystalline conversion: a faster process (red fit) having a characteristic time (i.e. reciprocal of the highest conversion rate over time) of about 36 h and a slower one (blue fit) with a characteristic time of about 55 h.

At the same time, during illumination a sensible increase of scattering intensity in the crystalline peaks is observed. This fact is consistent with an increased number of crystallite nanodomains for unit volume (crystallinity). The overall intensity increase is about 26% for the PCBM signal and 13% for the P3HT one (Fig. 11 upper-right side), therefore closely matching with the reduced amorphous scattering intensity (40%). In addition, both the P3HT and PCBM signals are characterized by progressive peak sharpening, consistent with the formation of larger nanocrystalline domains.

On the other hand, the crystalline scattering signal may also be correlated to modifications in orientation distribution (texture) of the crystalline domains that, in principle, may vary due to rise in temperature. To clarify this point, a rocking curve (RC) analysis was performed. The RC of the Bragg reflections was measured as a function of the asymmetry parameter $\alpha = (\vartheta_i - \vartheta_r)/2$, where the incidence angle ϑ_i and the reflection angle ϑ_r are defined with respect to the sample surface.

The distribution of the diffracted intensity as a function of α keeping $\vartheta_i + \vartheta_r = 2\vartheta$ unchanged (energy dispersive mode), reproduces the statistical distribution of the domain orientation. As a result, no relevant texture of the crystalline domains was detected, as evidenced by the RC results reported in Fig. 11 lower side, together with the comparison of the P3HT signal collected at the rocking angles $\alpha = -0.5°$ and $\alpha = 0.5°$. Therefore, we can safely state that the observed increase of crystalline scattering signal during illumination is associated to a progressive improvement in sample cristallinity.

An accurate analysis of the diffraction patterns was obtained on the basis of the Laue relation seen in the previous section, that is the equivalent for the ED mode of the Scherrer formula (valid for the conventional Angular Dispersive X-ray Diffraction).

In this way the time dependence of the average size of the crystallite of the film components was obtained. The kinetics of growth of the PCBM and P3HT nanocrystalline domains upon illumination is reported in Fig. 12, lower side. The characteristic times of the PCBM and P3HT

grain size growth are, respectively, about 27 and 57 hours. Therefore, the two processes are consistent with the hypothesis of a twofold contribution to the reduction of the amorphous contribution to the EDXD signal (red line and blue line representing the data fits in Fig. 12, upper-side).
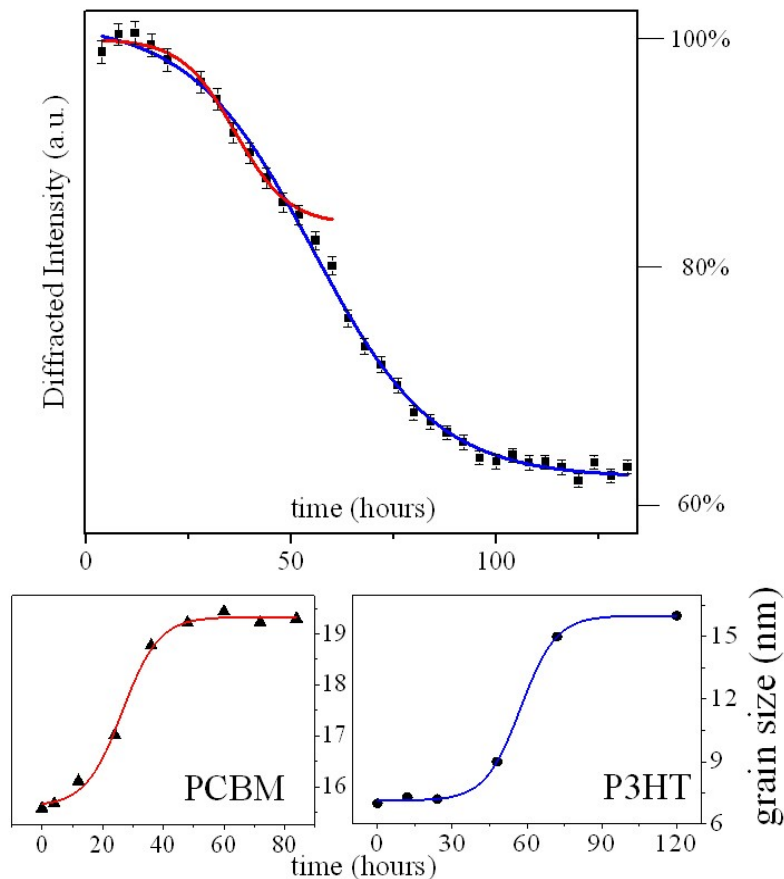

Figure 12: Time-resolved EDXD on P3HT:PCBM sample: result of the data analysis. Upper side: amorphous matrix contribution vs. time curve (in % of the initial value). Lower side: kinetics of growth of PCBM (left curve) and P3HT (right curve) grain size.

A clear picture is gained from the overall EDXD analysis, indicating the occurrence of two distinct processes: crystallization of the P3HT component of the blend and clustering of PCBM molecules into larger crystalline domains, proceeding by nucleation of the pre-existing crystallites.

These evidences suggest that the blend undergoes a structural rearrangement under illumination, due to heating consequent to illumination, which eventually results in phase separation of the two components of the bulk heterojunction. Such observation is in agreement with the results reported for a similar device [17], where both illumination and heating (in the dark) produce equivalent morphological changes in P3HT:PCBM films. Indeed, being the crystallization of the organic component due to thermal effects, the only relevant parameter is the sample temperature, regardless if it is produced by thermal heating or by illumination-induced heating.

117

This hypothesis is supported by the AFM results. In Fig. 13, a comparison between the AFM image acquired at the beginning (A, upper) and at the end (B, upper part) of the illumination (during EDXD data collection) is shown. On the lower side, (1 x 1 μm) zoom and line profiles extracted in correspondence of the black lines are plotted.
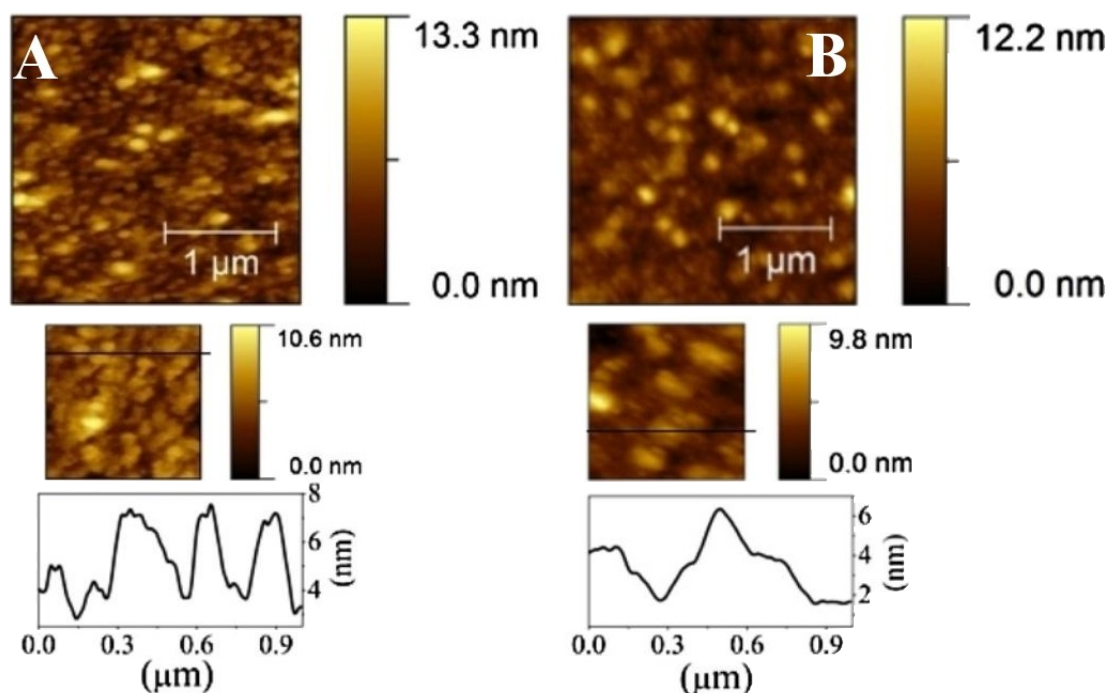

Figure 13: Surface morphology of P3HT:PCBM film: comparison of the AFM images collected before illumination (A) and after illumination (B). For each image, in the lower side, its (1 x 1) μm zoom and a line profile are shown.

It is clearly visible that a remarkable modification of the sample topography occurred. Observing both the images and the line profiles, it is evident that the pre-existing granular aggregates increased in the lateral dimensions from an average value of about 70 nm to an average value of about 150 nm. No modification of the vertical dimension is visible, testifying a 2D grow along the direction parallel to the surface plane. This may be a further indication of PCBM segregation in larger aggregates. Indeed, at the temperature (about 75°C) reached by the sample during long lasting illumination, a softening of the polymeric component is expected, favouring PCBM diffusion and clustering [2,18] and the consequent remixing of the blend components.

Further FTIR experiments validate the phase separation hypothesis and provide a picture of the chemical modifications driving such effect, Fig. 14, compares the spectra collected on the sample as deposited (empty dots line) and after illumination (blue continuous line). After illumination, the band labelled as *1* at 1751 cm^{-1}, which can be attributed to the C=O vibration (PCBM molecules), increases in intensity and shifts towards lower wave-numbers (at 1739 cm^{-1}). This is a clue to PCBM rearrangement. The bands labelled as *2*, at 1534 cm^{-1} and at 1553 cm^{-1}, and the band labelled

as *3*, at 1490 cm^{-1}, can be attributed to the ν and δ modes of the aromatic C=C bonds in the C$_{60}$ of the PCBM. These bands, after the illumination, are shifted towards lower wave-numbers (1525 and 1456 cm^{-1}, respectively), therefore indicating that the vibration occurs at higher energies, which is compatible with the PCBM clustering assumption.

Finally, the spectral region labelled as *4* is representative of the scissoring mode of both (CH$_3$) and (CH$_2$) groups vibrating around 1450–1260 cm^{-1} and 1480–1440 cm^{-1}, respectively. These groups characterize the linear chains of both P3HT and PCBM. In this case, only a slight modification of the IR spectrum (intensity decrease) is evidenced after illumination. This result is compatible with PCBM clustering.
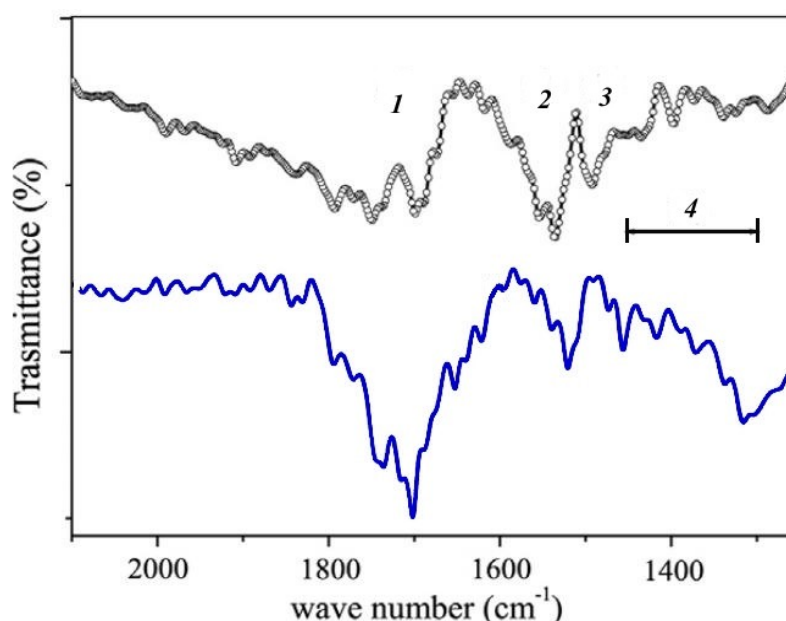

Figure 14: FTIR spectra relative to P3HT:PCBM film: the spectrum of the as deposited sample (dot line) is compared with that acquired after illumination (blue continuous line).

3.3.3 Conclusion

The structural study [19] provided, performing the first in situ time-resolved EDXD study of P3HT:PCBM blends, reports a full, real-time description of the re-arrangement of the active layer molecules. The data, collected during sample irradiation with simulated solar light, shows a growth of the PCBM and P3HT nanocrystalline domains thus evidencing two different processes: (i) P3HT crystallization and (ii) PCBM clustering into larger crystalline domains, proceeding by nucleation of the pre-existing crystallites. AFM and FTIR analysis confirm the hypothesis of structural rearrangement under illumination and in particular of a phase separation of the two components of the blend, the PCBM diffusing and aggregating in larger clusters.

Bibliography

[1] X. Yang, J.K.J. van Duren, M.R. Rispens, J.C. Hummelen, R.A.J. Janssen, M.A.J. Michels, J. Loos, Adv. Mater. 16 (2004) 802.

[2] X. Yang, J.K.J. van Duren, R.A.J. Janssen, M.A.J. Michels, J. Loos, Macromolecules 37 (2004) 2151.

[3] S. Schuller, P. Schilinsky, J. Hauch, J.C. Brabec, Appl. Phys. A 79 (2004) 37.

[4] G.F. Malgas, C.J. Arendse, S. Mavundla, F.R. Cummings, J. Mater. Sci. 43 (2008) 5599.

[5] M.O. Reese, A.J. Morfa, M.S. White, N. Kopidakis, S.E. Shaheen, G. Rumbles, D.S. Ginley, Sol. Energy Mater. Sol. Cells 92 (2008) 746.

[6] C.C. Wu, C.I. Wu, J.C. Sturm, A. Kahn, Appl. Phys. Lett. 70 (11) (1997) 1348.

[7] B. Paci, A. Generosi, V. Rossi Albertini, P. Perfetti, R. de Bettignies, C. Sentein, Chem. Phys. Lett. 461 (2008) 77

[8] K. Sugiyama, T. Kojima, H. Fukuda, H. Yashiro, T. Matsuura, Y. Shimoyama, Thin Solid Films 516 (2008) 2691

[9] M. Reyes-Reyes, R. López-Sandoval, J. Arenas-Alatorre, R. Garibay-Alonso, D.L. Carroll, A. Lastras-Martinez, Thin Solid Films 516 (2007) 52.

[10] Vanlaeke, P.a, Swinnen, A. , Haeldermans, I. , Vanhoyland, G. , Aernouts, T. , Cheyns, D. , Deibel, C. , D'Haen, J. , Heremans, P. , Poortmans, J. , Manca, J.V., Sol. Energy Mater. Sol. Cells 90 (2006) 2150

[11] .P. de Jong, D.P.L. Simon, M.A. Reijme, L.J. Van Ijzendoorn, A.W. Denier van der Gon, M.J.A. De Voight, H.H. Brongersma and R.W. Gymer, Synth. Met. 110 (2000) 1-6

[12] F.A. Carey, R.J. Sundberg, Advanced Organic Chemistry, Plenum Press, New York, 1990

[13] T.P. Nguyen, P. Le Rendu, P.D. Long, S.A. Vos, Surf. Coat. Technol. 180 (2004) 646

[14] B. Paci, a Generosi, D. Bailo, V. Rossi Albertini, and R. de Bettignies, Chemical Physics Letters, 494, . 2010 no. 1-3, 69-74,.

[15] Y. Cao, G. Yu, C. Zhang, R. Menon, and A.J. Heeger, Synthetic Metals, 87, 1997, 171-174.

[16] H. Snaith, H. kenrick, M. Chiesa, and R. Friend, Polymer, 46, Mar. 2005, 2573-2578.

[17]B. Paci, A. Generosi, V. Rossi Albertini, R. Generosi, P. Perfetti, R. de Bettignies, C. Sentein, J. Phys. Chem. C 112 (2008) 9931.

[18] K. Inoue, R. Ulbricht, P.C. Madakasira, W.M. Sampson, S. Lee, J. Gutierrez, J.P. Ferraris and A.A. Zakhidov,, Synth. Met. 154 (2005) 41-44

[19] B. Paci, A. Generosi, D. Bailo, R. Caminiti, R. de Bettignie, and V. Rossi Albertini, Chemical Physics Letters, , 504 (2011) 216-220.

[20] Gwan Ho Jung , Kyung-GeunLim , Tae-WooLee , Jong-LamLee ,Sol. Energy Mater. Sol. Cells(2011)

- Chapter IV -

P3HT:PCBM doped with AgNPs

In enhancing morphological and structural properties of organic solar cells active materials, several techniques can be used. Up to now, in the present work, insertion of buffer layer, variations in weight ratio and annealing procedures have been investigated. Another technique which seems to be very promising is the doping of active layer with inorganic materials [1].

In this chapter, through the use of combined EDXR/AFM technique applied under illumination, P3HT:PCBM active layer doped with AgNps were investigated, thus uncovering aging mechanisms at the BHJ buried interface, which is of fundamental importance when the morphological stability at the elevated temperature conditions, induced by illumination, has to be examined.

4.1 Materials and methods

One prior way to enhance device performances would be improving absorption of the active layer. Nevertheless it is not possible to gain absorption by using thicker films due to the configuration of OPV devices and the fact that the polymer has rather low carrier mobility, as discussed before. Therefore, different tactics must be explored. The approach of plasmonic devices is a promising strategy to overcome this major limit. These systems take advantage of the localized surface plasmon resonance (LSPR), resulting from the resonant interaction of the surface electrons of metallic nanostructures, with sizes smaller than the wavelenght of the light, and the electromagnetic field of light. Illumination induces the excitation of surface-waves (surface plasmons), propagating at the interface between the dielectric polymer material and the metal nanostructures. The local enhancement of the incident electromagnetic irradiation field, resulting from such collective electron oscillations, provides enhanced exciton generation and improved device efficiency [16-20].

In fig 1 the current–voltage characteristics under illumination of as-prepared (slowly grown) and annealed P3HT:PCBM (slowly grown + thermal and post-fabrication annealing steps) PV devices doped with Ag NPs in comparison with the undoped reference ones are shown [15].
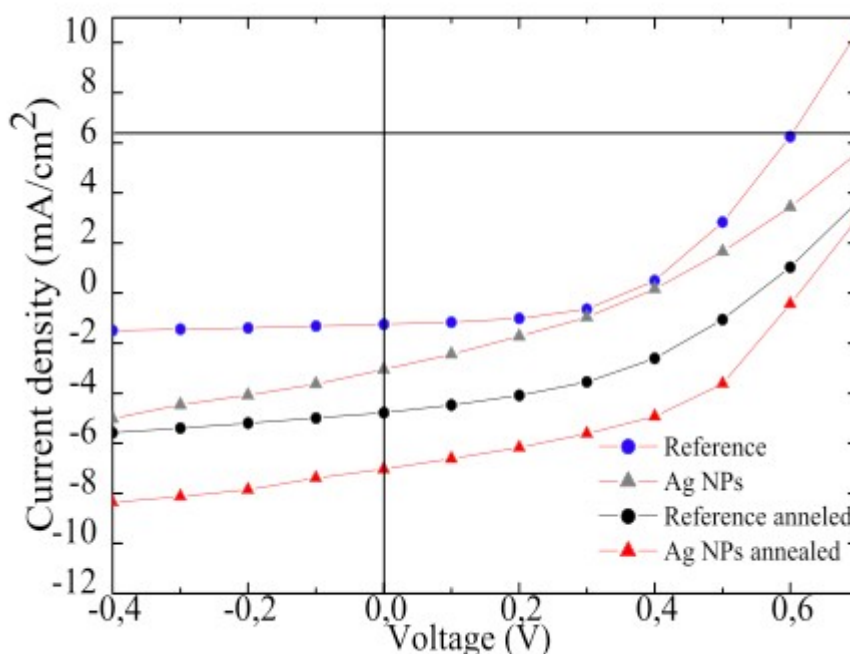

Figure 1 Current–voltage characteristics showing the PV output of reference P3HT:PCBM and the P3HT:PCBM-NPs cells average devices.

The PV characteristics of the as-prepared and annealed devices, extracted from Figure 1, are given

123

in Table 1 for pristine and annealed blends. As can be seen, the incorporation of Ag NPs in the P3HT:PCBM BHJ active layers leads to an impressive improvement of the device PCE up to 250%. This is both due to an improved short-circuit current (J_{sc}) and to an improved fill factor (FF). This improvement is observed for devices based on both as-prepared and annealed blends. It is important to stress that all devices were fabricated in air and not in inert atmosphere; this is the reason for the relative low efficiency values.

Device Structure PEDOT:PSS/ P3HT:PCBM/Al	J_{sc} [mA cm^{-2}]	V_{oc} [V]	FF	η [%]
Reference	*1.25*	*0.36*	*0.43*	*0.19*
Ag NPs	*3.05*	*0.39*	*0.43*	*0.51*
Ref. annealed	*4.78*	*0.55*	*0.40*	*1.05*
Ag NPs annealed	*7.03*	*0.61*	*0.48*	*2.06*

Table I: PV parameters of devices for both pristine and annealed blends.

The generation of NPs was performed by the research group of Institute of Electronic Structure and Laser (IESL), Foundation for Research and Technology-Hellas (FORTH), Crete, Greece. NPs were obtained by ultrafast laser ablation of metallic targets (Ag/99.98%). This technique provides the possibility of generating a large variety of NPs that are free of both surface-active substances and counter-ions[2]. The targets were placed into a Pyrex cell and covered by a layer of absolute ethanol. A femtosecond (~100fs@1kHz) laser beam was focused onto the target through the ethanol layer. The cell was mounted on a computer-driven X-Y stage and translated during laser exposure. More experimental details can be found elsewhere [3].

Laser irradiation gives rise to a high temperature gradient in the metal bulk and melts of a thin layer of the target. A fraction of the molten layer of the target is dispersed into the liquid as NPs. Further details on the structural and optical properties of the NPs were reported elsewhere [4].

Photovoltaic systems and devices based on P3HT:PCBM blends only (reference P3HT:PCBM devices) as well as those incorporating metallic NPs into the P3HT:PCBM active layer (P3HT:PCBM-NPs devices) were fabricated and electrically characterized (IV curves) by the research group the Electrical Engineering Department and Center of Materials Technology & Photonics Technological Educational Institute of Crete Greece.

Regioregular P3HT was purchased from Rieke Metals and PCBM was purchased from Nano-C. Regioregular P3HT and PCBM in 1:1 ratio were dissolved in chloroform and stirred from 1h at 60°C. The photovoltaic devices reported were fabricated on 25 mm x 25 mm indium–tin-oxide (ITO) glass substrates with a sheet resistance of 8-12 Ω/sq. As a buffer layer, poly (ethylene-dioxythiophene) doped with poly(4-styrenesulfonate) (PEDOT:PSS), purchased from Bayer AG,

124

was spin cast from an aqueous solution on the ITO substrate, giving an average thickness of 40 nm layer followed by 1h baking at 110°C inside a nitrogen-filled glove box. The metallic NPs solutions in ethanol were blended into the P3HT:PCBM solution at various concentrations. The composite photoactive layer was subsequently deposited by spin-coating the P3HT:PCBM mixture at 800 rpm for 60 s, then the films were dried for 1h at room temperature. The films studied by X-ray-AFM techniques were dried for 1h at room temperature, but not annealed.

Complete PV cells were obtained by thermally evaporating aluminium cathodes through a shadow mask. Reference and devices with Ag NPs based on both slowly grown blends and annealed blends were prepared. For the annealing process the films were thermally treated at 55 °C for 15 min followed by a post fabrication annealing for another 5 minutes at 75°C in nitrogen.

Current–voltage (I–V) measurements were performed at room temperature using an Agilent B1500A Semiconductor Device Analyzer in air. Structural and morphological measurements were carried out during illumination with a white light lamp (10 mW/cm^2), and experimental conditions of EDXR and AFM apparatus are the one described in chapter 3.2

In the following a comparative study of the structural and morphological properties of both reference and NPs doped BHJ films is reported.

4.2 Results and discussion

As discussed in the introduction, and reported in [15] incorporation of Ag NPs in the P3HT:PCBM BHJ active layers leads to an impressive improvement of the device PCE, due to improved short-circuit current (J_{sc}) and fill factor (FF).

These findings are in full agreement with previous reports, indicating that the incorporation of plasmonic nanostructures in OPV cells is expected to provide enhanced optical absorption, due to localized surface plasmon resonance (LSPR) [4,5]. LSPR resulting from the resonant interaction of the surface electrons of the metallic nanostructures and the electromagnetic field of light. Illumination induces the excitation of surface-waves (surface plasmons), propagating at the interface between the dielectric-polymer material and the metal nanostructures, having smaller size than the light wavelength. As a result of such collective electron oscillations, a local enhancement of the incident electromagnetic irradiation field occurs, leading to enhanced exciton generation and improved device efficiency [6-10].

Our goal is to address the major limitations for the poor stability of OPV devices at the typical temperatures at which they operate. To this end the effect on NPs incorporation on the active layer stability was investigated by means of in-situ time-resolved EDXR and AFM measurements, complemented by EDXD, during light exposure.

4.2.1 Effect Ag NPs incorporation on the BHJ morphological properties (EDXR/AFM analysis)

A comparative investigation of the structural/morphological properties of different blends, incorporating NPs and NPs-free-reference, was performed by time-resolved EDXR, applied in-situ, jointly with AFM, during exposure to light.

As we aim to detect the occurrence of possible structural rearrangements, due to thermal effects, the only relevant parameter is the sample temperature. In turn, as already cited, heating of the OPV cell active layer is essentially due to light absorption, the heat released upon cell working through Joule effect being negligibly low.

A preliminary characterization of P3HT:PCBM reference samples was performed, to provide a stringent comparison of the characteristics and of the behaviour of the two systems.

The results of the *in situ* EDXR measurements on the reference sample are reported in fig. 1, where

the raw patterns are shown as a function of the scattering parameter q, and of illumination time t. Each pattern was acquired for 2 hours, for an overall exposure to light of 72 hours. A shift of the oscillation towards lower q-values during light exposure is visible by naked eye and evidenced by the arrows, suggesting that the film is getting thicker. The time evolution of the morphological parameters, film thickness (d) and roughness (σ), was obtained fitting the data with the aforementioned Parratt procedure, which is shown in Fig. 1. The d(t) and σ(t) curves are well described by Boltzmann growth functions, and the corresponding amplitudes and time constants of the overall variations are about: $\Delta d = 8$ Å, $\tau_d = (20 \pm 2)$ hours, and $\Delta \sigma = 4.5$ Å, $\tau_\sigma = (16 \pm 2)$ hours, respectively.
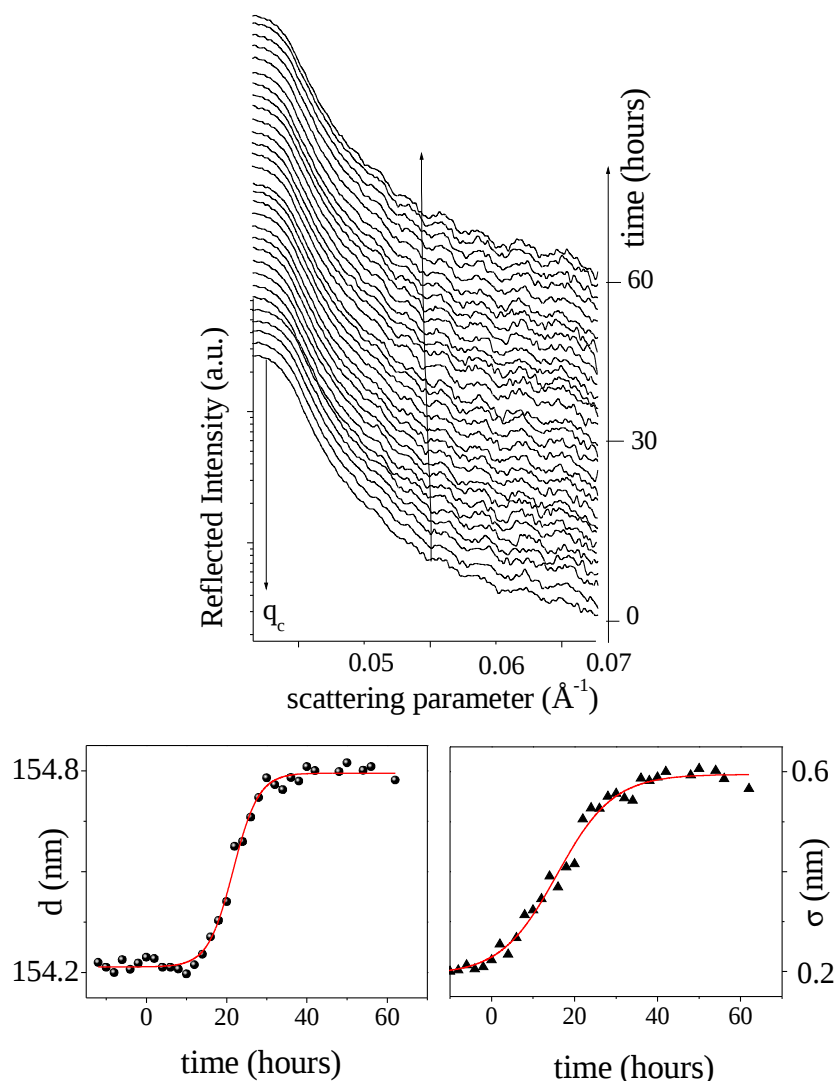

Figure 1: EDXR measurements on the reference sample. On the upper side raw patterns are shown as a function of the scattering parameter q, and of illumination time t. Each pattern was acquired for 2 hours, for an overall exposure to light of 72 hours. On the lower side, time evolution of thickness d (lower-left) and roughness σ (lower-right) obtained by means of Parratt fitting procedure, are shown.

The overall thickness increase is about 0.6 %. Such modifications in the morphological parameters evidence a bulk reorganization of blend molecules, due to heating effects consequent to illumination

127

[11].

The time-resolved AFM study of the reference sample, performed by periodically monitoring a fixed portion of the sample surface during exposure to light, is reported in Fig. 2. The sample appears to have a uniform topography, since the observed structures exhibit a height in the (4÷6) nm range and in-plane characteristic size in the (100÷120)nm range. This latter value, being very close to the lateral resolution limit, represents a superior limit of the structures' in-plane dimensions. It is observed that the surface morphology does not change at all throughout the sequential collection of AFM topography images during illumination (see Fig. 2A and 2B comparing the first and the last (4μm*4μm) images and line profiles). This steadiness of the sample topography is confirmed by the corresponding evolution of the sample surface roughness (σ_{AFM}), deduced from each AFM image.
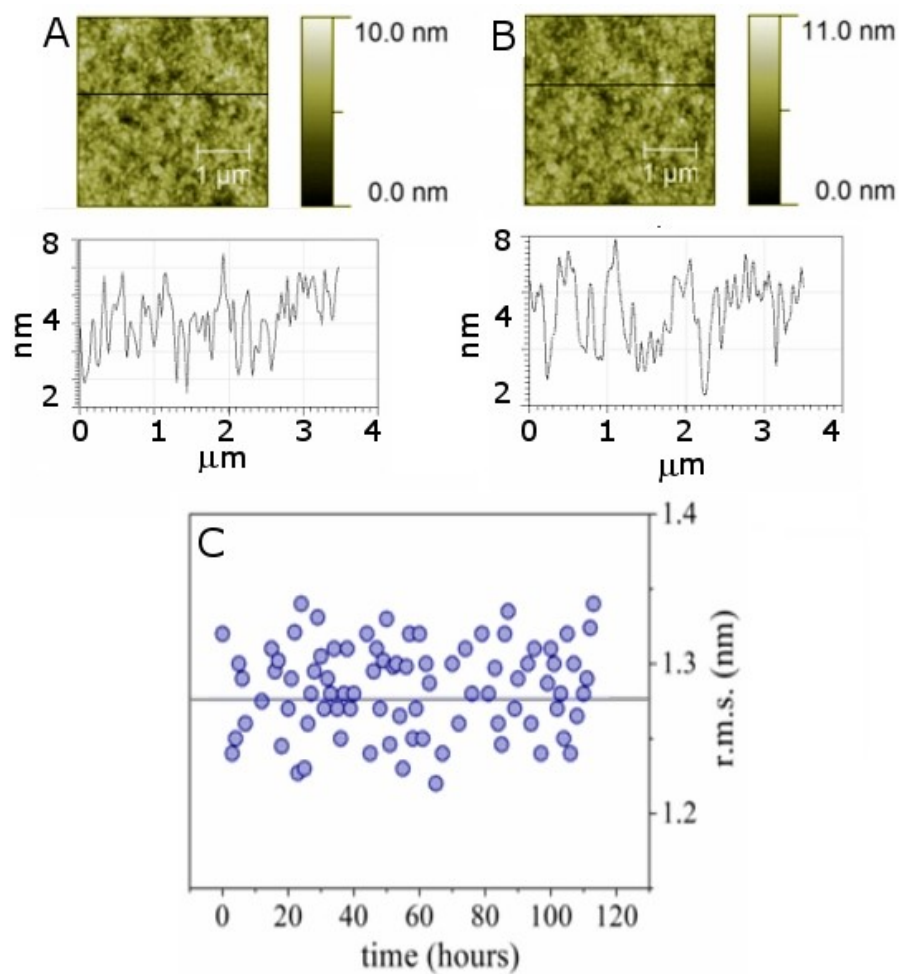

Figure 2: Time-resolved AFM study of the reference sample, performed by periodically monitoring a fixed portion of the sample surface during exposure to light. A: first 4x4 μ image of the sequence, with respective cross section profile on the right. B: last 4x4 μ image of the sequence, with respective cross section profile on the right. C: Time evolution of ample surface roughness (rms), deduced from each AFM image.

Indeed, as shown in Fig. 2C the σ_{AFM} value remains practically constant over illumination time.

Since the surface roughness remains constant with illumination time, as detected by the AFM

128

measurements, the variation of film roughness indicated by the EDXR measurements may solely be attributed to a roughening effect of the buried film interface. Therefore, the combined X-ray/AFM approach allowed the detection and evaluation of the dynamics of morphological changes occurring within the active layer during illumination and revealed two major dynamical phenomena: (i) a bulk reorganization process indicated by the film thickness increase and (ii) a degradation effect taking place at the interface between the active and the buffer PEDOT:PSS layers. The bulk phenomenon is related to a secondary crystallization process of the blend polymeric component as observed previously. The interface aging effect is also well consistent with the literature studies reporting swelling of the hole transport layer and subsequent etching of the transparent electrode [12]. Alternatively, Indium diffusion from ITO into the organic layer, observed in either OPV devices [13] or in polymer light-emitting diodes [14], may also be at the origin of interface effects.
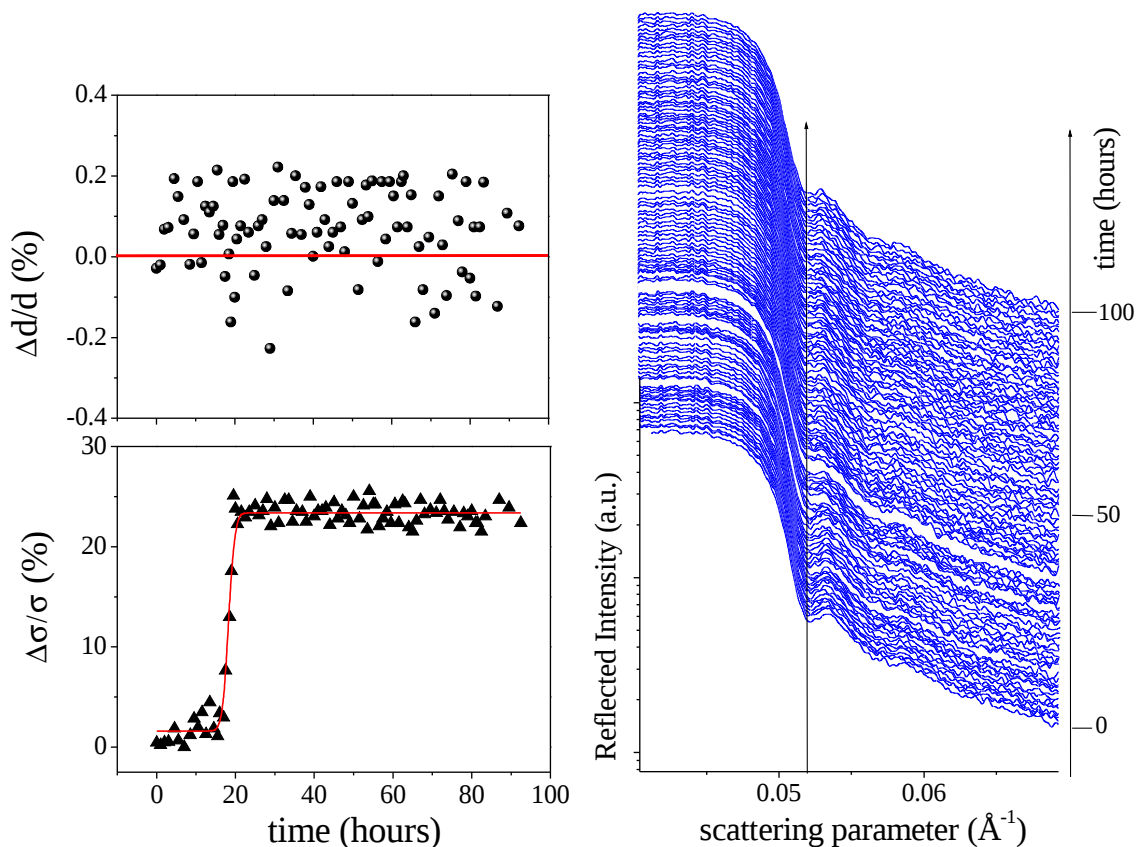

Figure 3: EDXR measurements on the reference sample. On the right side raw patterns are shown as a function of the scattering parameter q, and of illumination time t. Each pattern was acquired for 30 minutes, for an overall monitoring of more than 100 hours. On the left side, time evolution of thickness Δd/d (lower-left) and roughness Δσ/σ (lower-right) obtained by means of Parratt fitting procedure, are shown.

The second step of this joint X-ray/AFM study is devoted to blends incorporating Ag NPs (structure: glass/ITO/PEDOT:PSS/P3HT:PCBM-NPs).

Each pattern was acquired for 30 minutes, for an overall monitoring of more than 100 hours. The Parratt fitting applied to each pattern provided the time evolution of the morphological parameter with the corresponding results presented in Fig. 3. It is observed that the overall thickness remains unchanged during light exposure; d values follow a steady distribution around their mean value.

On the other hand, the EDXR roughness σ (joint interface and surface contribution) remains constant for the first 20 hours, and subsequently undergoes a fast rise up to an asymptotic value. The σ (t) curve evolution can be fitted by a Boltzmann growth (red line), having a characteristic time of τ_σ = (18.0±0.5)hours. The overall roughness increase is about 2 Å ($\Delta\sigma$ = 21%). This relative change is much lower than that measured in the case of the reference BHJ blend.

Therefore, EDXR experiments indicate that that the NPs doped film, unlike the reference one, showed a limited modification of the morphological parameters, exhibiting only a minor film roughening effect.

A deeper understanding of the origin of such effect was provided by time resolved AFM studies, allowing the evolution of surface topography to be monitored as well. Fig. 4 reports the comparison between the first (Fig. 4A, upper part) and last (Fig. 4B, lower part) of the AFM (6μm*6μm) images collected upon illumination.

The corresponding line profiles presented in Fig. 4 clearly evidence that the very same topographical features are present, even after 100 hours of continuous illumination. In this case, globular structures are present, the characteristic dimensions of which range from $x_{min}=y_{min}$= 200nm to $x_{max}=y_{max}$= 700nm (in-plane size) and from z_{min} = 10nm to z_{max}= 60nm (vertical dimension), respectively. The corresponding time evolution of the σ_{AFM} surface roughness deduced by the analysis of each AFM image collected during the sample illumination (2 hours acquisition time) is reported in Fig. 4C indicating that the rms value remains constant, distributed around the mean value of ~19 nm.

In conclusion, combined EDXR and AFM experiments suggest that the incorporation of Ag NPs in the BHJ blend leads essentially to an enhanced structural stability of the bulk of the photo-active layer, so that the only source of instability is related to a minor roughening process taking place at the blend/PEDOT:PSS interface. This is an important result, considering that the film under study was not subjected to any prior thermal treatment, usually mandatory to enhance its structural characteristics.
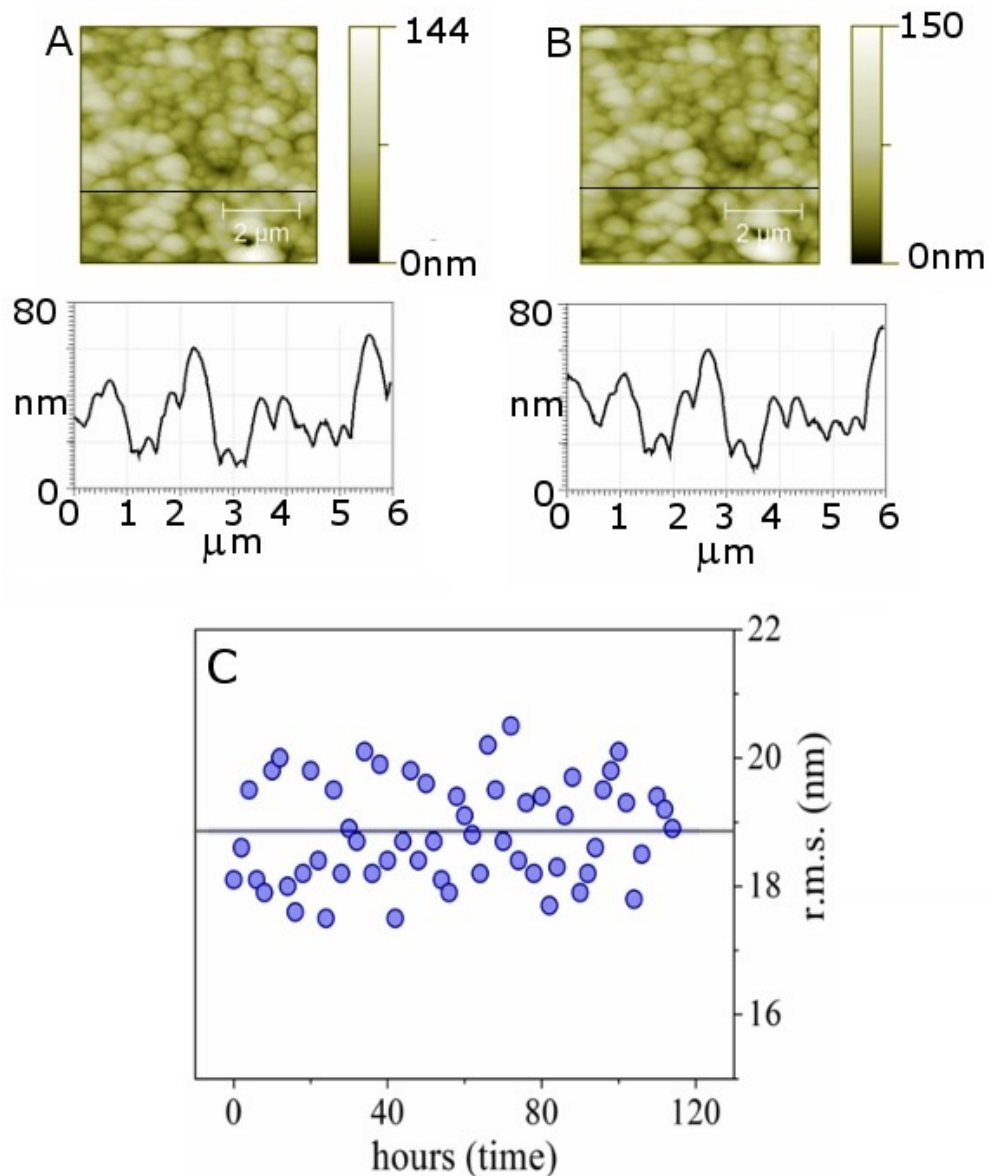
Figure 4: Time-resolved AFM study of the AgNPs-doped sample, performed by periodically monitoring a fixed portion of the sample surface during exposure to light. (a) first 6x6 μ image of the sequence, with respective cross section profile on the right. (b) last 6x6 μ image of the sequence, with respective cross section profile on the right. (c) Time evolution of ample surface roughness (rms), deduced from each AFM image.

4.2.2 Effect of Ag NPs incorporation on the BHJ structural properties (EDXD analysis)

Energy Dispersive X-ray diffraction analysis provided additional information on the interesting structural properties of the plasmonic active layer. EDXD was applied in-situ during exposure to light. The patterns in the sequence of fig. 5 upper side are characterized by both an amorphous and a crystalline contribution.

In Fig. 5, lower side, magnifications of the q regions of interest, showing the P3HT (0 2 0) reflection at q = 3.32(1) Å-1and the PCBM signal at about q = 2.11 (1) Å-1, are reported.
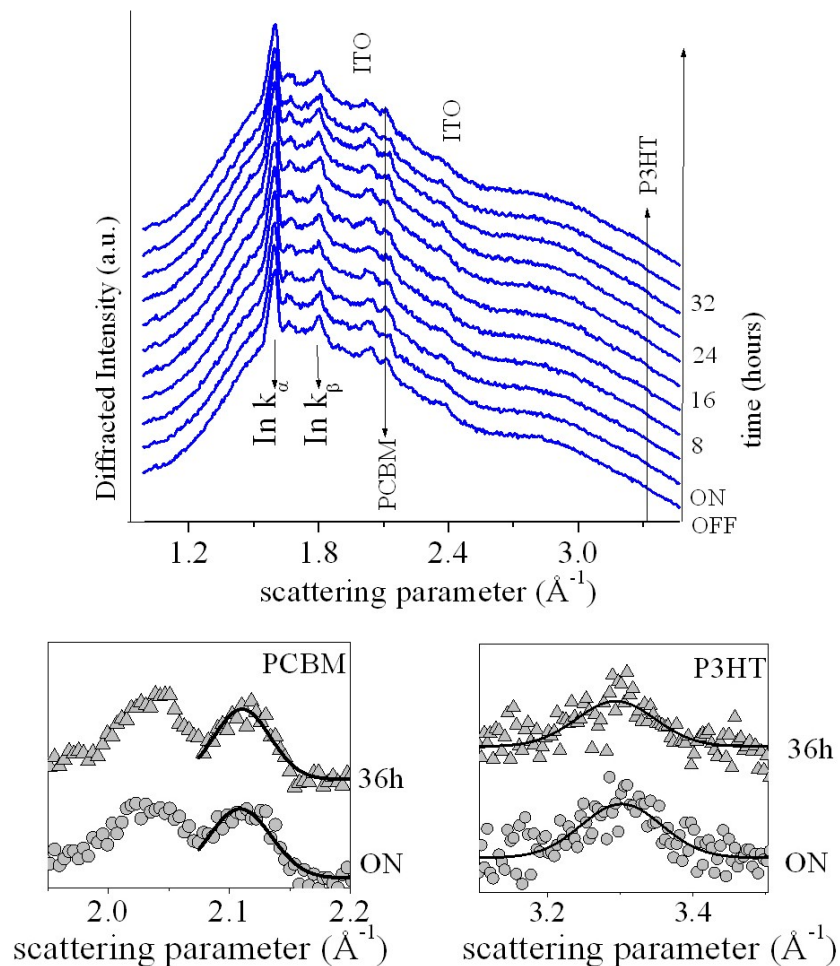

Figure 5:Energy Dispersive X-ray diffraction analysis up-on illumination. On the left side, the raw diffraction patterns are shown as a function of the scattering parameter q, and of illumination time t. On the right side, magnifications of the q regions of interest, showing the P3HT (0 2 0) reflection at q = 3.32(1) Å-1and the PCBM signal at about q = 2.11 (1) Å-1, are shown.

The data indicate that the active layer can be described as composed of P3HT crystallites embedded

in an amorphous polymer matrix. This finding is in agreement with results of the previous section, demonstrating that the incorporation of NPs does not perturb the structural properties of the P3HT:PCBM blend.

Fig. 6 shows the result of the analysis of the time resolved diffraction data (in fig. 5). No appreciable modification of the crystalline scattering intensities is observed during illumination, indicating that the number of crystallite nanodomains for unit volume (cristallinity) remains unchanged. The average crystallite size of P3HT and PCBM nanodomains was estimated from the diffraction pattern, by means of the equation based on the Laue relations.
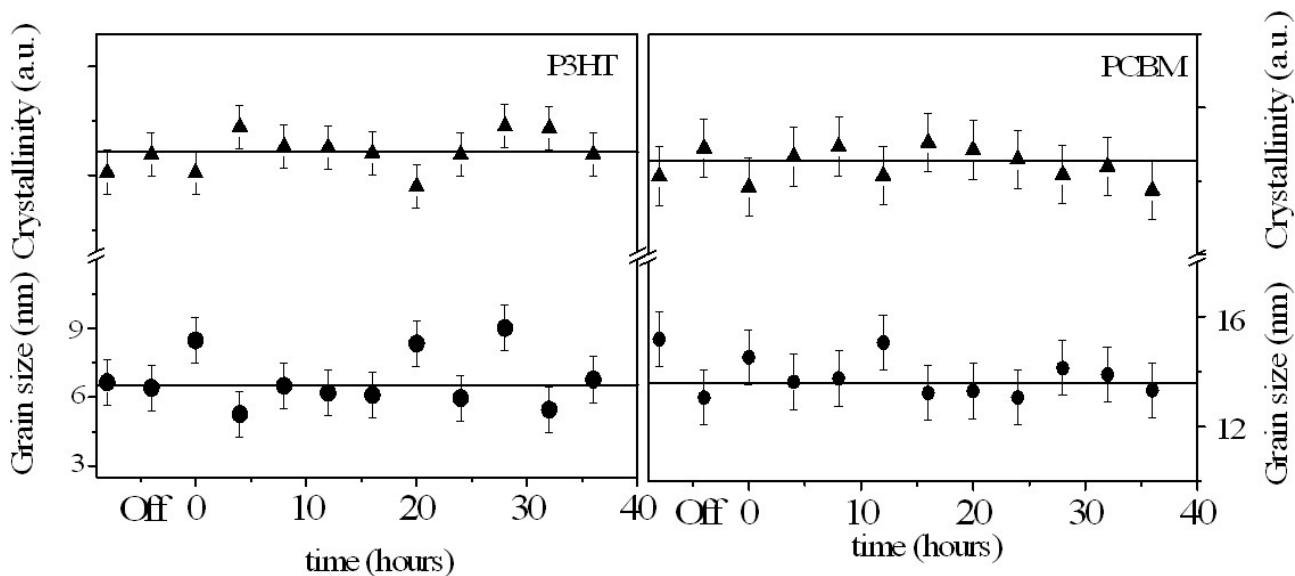

Figure 6: Average size of the crystallites of both P3HT AND PCBM film components estimated from the diffraction pattern, by means of an equation based on the Laue relations (equivalent to the Scherrer formula valid for the Angular Dispersive X-ray Diffraction mode)

The results in fig. 6 show that the average size of the crystallites of both the film components remains constant during illumination. Therefore, the time-resolved diffraction analysis demonstrates that the initial structural properties are preserved upon light exposure. This finding is an important result considering our previous observation that illumination induces a secondary crystallization process in the crystalline domains of P3HT in NPs free blends.

On the contrary, incorporation of NPs into the blend may well hinder the segmental motions of the polymer chains, leading to a mitigation of the detrimental rearrangements of the polymer structure. In conclusion, by comparing the EXDR, AFM and EDXD results it can be safely asserted that doping of the BHJ PV blends with Ag NPs gives rise to enhanced bulk stability. Contrary to the reference undoped BHJ, the only aging effect detected was a minimal augmentation of the roughness upon illumination.

4.3 Conclusions

In conclusion, it is evidenced that the incorporation of metallic Ag NPs into the active layer of BHJ PV cells leads to a dual improvement effect compared to the NP-free blend [15]. On the one hand it leads to a better PV performance and on the other hand it gives rise to enhanced structural stability of the blend. Structural superiority of the composite photo-active layer was confirmed through the unconventional joint X-ray and AFM analysis approach.

Experiments performed during illumination of NP-free active layer revealed two major dynamical phenomena: (i) a bulk reorganization process indicated by the film thickness increase over time and (ii) a degradation effect taking place at the interface between the active and the buffer PEDOT:PSS layers.

 On the contrary, the composite active layer exhibited only a minor aging effect taking place at the blend/PEDOT:PSS interface. These results are very encouraging, considering that the AFM/EDXR structural stability studies were performed on the slowly grown blends prior to any thermal annealing treatment. It can be, therefore, suggested that a systematic study of organic PV layers doped with metallic nanostructures will be a key strategy towards the development of novel OPV devices with enhanced efficiency durability .

Bibliography

[1]J. You, T. Arakawa, T. Munaoka, T. Akiyama, Y. Takahashi, and S. Yamada, Japanese Journal of Applied Physics, 50, . 2011, p. 04.

[2] E. Stratakis, M. Barberoglou, C. Fotakis, G. Viau, C. Garcia, G.A. Shafeev, Optics Express 2009, 17, p12650.

[3] E. Stratakis, V. Zorba, M. Barberoglou, C. Fotakis, G. A. Shafeev, Nanotechnology 20, 2009, p105303.

[4] G. D. Spyropoulos, M. Stylianakis, E. Stratakis, E. Kymakis, Photonics and Nanostructures Volume 9, Issue 2, 2011, p184-189

[5] J. L. Wu, F.C. Chen, Y.S. Hsiao, F. C.Chien, P. Chen, C.H. Kuo, M. H. Huang, and C. S. Hsu, 2011, ACS Nano, 5, 959, 2011, 79

[6] W.-J, Yoon, K.-Y. Jung, J. Liu, T. Duraisamy, R. Revur, F. L. Teixeira, S. Sengupta, P. R. Berger, Solar Energy Materials & Solar Cells, 94, 2010 , p128.

[7] G. D. Spyropoulos, M. Stylianakis, E. Stratakis, E. Kymakis, Photonics and Nanostructures Volume 9, Issue 2, 2011, p184-189

[8] Emmanuel Kymakis, Emmanuel Stratakis, Emmanuel Koudoumas and Costas Fotakis IEEE Trans Electron Devices 58(1), 2011, p860-864

[9] A. J. Morfa, K. L. Rowlen, T. H. Reilly, M. J. Romero, and J. van de Lagemaat, Appl. Phys. Lett., 92, 2008, 013504

[10] C. Min, J. Li, G. Veronis, J. -Y. Lee, S. Fan, and P. Peumans, Appl. Phys. Lett., 96, 2010 , 133302

[13] B. Paci, A. Generosi, D. Bailo, V. Rossi Albertini, R. de Bettignes, Chem. Phys. Lett. 494, 1-3, 2010, p69-74

[11] B. Paci , A. Generosi , V. R. Albertini , R. Generosi , P. Perfetti , R. De Bettignies , C. Sentein , J. Phys. Chem. C 2008, 112, p9931.

[12] K. Kawano, R. Pacios, D. Poplavsky, J. Nelson, D. D. C. Bradley, J. R. Durrant, Solar Energy Materials & Solar Cells, 90, 2006 , p3520.

[14] M. P. de Jong, D. P. L. Simons, M. A. Reijme, L. J. van IJzendoorn, A. W. Denier van der Gon, M. J. A. de Voigt, H. H. Brongersma, R. W. Gymer, Synthetic Metals, 110 -1, 2000, p1-6.

[15] B. Paci, G. D. Spyropoulos, A. Generosi, D. Bailo, V. Rossi Albertini, E.Stratakis, Kymakis, Adv. Func. Mat, V.21, 18, 2011, p3573–3582,

[16] W.-J . Yoon , K.-Y. Jung , J. Liu , T. Duraisamy , R. Revur , F. L. Teixeira , S. Sengupta , P. R.

Berger , Sol. Energy Mater. Sol. Cells 2010 , 94 , 128 .

[17] G. D. Spyropoulos , M. Stylianakis , E. Stratakis , E. Kymakis , Photonics Nanostruct. 2011 , 9 184 .

[18] E. Kymakis, E. Stratakis , E. Koudoumas , C. Fotakis , IEEE Trans. Electron Devices , 2011 , 58 , 860 .

[19] A. J. Morfa , K. L. Rowlen , T. H. Reilly , M. J. Romero , J. van de Lagemaat , Appl. Phys. Lett. 2008 , 92 , 013504 .

[20] C. Min , J. Li , G. Veronis , J. -Y. Lee , S. Fan , P. Peumans , Appl. Phys.Lett. 2010 , 96 , 133302 .

Conclusions

The present Thesis work aimed addressing the crucial requirement, in the development of organic photovoltaics, of the structural/morphological stability of the organic active components of the devices. Organic solar cells are, indeed, among the most interesting candidates for environmental-friendly and low-cost conversion of solar energy. However for commercialization of organic PV devices to take place, a substantial boost of their performances is still required, efficiency and lifetime remaining the major aspects to address. In this framework, a central role is played by the adoption of unconventional characterization techniques, for a deeper understand the various mechanisms involved in cell aging.

The present study focused in particular on the structural morphological properties of the organic films, constituting the active material of the cell. The approach used allowed to monitor the changes experienced by the structural properties and by the morphological parameters (i.e. the thickness and surface/interface roughness) of organic films, used as active layers in OPVs, during illumination.

This was possible thanks to an original set-up for joint in-situ Energy Dispersive X-ray Reflectometry/Diffractometry (EDXR/EDXD) and AFM experiments. The results of the Thesis indicate that such cross monitoring, allowing to detect the occurrence of bulk, interface and surface degradation phenomena, is a powerful tool to provide direct information on the structural and morphological changes accompanying exposure to light.

In particular, the preliminary studies on a reference monolayer sample allowed validating the joint EDXR/AFM technique and demonstrated its effectiveness for a quantitative estimation of surface and interface roughness, allowing to export the approach to the study of more complex multilayer samples for OPV applications.

Then, the possible causes of aging imputable to the structural/morphological instability of the various organic components of the cell, were addressed.

The PEDOT:PSS buffer layer was first investigated, in order to identify the possible source of

137

degradation that may compromise its role as hole transport layer. The aging structural and morphological issues limiting its applications in organic devices were pointed out, suggesting the need for a more stable polymer buffer layer material and effective encapsulation method.

In a subsequent phase, an extensive study of the P3HT:PCBM active layer structural and morphological modifications related to degradation issues was carried on.

Preliminarily, the influence of the presence of PEDOT:PSS buffer layer and of the active layer blend relative P3HT and PCBM weight ratio on structural parameters was considered. It was hence possible to verify that for the different sample structures and for the different active layer weight ratios, the P3HT:PCBM layers always present structural/morphological parameters well fulfilling the requirements for application in OPV devices.

Then, the active layer was studied in-situ, under the effect of white light illumination and at the typical working temperature, and its real time morphological and structural modifications were detected. This enabled to distinguish, in pristine samples, bulk aging and rearrangements of active layer molecules, suggesting a phase separation of the blend components. Conversely, an improved bulk stability was detected in annealed samples, where only a roughness increase, limited to buried interface, was measured.

Finally, an approach to mitigate the degradation pathway related to the active layer structural/morphological degradation, avoiding post-production thermal annealing, was proposed. This was done by addressing the effect of incorporation of Ag nanoparticles in the P3HT:PCBM active layer. Time-resolved X-ray and AFM investigations, during prolonged illumination in air, evidenced that both morphological and structural stability are improved without the need of any prior annealing treatment.

To conclude, the non-destructive joint X-ray/AFM characterization provided access to the concomitant chemical–physical processes occurring, during illumination, to the OPV cell organic components and related to performances degradation.

Furthermore, the systematic study carried out and aiming to find possible solution to mitigate the aging effects in organic photovoltaics,   indicates polymer-nanoparticle composites as very promising candidates for the development of novel OPV devices with enhanced durability.